UC San Diego
UC San Diego Previously Published Works

Title

Making the invisible visible—ultrashort echo time magnetic resonance imaging: Technical developments and applications

Permalink

https://escholarship.org/uc/item/35g9r729

Journal

Applied Physics Reviews, 9(4)

ISSN

1931-9401

Authors

Ma, Yajun

Jang, Hyungseok

Jerban, Saeed

et al.

Publication Date

2022-12-01

DOI

10.1063/5.0086459

Peer reviewed

Making the invisible visible—ultrashort echo time magnetic resonance imaging: Technical developments and applications ⓕ ⓢⒸⒾ

Yajun Ma,[1] Hyungseok Jang,[1] Saeed Jerban,[1] Eric Y Chang,[1,2] Christine B Chung,[1,2] Graeme M Bydder,[1] ⒾⒹ and Jiang Du[1,2,3,a] ⒾⒹ

AFFILIATIONS

[1]Department of Radiology, University of California, San Diego, California 92037, USA
[2]Research Service, Veterans Affairs San Diego Healthcare System, San Diego, California 92161, USA
[3]Department of Bioengineering, University of California, San Diego, California 92093, USA

[a]Author to whom correspondence should be addressed: jiangdu@ucsd.edu. **Tel.**: (858) 246-2248, **Fax**: (858) 246-2221

ABSTRACT

Magnetic resonance imaging (MRI) uses a large magnetic field and radio waves to generate images of tissues in the body. Conventional MRI techniques have been developed to image and quantify tissues and fluids with long transverse relaxation times (T_2s), such as muscle, cartilage, liver, white matter, gray matter, spinal cord, and cerebrospinal fluid. However, the body also contains many tissues and tissue components such as the osteochondral junction, menisci, ligaments, tendons, bone, lung parenchyma, and myelin, which have short or ultrashort T_2s. After radio frequency excitation, their transverse magnetizations typically decay to zero or near zero before the receiving mode is enabled for spatial encoding with conventional MR imaging. As a result, these tissues appear dark, and their MR properties are inaccessible. However, when ultrashort echo times (UTEs) are used, signals can be detected from these tissues before they decay to zero. This review summarizes recent technical developments in UTE MRI of tissues with short and ultrashort T_2 relaxation times. A series of UTE MRI techniques for high-resolution morphological and quantitative imaging of these short-T_2 tissues are discussed. Applications of UTE imaging in the musculoskeletal, nervous, respiratory, gastrointestinal, and cardiovascular systems of the body are included.

Published under an exclusive license by AIP Publishing. https://doi.org/10.1063/5.0086459

TABLE OF CONTENTS

I. INTRODUCTION—BASIC PRINCIPLES OF MAGNETIC RESONANCE IMAGING (MRI)

Magnetic resonance imaging (MRI) is a relatively new but fast-evolving technology that provides noninvasive, high-resolution imaging of internal body structures.[1–3] The technique uses a high magnetic field and radio waves to generate images of tissues and tissue components in the body. A commercial MRI scanner has three major components: a main magnet which generates bulk magnetization (M_0) in tissues and fluids, a gradient system which generates additional magnetic fields for spatial localization of the MR signal, and a radio frequency (RF) system, which excites the aligned spins and detects the resulting MR signal (Fig. 1).[2] The gradient system generates linear gradient fields and introduces a spatial dependence of the frequency and phase of the signal. A 90° RF pulse rotates M_0 from the longitudinal direction into the transverse plane. The MRI signal primarily originates from hydrogen nuclei (i.e., protons) in water and fat, which have a high natural abundance in humans and many other organisms. Each proton can be treated as an individual magnetic moment. Without the application of an external magnetic field, individual protons are randomly oriented, and this leads to zero net magnetization. When an external magnetic field B_0 is present, net magnetization aligned along the B_0 field results. This is the bulk magnetization M_0.[4] It is proportional to the strength of the B_0 field [Fig. 1(a)] and can be rotated into the transverse plane to create transverse magnetization perpendicular to the B_0 field. The dynamic behavior of the MR signal is characterized by two time constants: spin-lattice relaxation time (i.e., T_1), which characterizes how quickly the longitudinal magnetization (M_z) recovers back to its initial value after rotation into the transverse plane [Figs. 1(e)–1(h)], and spin–spin relaxation time (i.e., T_2), which characterizes how fast the transverse magnetization (M_{xy}) decays back to zero [Figs. 1(i)–1(l)].[3] T_1 is the time needed by M_z to reach 63% of its initial value during an exponential recovery [Fig. 1(h)], whereas T_2 is the time required by M_{xy} to drop to 37% of its initial value during an exponential decay [Fig. 1(l)].

In the body, different tissues typically have different T_1s and T_2s. Some tissues and fluids, such as muscle, most cartilage, liver, white matter, gray matter, spinal cord, and cerebrospinal fluid (CSF), have relatively long T_1s (of the order of hundreds to thousands of milliseconds) and T_2s (of the order of tens to hundreds of milliseconds).[5] Such signals are readily imaged using conventional MRI sequences that can detect signals from the transverse magnetization using echo times (TEs) of several milliseconds or longer. TE is the time from the RF pulse to the signal detection. Other tissues and tissue components, however, such as the osteochondral junction (OCJ), menisci, ligaments, tendons, bone, lung parenchyma, and myelin, have much shorter T_1s (hundreds of milliseconds or shorter) and T_2s (ranging from a few milliseconds down to sub-milliseconds).[5–8] Their transverse magnetizations decay to zero, or near zero, before the signal can be detected from them with conventional sequences. A particular group of techniques employing ultrashort echo time (UTE) sequences with TEs often of the order of 0.1 ms or shorter are used to directly image tissues of the type described above which have short (1–10 ms) or ultrashort T_2s (0.1–1 ms).[5–8] Details about these sequences are discussed in Secs. II–VII of this paper.

II. CONVENTIONAL MRI

Conventional MRI techniques allow direct imaging of tissues with relatively long T_2s. The spatial localization is based on the use of three orthogonal magnetic field gradients, which are used for slice selection (G_z), phase encoding (G_y), and frequency encoding (G_x).[2] G_z, together with an RF pulse, rotates proton magnetization to form a thin slice for two-dimensional (2D) imaging or to form a thick slab for three-dimensional (3D) imaging. The application of G_y causes the protons to gain or lose different phase increments according to their location on the y-axis. In contrast, the application of G_x causes proton magnetizations to rotate at different frequencies according to their locations on the x-axis. Cartesian sampling is typically used to collect phase and frequency encoded data in k-space. The final MR image is reconstructed using inverse Fourier transformation of the 2D or 3D k-space data.

Over the past four decades, several techniques have been developed to produce high spatial resolution MR imaging of soft tissues in the body. The most commonly used sequences are either T_1-weighted or T_2-weighted and utilize spin echo (SE), fast spin echo (FSE), and gradient-recalled echo (GRE) acquisitions. A spin echo is generated by a pair of RF pulses, whereas a gradient echo is generated by a single RF pulse in conjunction with gradient reversal (Fig. 2). Figures 2(c)–2(e) shows a representative Cartesian sampling scheme, k-space data, and the corresponding MR image.[9] An SE sequence is insensitive to B_0 inhomogeneity through an additional 180° RF pulse, which refocuses dephased transverse magnetization. A GRE sequence typically has a much shorter TE and repetition time (TR) than an SE sequence, with TR being the time between successive pulse sequences applied to the same slice or slab. SE sequences are routinely used for high-resolution imaging of tissues in the body, and GRE sequences are widely used for fast imaging due to their shorter TEs and TRs.

Conventional MRI techniques provide morphological and quantitative imaging of long-T_2 tissues in the body.[2–8] Various contrast mechanisms have been developed to display abnormalities in targeted tissues based on differences in T_1, T_2, and proton density (PD).[10–13] A series of quantitative imaging techniques have also been developed for robust mapping of MR relaxation times, such as T_1,[14–16] T_2,[16–18] T_2^* (apparent transverse relaxation time),[19] and $T_{1\rho}$ (spin-lattice relaxation in the rotating frame).[20–22] Other quantitative MRI techniques have also been developed, including measurement of magnetization transfer ratios (MTRs),[16] macromolecular proton fraction (MMF),[23] perfusion,[24] diffusion,[25] and susceptibility using quantitative susceptibility mapping (QSM).[26]

III. MRI OF SHORT-T_2 TISSUES

Conventional MRI techniques cannot directly image tissues with very short T_2s due to the fast decay of M_{xy} to zero, or near zero, before the spatial encoding gradients are applied and the signal is detected.[5–8]
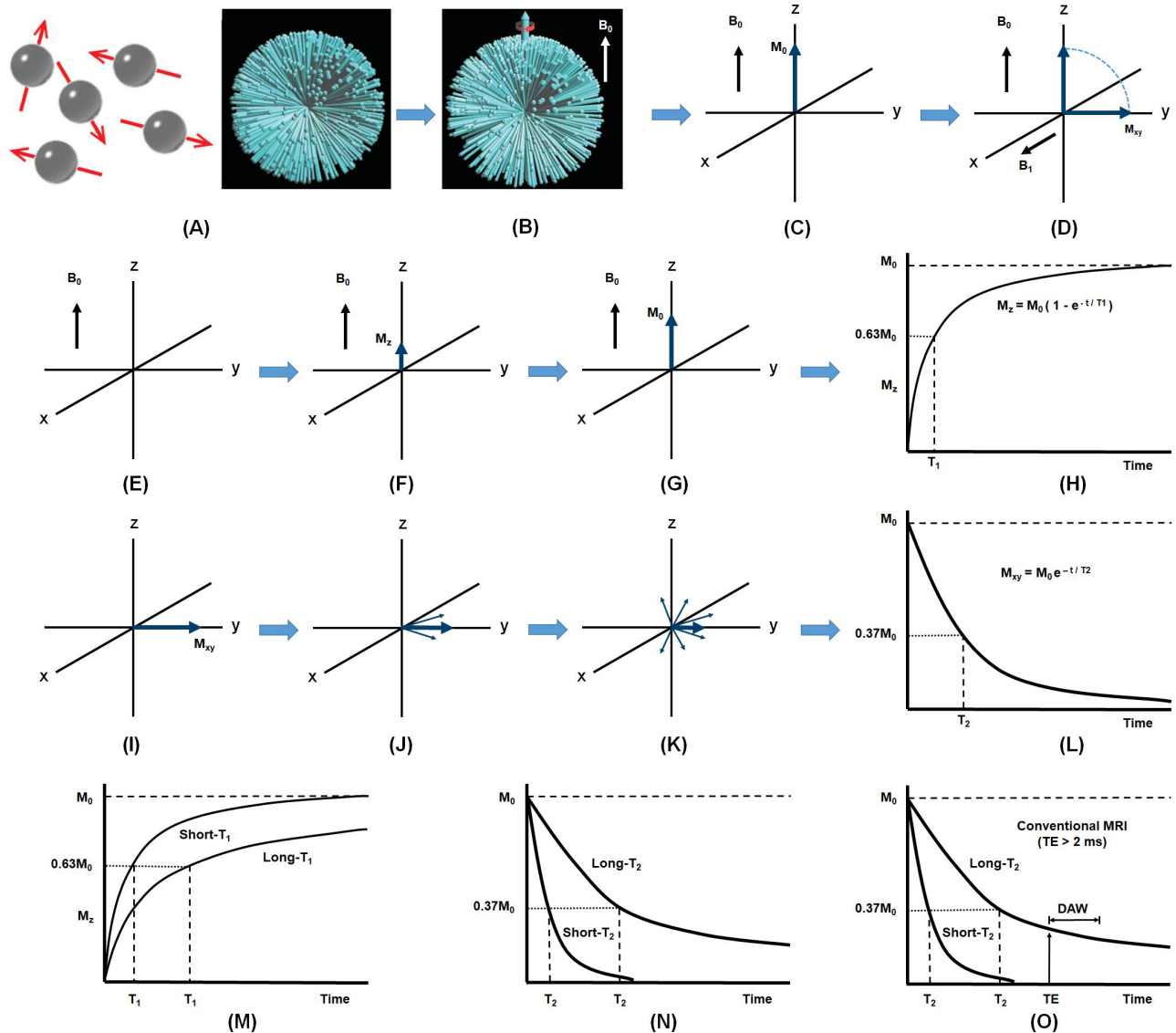
FIG. 1. The basic principles of MRI. Without an external magnetic field B_0, proton magnetic moments are randomly oriented (a). With the application of an external magnetic field, the magnetic moments are partially aligned either parallel (spin-up) or antiparallel (spin-down) to B_0 (b), resulting in a net bulk magnetization, M_0 (c). The radio frequency (RF) system, B_1, rotates M_0 into the x-y plane, creating transverse magnetization (M_{xy}) (d). When the RF system is turned off, M_z and M_{xy} undergo simultaneous longitudinal T_1 relaxation or recovery (e)–(h) and transverse T_2 relaxation or decay (i)–(l), respectively. T_1 is the time needed for M_z to reach 63% of M_0 during its exponential recovery (h), and T_2 is the time required for M_{xy} to decay to 37% of its initial value during its exponential decay (L). The human body consists of tissues with short or long T_1s (m) and T_2s (n). Conventional MRI sequences typically have TEs of ∼2 ms or longer. Hence, the decay of M_{xy} before the signal acquisition is minimal for long-T_2 tissues, but for short-T_2 tissues, the signal decays to zero or near zero during this time (o). As a result, the M_{xy} of long-T_2 tissues can be captured using a data acquisition window (DAW) before significant decay. However, because the M_{xy} of short- and ultrashort-T_2 tissues typically decays to zero or near zero before the DAW, these tissues are rendered "invisible" when conventional MRI sequences are used. (a) and (b) Reproduced with permission from L. G. Hanson, Concepts Magn. Reson. Part A **32A**, 329–340 (2008). Copyright 2008 John Wiley and Sons.[4]

As a result, short- and ultrashort-T_2 tissues appear dark on conventional MR images. The lack of signal also means that conventional clinical MRI sequences are often of little or no value for quantitative assessment of short- and ultrashort-T_2 tissues. Their MR relaxation times and other tissue properties are not known or well-characterized. These properties can include early biochemical changes such as

proteoglycan depletion, collagen degradation, and changes in water content.[5–8]

To directly detect signals from short and ultrashort-T_2 tissues, it is critical to reducing the sequence TE to less than the tissue T_2^*s to allow enough time for spatial encoding to be enabled and signal to be detected before the transverse magnetization decays to zero or near
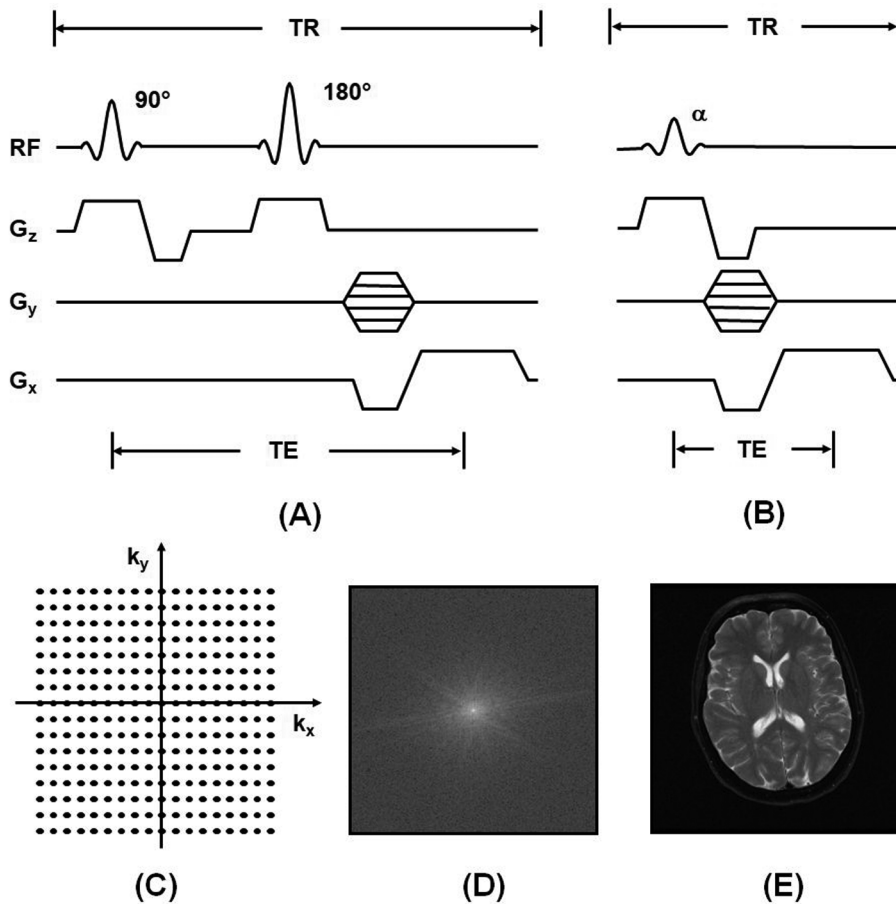
FIG. 2. (a) shows a spin echo (SE) sequence which employs a 90° RF pulse for signal excitation followed by a 180° pulse for spin refocusing, together with a slice selection gradient (G_z), a phase encoding gradient (G_y), and a frequency encoding gradient (G_x). These allow data acquisition in k-space with an echo time (TE) and a repetition time (TR). (b) shows a gradient-recalled echo (GRE) sequence which employs a single low flip angle RF pulse with a shorter TE and a shorter TR together with the G_x, G_y, and G_x gradients to acquire signals encoded in k-space. A diagram illustrating conventional Cartesian sampling of k-space is shown in (c). An example of 2D k-space data are shown in (d), which undergoes fast inverse Fourier Transformation to produce the MR image in (e).

zero. Recently, a group of sequences typically with TEs of 0.1 ms or less has been developed for high-resolution imaging of short-T_2 tissues. These sequences include ultrashort echo time (UTE) imaging,[27–37] single point imaging (SPI),[38,39] water- and fat-suppressed proton projection MRI (WASPI),[40,41] sweep imaging with Fourier transformation (SWIFT),[42] hybrid acquisition-weighted stack of spirals (AWSOS),[43] pointwise encoding time reduction with radial acquisition (PETRA),[44] ramped hybrid encoding (RHE),[45] and zero echo time (ZTE) imaging.[46] The nominal TEs of these sequences are ~100–1000 times shorter than even the shortest TEs (i.e., a few milliseconds) that are typically used with conventional MRI sequences. As a result, short and ultrashort-T_2 tissues can be directly imaged with useful signal levels and high spatial resolution.

Among the new sequences that have been developed for short-T_2 imaging, UTE sequences have attracted the most attention for morphological and quantitative assessment of short-T_2 tissues or tissue components. UTE sequences are generally based on GRE acquisitions and use radial or spiral mapping of k-space rather than conventional Cartesian k-space sampling. By using a different form of slice selection (i.e., a half RF pulse), radial mapping of k-space, and variable rate selective excitation, nominal TEs as short as 8 μs can be achieved with 2D UTE imaging [Fig. 3(a)].[27–29] Similarly, 3D UTE imaging can be achieved by combining a short rectangular RF pulse excitation with a 3D radial mapping of k-space [Fig. 3(b)].[30–34] Furthermore, the radial trajectory can be twisted for more efficient data acquisition [Fig. 3(c)].[35–37] These 2D and 3D UTE sequences make it possible to detect signals from short- and ultrashort-T_2 tissues with spatial resolution, signal-to-noise ratio (SNR), and contrast-to-noise ratio (CNR) comparable to those of conventional sequences.

While UTE sequences allow direct imaging of short and ultrashort-T_2 tissues, there are some technical challenges. First, using a short TE alone is often insufficient to provide high contrast imaging of short- and ultrashort-T_2 tissues,[32] which typically have lower proton densities than surrounding or associated long-T_2 tissues. As a result, many short- and ultrashort-T_2 components, such as those in bone and myelin, display much lower signals than surrounding or associated long-T_2 tissues and are consequently relatively inapparent even with UTE sequences. Efficient suppression of long-T_2 signals is of critical importance for high contrast imaging of short and ultrashort-T_2 tissues.[5–8,32] Second, quantitative imaging frequently allows early detection of tissue changes more effectively than morphological imaging, as morphological changes typically happen at later stages in disease progression. However, conventional quantitative MRI techniques cannot usually be applied directly to short- and ultrashort-T_2 tissues because of rapid transverse relaxation during RF excitation and before and during data sampling. This relaxation precludes signal detection and
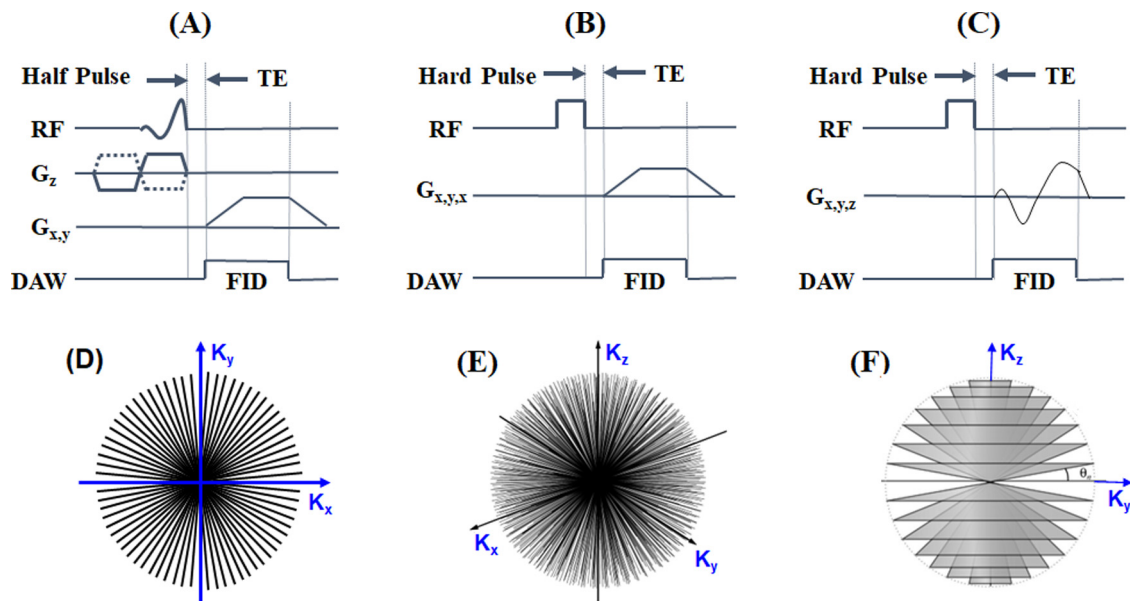
FIG. 3. Diagrams of the 2D radial UTE sequence (a), the 3D radial UTE sequence (b), and the 3D spiral UTE sequence (c), as well as the corresponding k-space trajectories (d)–(f). The 2D UTE sequence employs a slice-selective half-pulse excitation followed by 2D radial ramp sampling (a) and (d). The 3D UTE sequence uses a short rectangular pulse excitation followed by 3D radial ramp sampling (b) and (e) or twisted radial trajectories with conical view ordering (c) and (f).

accurate measurement.[5–8] Quantitative UTE techniques to evaluate the various short- or ultrashort-T_2 tissues or components (e.g., water, proteoglycan, collagen, myelin, and/or other macromolecules) using clinical MR scanners have been developed to address these challenges and will be described in this review as follows: Part I—contrast mechanisms which produce high contrast images of various short-T_2 tissues; Part II—quantitative UTE imaging techniques which quantify T_1, T_2, T_2^*, $T_{1\rho}$, and other tissue properties (PD, MTR, MMF, perfusion, diffusion, and susceptibility); and Part III—applications of UTE-based techniques in the musculoskeletal (MSK), nervous, respiratory, gastrointestinal, and cardiovascular systems.

IV. PART I—TECHNICAL DEVELOPMENT IN MORPHOLOGICAL UTE MRI

Basic UTE sequences developed with different short- and ultrashort-T_2 contrast mechanisms are described below. The feasibility of each approach has been demonstrated *ex vivo* or *in vivo* using clinical MR scanners.

A. UTE with echo subtraction

Multi-echo UTE data acquisition and subsequent echo subtraction are very effective techniques for suppressing long and medium T_2 signals and providing high contrast imaging of short-T_2 tissues or tissue components.[6,30,32] Short-T_2 contrast is achieved by subtracting a later echo image from the first, a technique that is equivalent to T_2 bandpass filtering. Signals from long-T_2 tissues decay minimally by the time of the later echo, leading to a significant reduction of long-T_2 signals after echo subtraction. Signals from short-T_2 tissues or tissue components drop significantly by the time of the later echo and are much less affected by echo subtraction. T_2^*-related signal loss prior to subtraction can be reduced by minimizing the RF pulse duration, the

TE, and the readout window.[30] This dual-echo UTE subtraction technique has been used effectively to demonstrate cartilaginous endplate (CEP) morphology, including cartilaginous endplate thickening and irregularity on subtracted 3D UTE images (Fig. 4).[47] The cartilaginous endplate is well visualized on 3D UTE images but not on longer TE T_2-weighted SE images, and UTE-detected cartilaginous endplate abnormalities shown in this way are significantly correlated with the Miyazaki grade (p < 0.001).[47] UTE with echo subtraction has also been used to image cortical bone, menisci, ligaments, tendons, graft material, and fixation elements following surgical tissue trauma repair.[48] The major limitation of the technique is its sensitivity to susceptibility, B_0 field inhomogeneity, and chemical shift effects. Fat has multiple resonance peaks leading to a short T_2^*, which has the potential to create a significant residual signal on echo-subtracted UTE images.

B. UTE with long-T_2 saturation

Long-T_2 signal saturation can be achieved by using a long-duration low amplitude 90° pulse to flip the long-T_2 magnetization into the transverse plane, where it is eventually spoiled by a large crusher gradient.[32,49,50] The short-T_2 magnetization experiences significant transverse relaxation during the saturation process. As a result, its longitudinal magnetization is unchanged and is subsequently available for detection by the UTE data acquisition [Fig. 5(a)]. Long-T_2-saturated UTE imaging has been applied to ultrashort-T_2 components in the brain, such as myelin.[50] A key parameter in UTE myelin imaging is the time-bandwidth product of the saturation pulse, which is related to spectral profile sharpness. Rectangular pulses, single-band pulses, and dual-band pulses have all been systematically investigated. Figures 5(b)–5(d) shows MR images of the brain in a healthy volunteer
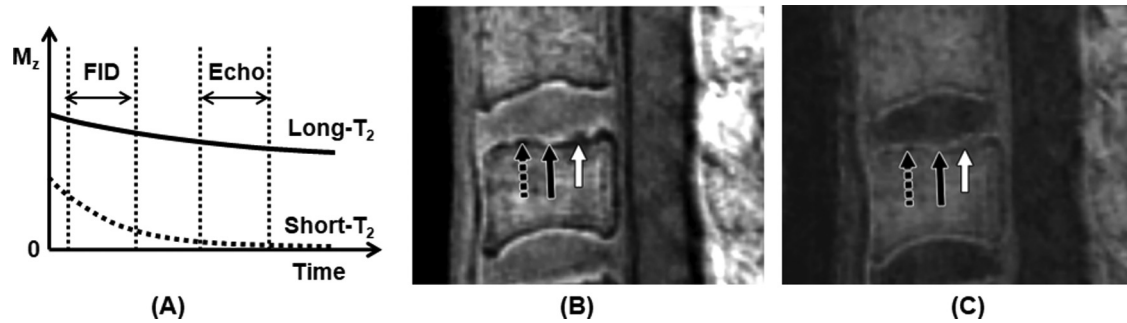
FIG. 4. The contrast mechanism for short-T_2 imaging with long-T_2 signal suppression is achieved via subtraction of a second echo image from the first (i.e., UTE) echo image (a). A mid-sagittal 3D UTE image of the C3-4 disk in a 61-year-old male patient shows cartilaginous endplate thinning (solid black arrow) and a cartilaginous endplate defect (dashed arrow), as well as focal nodular low signal intensity from a cartilaginous endplate defect (white arrow) (b). UTE with echo subtraction highlights areas of cartilaginous endplate thinning (solid black arrow) as well as the cartilaginous endplate defect (dashed arrow), both of which are well visualized because of the increased contrast-to-noise ratios (c). The focal low signal intensity associated with the cartilaginous endplate defect seen in panel (b) appears as focal irregular cartilaginous endplate thickening and irregularity (white arrow) in panel (c). (b) and (c) Reproduced with permission from Kim *et al.*, Am. J. Roentgenol. **210**, 1131–1140 (2018). Copyright 2018 American Roentgen Ray Society.[47]
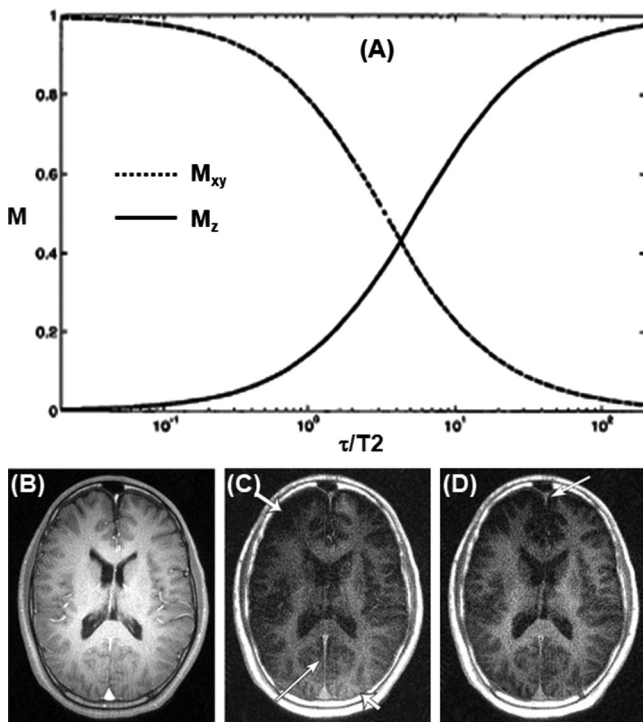

FIG. 5. Numerical simulation of transverse (M_{xy}) and longitudinal (M_z) magnetizations vs τ/T_2 in response to a rectangular pulse $\gamma B_1 \tau = 90°$, where τ is the pulse duration (a). The long-T_2 components are rotated into the transverse plane. In contrast, the short-T_2 components are located along the longitudinal axis. An example of UTE imaging of the brain in a healthy volunteer is shown without long-T_2 suppression (b), with a rectangular suppression pulse (duration = 16 ms) (c), and with a single-band suppression pulse (duration = 40 ms, time-bandwidth product = 2.4) (d). Short-T_2 components in white matter and the falx cerebri (long, thin arrows) are apparent only after long-T_2 suppression. (a) Reproduced with permission from Sussman *et al.*, Magn. Reson. Med. **40**, 890–899 (1998). Copyright 1998 Wiley.[49] (b)–(d) Reproduced with permission from Larson *et al.*, Magn. Reson. Med. **56**, 94–103 (2006). Copyright 1998 Wiley.[50]

using UTE imaging with and without long-T_2 saturation. The ultrashort-T_2 components in white matter are obscured when using regular UTE imaging but highlighted when long-T_2 saturation pulses are applied. This short-T_2 component is present in myelin; it is lost in patients with multiple sclerosis (MS).[50] The long-T_2 saturation pulse improves contrast for short-T_2 components in the falx cerebri [long, thin arrows in Figs. 5(c) and 5(d)]. Long dual-band saturation pulses have also been employed to suppress signals from long-T_2 tissues and tissue components;[51] however, long-T_2 saturation is generally very sensitive to off resonance effects, which can lead to incomplete long-T_2 signal suppression. Another limitation of long-T_2 saturation is its sensitivity to short-T_1 contamination: the short-T_2 contrast may be reduced due to fast signal recovery during the saturation recovery period from tissues with long-T_2s but short-T_1s (e.g., fat). Furthermore, the long-T_2 saturation technique is sensitive to B_1 inhomogeneity, which may result in significant residual long-T_2 signals and thereby degrade short-T_2 contrast.

C. UTE with off-resonance saturation

Short-T_2 tissues or tissue components such as the osteochondral junction, menisci, tendons, ligaments, cortical bone, and myelin have much broader spectral absorption lineshapes than long-T_2 tissues. They can be selectively affected by appropriately placed off resonance RF irradiation. A high-power saturation pulse placed a few kilohertz away from the water peak can preferentially saturate signals from short-T_2 tissues, leaving long-T_2 water and fat signals largely unaffected. Subtraction of UTE images with and without off resonance RF irradiation of this type can effectively suppress long-T_2 signals and create high contrast imaging of short-T_2 tissues.[52,53] Off-resonance RF saturation can also be used to create phase contrast for short-T_2 tissues. Phase changes detected using GRE sequences have provided a new source of image contrast. In conventional MRI, short-T_2 components, including myelin, contribute minimally to phase contrast. Regular UTE images do not show significant phase contrast between gray and white matter; however, UTE imaging with off resonance RF saturation pulses can provide high phase contrast in the brain even at

a nominal TE of 106 μs.[54] Compared to conventional MR imaging, UTE with off resonance RF saturation provides reversed phase contrast between gray and white matter. Figure 6 shows the magnitude and phase UTE images of the saturated components calculated using complex subtraction.[54] The saturated signal component of combined gray matter and CSF has a positive phase shift, while that of the white matter primarily shows a negative phase shift. CSF appears to have a similar positive phase shift in both UTE and GRE phase images, but white matter shows the opposite sign. UTE-based MRI phase images may improve the characterization of tissue microstructure in the brain by accessing short-T_2 components, thereby providing a better way of demonstrating phase contrast.[54]

D. UTE with long-T_2 adiabatic inversion

The adiabatic inversion recovery UTE (IR-UTE) sequence employs a long adiabatic inversion pulse (e.g., Silver–Hoult pulse, duration τ of $\sim$8 ms) to invert the longitudinal magnetizations of long-T_2 water and fat [Fig. 7(a)].[55–61] The degree of inversion depends on the tissue T_2, with full inversion when $T_2 \gg \tau$, and saturation when $T_2 \ll \tau$.[57,58] When the pulse duration τ is much longer than the transverse relaxation times of short-T_2 tissues, the transverse magnetizations of short-T_2 tissues may experience significant relaxation, leading to approximate saturation rather than complete inversion. When the UTE acquisition starts at an inversion time (TI) designed to allow the fully inverted long-T_2 magnetization to reach the null point, short-T_2 tissues can be selectively imaged. A major advantage of the Silver–Hoult adiabatic inversion pulse is its insensitivity to B_1 and B_0 inhomogeneities. It provides uniform inversion of long-T_2 magnetizations when the RF pulse amplitude is above the adiabatic threshold.[62] It is also insensitive to off resonance effects due to its relatively broad spectral bandwidth ($\sim$1 kHz). The IR-UTE sequence provides high short-T_2 contrast.[60] Figures 7(b) and 7(c) shows representative IR-UTE and conventional clinical FSE images of the forearm. Cortical bone and tendons show near zero signal on the FSE image but high signal and excellent contrast on the IR-UTE image. The IR-UTE sequence can also be used to create high contrast for other short-T_2 tissues or tissue components such
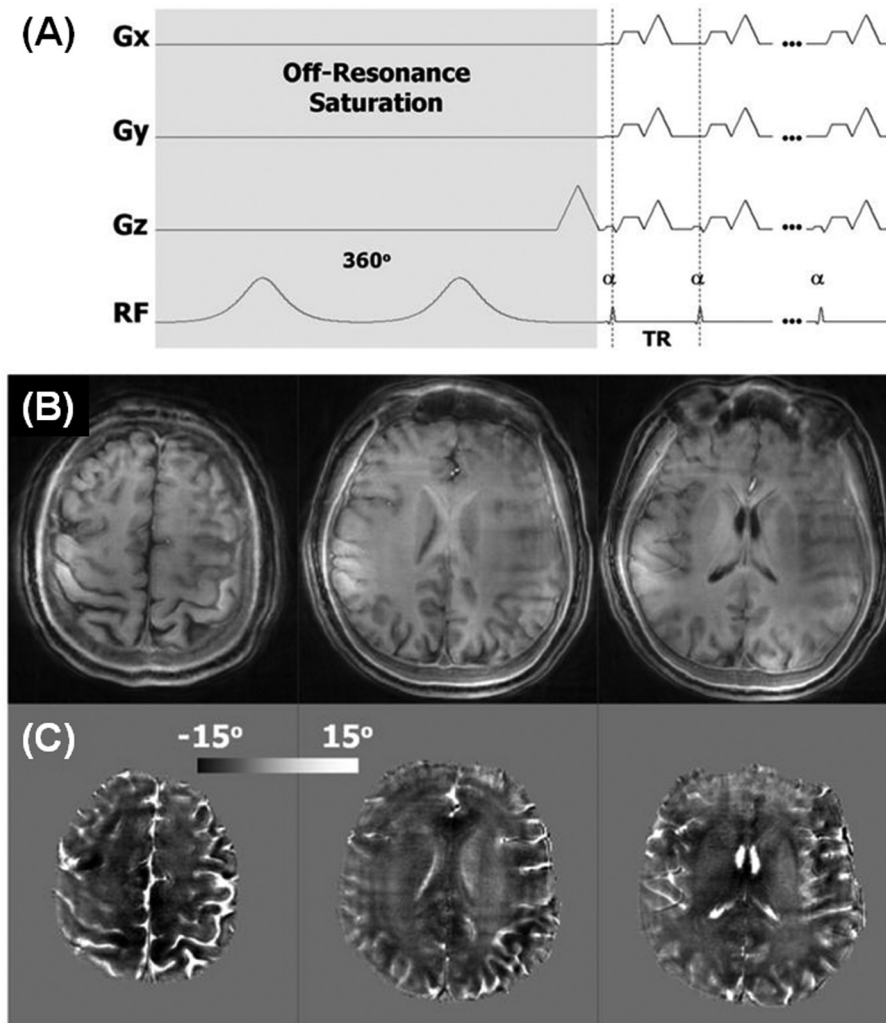
FIG. 6. Diagram of the 3D radial UTE sequence with off resonance saturation (a). This technique employs two consecutive 180° adiabatic inversion pulses for off resonance saturation and a minimum-phase pulse for excitation followed by 3D radial ramp sampling with a minimal nominal TE of 0.106 ms. An example of off resonance saturated UTE magnitude (b) and phase (c) imaging in the brain of a healthy volunteer is shown with a TE of 0.106 ms and a saturation frequency of −1.2 kHz. Three selected axial magnitude images show high signal intensity in white matter, indicating higher ultrashort-T_2 components (b). The corresponding phase images demonstrate negative phase shifts in white matter and positive phase shifts in CSF (c). (a)–(c) Reproduced with permission from Wei *et al.*, NeuroImage **175**, 1–11 (2018). Copyright 2018 Elsevier.[54]

FIG. 7. The contrast mechanism for IR-UTE imaging where an adiabatic inversion pulse is used to invert and null long-T_2 tissues, followed by a UTE free induction decay (FID) acquisition to detect signals from short-T_2 tissues (a). Clinical FSE imaging of a forearm shows near zero signal for cortical bone and tendons (b), whereas the IR-UTE sequence provides high signal and contrast for both (c).

as the osteochondral junction, menisci, ligaments, tendons, and myelin.

E. UTE with long-T_2 adiabatic inversion and echo subtraction

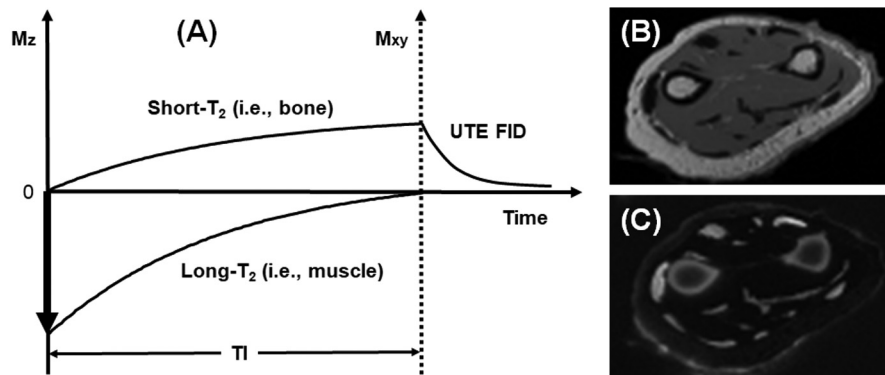The IR-UTE sequence can be combined with dual-echo acquisition and echo subtraction for selective imaging of non-aqueous myelin protons.[55,63–73] Figures 8(a) and 8(b) describes the contrast mechanism. The adiabatic inversion pulse uniformly inverts the longitudinal magnetizations of long-T_2 components in white and gray matter[55] but saturates the myelin magnetization, which has an ultrashort T_2 ($T_2 \ll 1$ ms) and experiences significant transverse relaxation during the long adiabatic inversion process.[55,57] The dual-echo UTE data acquisition starts at the TI necessary for the inverted longitudinal magnetization of long-T_2 white matter to reach its null point. The saturated myelin magnetization recovers quickly during this TI because of its short T_1.[66] The UTE sequence detects free induction decay (FID) signals from myelin and long-T_2 gray matter, which has a longer T_1 than long-T_2 white matter. The second echo acquires signals from non-nulled long-T_2 gray matter as the myelin signal quickly decays to near zero. Subtraction of the second echo image from the first provides selective imaging of myelin in white matter. At the null point, the white matter signal only comes from myelin. The gray matter signal, on the other hand, is more complicated because there is a degree of cancelation between the positive longitudinal magnetization from myelin and the negative longitudinal magnetization from long-T_2 components. The net effect is a reduced signal when the FID is acquired.[73] At the second echo (e.g., TE ∼ 2 ms), the myelin signal quickly decays to zero, while the long-T_2 gray matter signal remains essentially unchanged. Consequently, the gray matter has a higher signal at the second echo than at the FID [Fig. 8(b)]. As a result, subtraction of the second echo from the FID produces a positive signal for myelin in white matter but a negative signal for gray matter, thus creating high myelin contrast between the two [Fig. 8(e)].[73]

F. UTE with dual adiabatic inversion

The dual adiabatic inversion UTE (dual-IR-UTE) sequence employs two Silver–Hoult adiabatic inversion pulses to invert the longitudinal magnetizations of long-T_2 water and fat, respectively [Fig. 9(a)].[74–76] The longitudinal magnetizations of short-T_2 tissues are not inverted but largely saturated because of the fast signal decay

during the long adiabatic inversion process.[57] The UTE data acquisition starts at delay times of TI_1 and TI_2 that are chosen to invert and null the long-T_2 water and fat magnetizations, respectively.[74] The long-T_2 water magnetization has a longer T_1 and requires a longer inversion time TI_1 to reach the null point. In contrast, the long-T_2 fat magnetization has a shorter T_1 value requiring a shorter inversion time TI_2 to reach its null point. An appropriate combination of TI_1, TI_2, and TR allows robust suppression of long-T_2 water and fat signals simultaneously. Figures 9(b)–9(f) shows PD-FSE, T_1-FSE, GRE, basic UTE, and dual-IR-UTE images of a human patella sample.[74] The deep radial and calcified cartilage are inapparent with conventional FSE and GRE sequences but are highlighted as a linear, well-defined area of high signal (arrows) using dual-IR-UTE imaging. A similar technique, double adiabatic inversion UTE sequence, has also been proposed for high contrast imaging of short-T_2 tissues. It employs two identical adiabatic inversion pulses to invert the longitudinal magnetizations of two or more long-T_2 tissues.[77] This technique can simultaneously suppress long-T_2 tissues with a broad range of T_1s (e.g., fat and muscle).

G. UTE with adiabatic inversion and fat saturation

The adiabatic inversion recovery and fat saturation UTE (IR-FS-UTE) technique [Fig. 10(a)] provides high contrast for short-T_2 tissues by using an adiabatic inversion preparation to suppress long-T_2 water and using chemical shift-selective (CHESS) imaging to suppress fat.[78–80] An example is 3D IR-FS-UTE imaging of the cartilaginous endplate of the spine. The adiabatic inversion pulse is centered at -220 Hz, a frequency midway between the water and fat peaks at 3 T. The adiabatic pulse uniformly fully inverts the longitudinal magnetizations of long-T_2 water and fat but only partially inverts the longitudinal magnetizations of short-T_2 tissues, such as the cartilaginous endplate (CEP).[81] TI is chosen to null signals from long-T_2 tissues such as the nucleus pulposus (NP), leaving signals from short-T_2 tissues such as the CEP selectively deteted by the 3D UTE data acquisition. Short-T_2 tissues typically have short T_1s, leading to a fast signal recovery during TI and thus high signals at data collection.[72–84] The inversion preparation that nulls the NP signal with a long T_1 cannot null the fat signal which has a much shorter T_1. CHESS imaging is used before the UTE data acquisition to suppress fat signals further, thereby improving the CEP contrast. A train of spokes is acquired after each IR-FS preparation to speed up data acquisition. Figures 10(b)–10(d) show clinical and 3D IR-FS-UTE imaging of
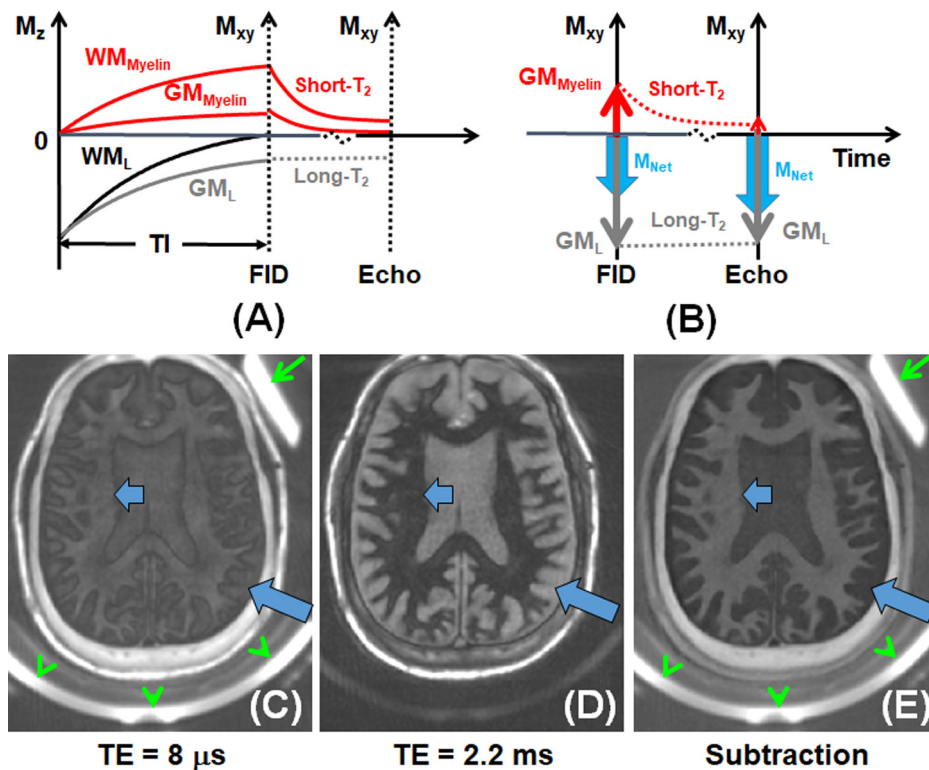
FIG. 8. The contrast mechanism for myelin imaging using a dual-echo IR-UTE acquisition with echo subtraction (a). This technique employs an adiabatic inversion pulse to invert and null signals from long-T_2 components in white matter (WM_L). Long-T_2 components in gray matter (GM_L) have negative longitudinal magnetization at the time of FID data acquisition because GM_L has a longer T_1 than WM_L. Myelin magnetization in white matter (WM_{Myelin}) and gray matter (GM_{Myelin}) is saturated mainly due to its ultrashort T_2 and recovers quickly during TI. At the null point, the white matter signal comes from WM_{Myelin}, whereas the gray matter signal includes both the positive GM_{Myelin} and the negative GM_L. At the second echo, signals from WM_{Myelin} and GM_{Myelin} quickly decay to zero, but GM_L's signal remains unchanged. As a result, a higher net magnetization (M_{NET}) in gray matter is produced at the second echo than at the FID (b). An example is shown on IR-UTE imaging of the brain of a healthy volunteer with a TE of 8 μs (c) and 2.2 ms (d). Echo subtraction shows excellent WM_{Myelin} contrast with a positive signal for myelin in white matter (short thick arrows) and a negative signal in gray matter (long thick arrows) (e). Rubber (long thin arrows) and pads (arrow heads) have short T_2s and are only visible with UTE images (c) and (e).

the lumbar spine in a patient. The IR-FS-UTE images depict a small incipient Schmorl's node on the superior vertebral body endplate with a preserved thin cartilaginous endplate, which could not be identified in the clinical T_1- or T_2-FSE images. This result demonstrates the potential of the IR-FS-UTE sequence for imaging the CEP of the spine with high contrast and its potential for diagnosing early degenerative changes in the intervertebral disk. The 3D IR-FS-UTE sequence can also be used to depict other short-T_2 tissues, such as the osteochondral junction, menisci, tendons, ligaments, and bone.[78] The IR-FS preparation module can be combined with other UTE-type sequences, such as zero echo time (ZTE), for high contrast imaging of short-T_2 tissues.[85] Generally, the IR-FS scheme shows low sensitivity to B_1 and B_0 inhomogeneities and provides higher contrast for the CEP, the osteochondral junction, and other short-T_2 tissues than UTE-based dual-echo subtraction and long-T_2 saturation approaches.

H. UTE with short TR adiabatic inversion

The short TR adiabatic inversion recovery UTE (STAIR-UTE) sequence [Fig. 11(a)] utilizes the 3D IR-UTE data acquisition with a short TR and a high flip angle within limits imposed by specific absorption rate (SAR) concerns in clinical imaging.[86–88] A very short TR and TI combination suppress signals from long-T_2 tissues with different T_1s above a specific minimum value. To speed up data acquisition, multiple spokes are acquired after each adiabatic inversion pulse. This provides fast volumetric imaging of short-T_2 tissues such as cortical and trabecular bone in the spine and myelin in the brain's gray and white matter. The spokes acquired before and after the null point (center spoke) have opposite M_zs for long-T_2 tissues, leading to signal cancelation and additional long-T_2 signal suppression and, thus, more selective imaging of short-T_2 tissues. Numerical simulation suggests that more efficient long-T_2 signal suppression can be achieved with shorter TRs (e.g., <150 ms) and higher flip angles[86] because shorter TRs provide more effective long-T_2 signal suppression. In addition, higher flip angles provide more T_1 weighting. The latter benefits short-T_2 imaging as short-T_2 tissues typically have shorter T_1s than long-T_2 tissues. Figures 11(b)–11(f) shows 3D STAIR-UTE brain imaging in a 29-year-old female volunteer at different TEs. Long-T_2 signals from white matter, gray matter, and CSF are efficiently suppressed, and only ultrashort T_2^* signals from non-aqueous myelin protons are detected. This is shown by the excellent fitting of the signals from white matter
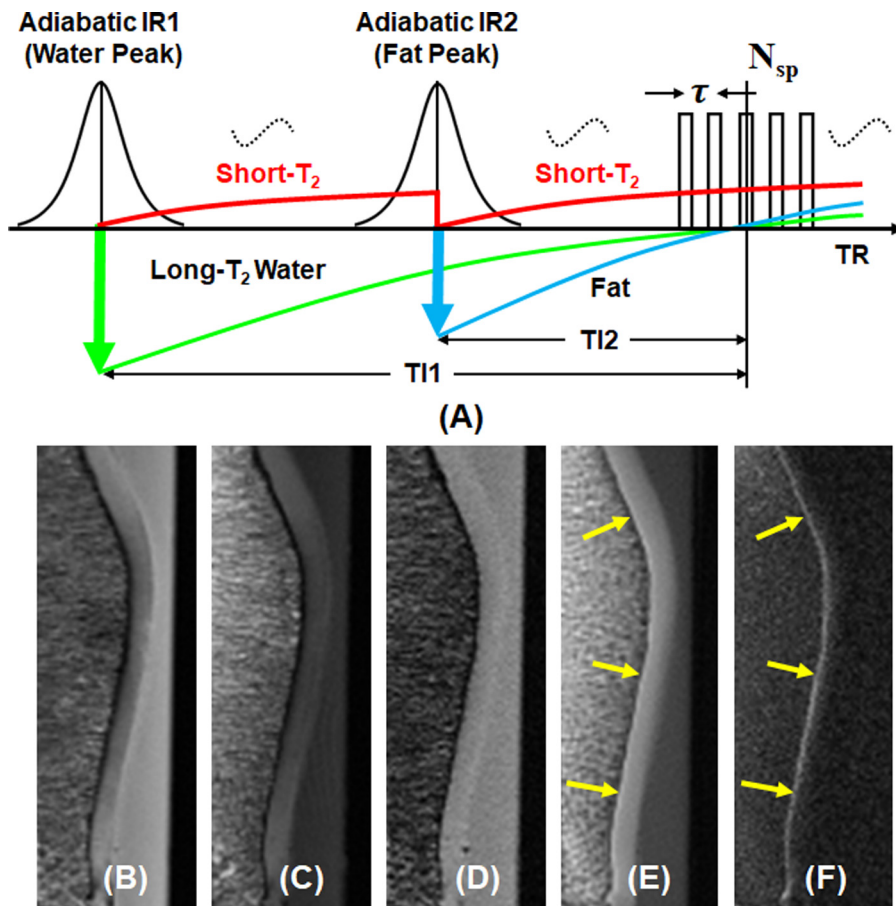
FIG. 9. The contrast mechanism for dual-IR-UTE imaging of short-T_2 tissues (a). This technique employs two adiabatic inversion pulses to invert and null long-T_2 water and fat, respectively, followed by UTE acquisition to create short-T_2 contrast. An example is shown on clinical PD-FSE (b), T_1-FSE (c), GRE (d), regular UTE (e), and dual-IR-UTE (f) imaging of a cadaveric human patella sample. The deep radial and calcified cartilage are invisible with clinical sequences but highlighted as a linear, well-defined area of high signal (arrows) with the dual-IR-UTE sequence. (b)–(f) Reproduced with permission from Du et al., Osteoarthritis Cartilage **21**, 77–85 (2013). Copyright 2013 Elsevier.[76]

with a single component curve which shows a T_2^* of 0.22 ± 0.01 ms, close to the T_2^* of lyophilized myelin powder.[67]

The 3D STAIR-UTE sequence also shows high contrast imaging of cortical and trabecular bone in the lumbar spine, with excellent suppression of signals from long-T_2 tissues.[88] These results demonstrate that the STAIR-UTE technique reduces long-T_2 signals from muscle and fat effectively despite their differences in T_1. Direct imaging of trabecular bone in the spine, hip, or ankle is challenging due to high signals from marrow fat and other long-T_2 tissues. Many UTE-based sequences, such as dual-echo acquisition with echo subtraction,[30,47,48] long-T_2 saturation,[49–51] adiabatic inversion recovery,[59] and spectral pre-saturation with inversion recovery (SPIR)[89] may be unable to suppress signals from fat and other long-T2 tissues effectively. If suppression is unsatisfactory in this respect, the residual signal can be much higher than that from trabecular bone, leading to significant long-T_2 signal contamination. Recently, Wurnig et al. combined the SPIR preparation with 3D UTE data acquisition (SPIR-UTE) to directly image trabecular bone in the spine.[89] This approach resulted in a relatively long T_2^* value of 2.42 ± 0.56 ms for trabecular bone at 3 T, which is about eight times longer than the T_2^* of 0.31 ± 0.01 ms measured with a 3D STAIR-UTE sequence, suggesting that SPIR-UTE imaging of trabecular bone is subject to significant fat signal contamination.[88] The 3D STAIR-UTE-measured value of T_2^* for trabecular

bone is very close to the T_2^* of ~0.3 ms for cortical bone measured with various IR-based UTE techniques,[82–90] implying that marrow fat and water are effectively suppressed with this sequence and that trabecular bone is therefore being selectively detected.[88]

I. UTE water/fat imaging

Fat suppression is often required to enhance the short-T_2 contrast. However, the commonly used CHESS technique is problematic when imaging short-T_2 tissues because of their broad spectral bandwidths, which overlap with that of fat. Fat suppression pulses can saturate signals from short-T_2 tissues directly due to spectral overlap or indirectly due to magnetization transfer.[32,93,94] Conventional chemical shift-based decomposition techniques such as single- or multi-point Dixon approach[95] and IDEAL (Iterative Decomposition of water and fat with Echo Asymmetry and Least-squares estimation)[96] provide excellent water-fat signal separation for long-T_2 tissues. These techniques have provided the impetus for developing new methods, such as UTE-based IDEAL (UTE-IDEAL), which combines conventional water-fat separation methods with UTE data acquisition.[97] The methods are designed to preserve signals from short-T_2 tissues while providing high contrast, water-only images, as well as T_2^* and fat fraction maps. UTE-IDEAL employs multifrequency modeling of fat to
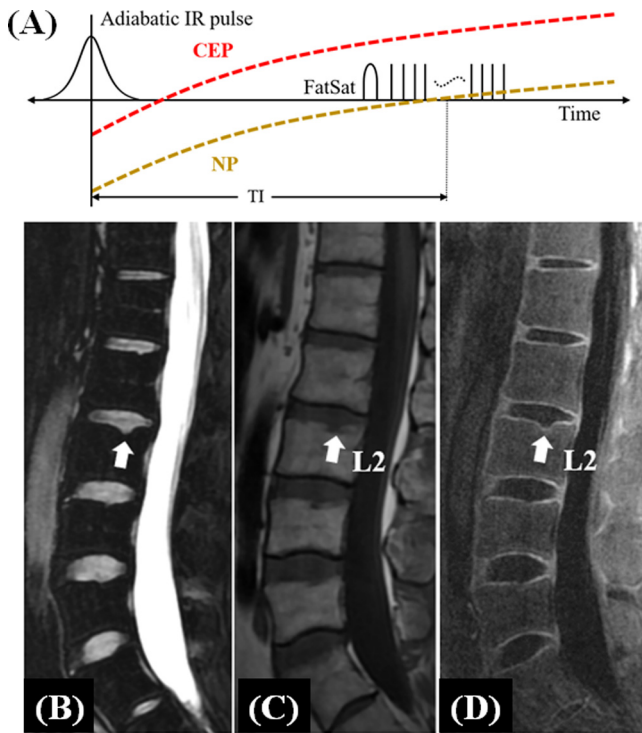
FIG. 10. The 3D IR-FS-UTE sequence. This combines adiabatic inversion pulse preparation and CHESS imaging with UTE acquisition to visualize short-T_2 tissues such as the cartilaginous endplate (CEP) (a). The adiabatic inversion pulse inverts and nulls signal from the nucleus pulposus (NP) in the intervertebral disk. CHESS imaging is used to suppress signal from fat. A multi-spoke 3D UTE acquisition follows to provide high contrast imaging of the CEP. The sequence was used in the spine (T11-L5) of a 38-year-old male volunteer with conventional 2D T_2-FSE (b), 2D T_1-FSE (c), and 3D IR-FS-UTE (d) sequences. Excellent contrast is achieved for the CEP using the 3D IR-FS-UTE sequence [arrow in panel (d)] but not with the clinical T_2- and T_1-FSE sequences [arrows in panels (b) and (c)]. The preserved cartilaginous endplate around the Schmorl's node in the superior endplate of L2 can only be seen with the IR-FS-UTE sequence. (a)–(d) Reproduced with permission from Lombardi et al., NMR Biomed. **34**, e4579 (2021). Copyright 2021 Wiley.[80]

improve water/fat signal separation.[97] Figure 12 shows UTE-IDEAL imaging of the ankle of a 28-year-old volunteer. Excellent fat water separation with T_2^* and fat fraction mapping can be achieved simultaneously, not only for long-T_2 tissues but also for short-T_2 tissues, such as the Achilles tendon and enthesis, which are invisible with conventional MRI sequences.

The single-point Dixon technique allows fast water and fat separation.[98,99] More recently, a single echo UTE (sUTE) technique was proposed to solve the smoothness-constrained inverse water/fat problem. The sUTE method can separate fat from water, remove unwanted low-frequency phase terms, and facilitate susceptibility-weighted imaging from a single complex UTE image.[100,101] Figure 13 shows representative water- and fat-separated images using sUTE-based Dixon (sUTE-Dixon) and Cartesian six echo-based Dixon (6TE-Dixon) imaging for water-fat separation.[101] An acute wedge compression fracture and bone marrow edema are clearly identified at L3 in this patient, with an excellent depiction of the fluid and bone marrow separation line in the fat images. These results suggest that the sUTE technique can be used to simultaneously evaluate vertebral fractures and bone marrow edema in the thoracolumbar spine.[101]

J. UTE with water excitation

Fat suppression is crucial for high contrast UTE imaging of short-T_2 tissues in the musculoskeletal system. Short-T_2 tissues such as cortical bone and tendon typically have much lower proton densities and shorter T_2s than fat. In addition, fat has a short T_1. These effects result in a relatively high fat signal in T_1-weighted UTE imaging. Further, UTE imaging is based on non-Cartesian sampling and is therefore sensitive to chemical shift and partial volume artifacts.[102] Consequently, it is necessary to incorporate fat suppression techniques into most morphological and quantitative UTE imaging outside the brain. In clinical practice, the most frequently used approach for fat suppression is CHESS imaging, which employs a spectrally selective RF pulse followed by a gradient spoiler to suppress signals from fat. However, CHESS imaging may directly saturate the broad signal of short-T_2 tissues or indirectly attenuate short-T_2 signals due to MT effects, especially with collagen-rich tissues.[103–105]
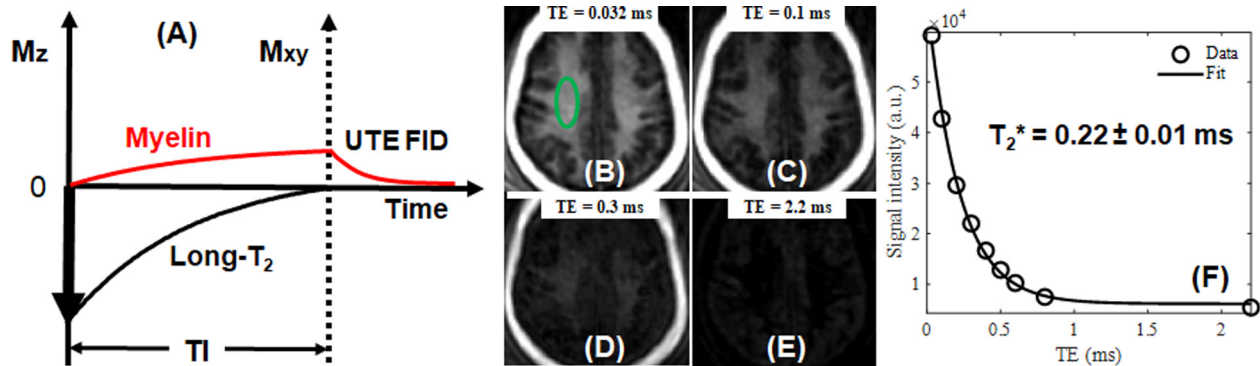
FIG. 11. The 3D STAIR-UTE sequence uses a short TR (e.g., TR $\sim$ 150 ms or shorter) and short TI (e.g., $\sim$64 ms) to suppress long-T_2 signal components (a). Its efficacy is demonstrated in STAIR-UTE imaging of the brain in a 29-year-old volunteer with TEs of 0.032 (b), 0.1 (c), 0.3 (d), and 2.2 ms (e), as well as exponential fitting of the STAIR-UTE signal for the white matter which shows a T_2^* of 0.22 $\pm$ 0.01 ms (f), consistent with long-T_2 signal suppression. (b)–(f) Reproduced with permission from Ma et al., Radiology **297**, 392–404 (2020). Copyright 2020 Radiology Society of North America.[86]
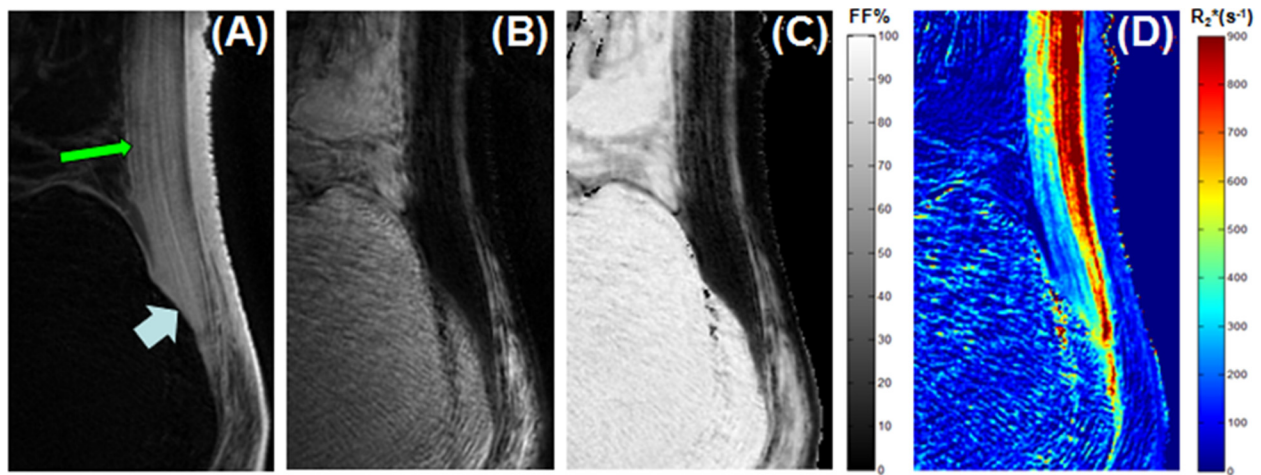
FIG. 12. UTE-IDEAL imaging of the ankle of a 28-year-old healthy volunteer. This shows robust water and fat signal separation and produces a water-only image with high signal and contrast of the Achilles tendon and enthesis (a), a fat-only image (b), a fat fraction map (c), and an R_2^* map (d).

Water excitation can effectively resolve these challenges.[106,107] A series of short RF pulses with binomial amplitude ratios have been proposed for water-selective excitation in 3D UTE imaging.[106] A nearly complete absence of fat signal can be achieved without the need for long preparation schemes or saturation pulses.[107] Figure 14(a) shows the pulse scheme, including the time interval between the two rectangular excitation pulses (T_{int}) and the duration of a single RF pulse (T_{RF}), which forms a 1–1 double RF excitation pulse. The transverse magnetization at the beginning of this double RF pulse excitation is near zero due to RF spoiling and spoiler gradients. Off-resonance Larmor frequencies are not excited by the 1–1 double RF pulse during

the saturation period. Figures 14(b)–14(d) show water-selective 3D UTE imaging of finger tendons and the posterior cruciate ligament with very low signal from fat.[106] Recently, a new soft-hard composite pulse has been developed for water excitation.[108] The soft pulse has a narrow bandwidth and is centered on the fat peak, so it only flips the fat magnetization. In distinction, a rectangular pulse with the same flip angle as the soft pulse is used to rotate the water and fat magnetizations in opposite directions. The fat magnetization experiences flipping up and down with an identical flip angle, leading to near zero transverse magnetization and excellent fat suppression. In addition, the low-power soft pulse has little direct or indirect saturation effect on
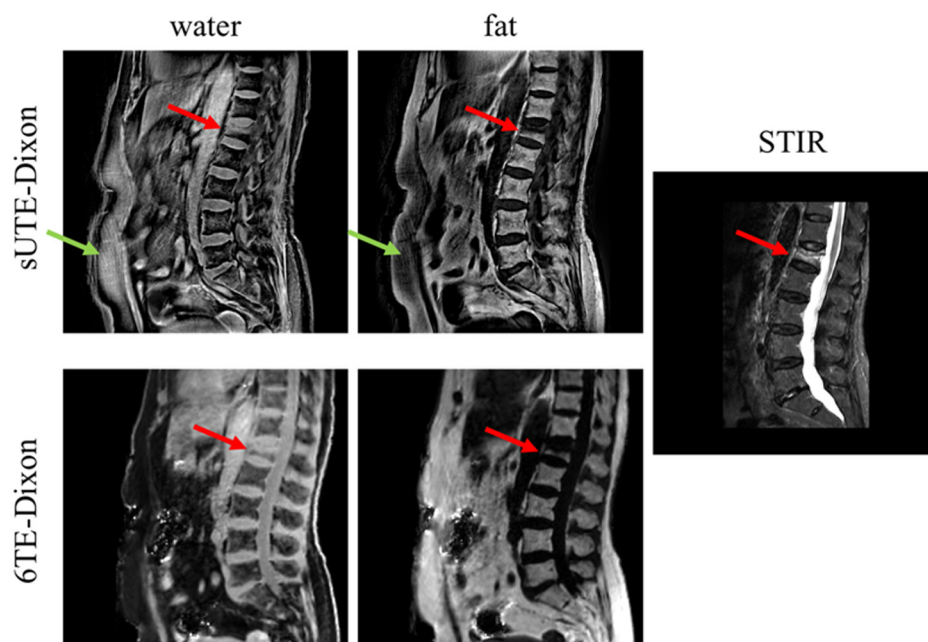
FIG. 13. Comparison of sUTE-Dixon, Cartesian 6TE-Dixon, and STIR (short tau inversion recovery) images in a patient with an acute wedge compression fracture of L3 with bone marrow edema. The STIR image shows an edema-equivalent signal alteration (red arrows). Compared with the STIR and the 6TE-Dixon scans, the UTE scan has higher in-plane resolution and thicker slices. The bone marrow edema is visible in the sUTE-Dixon images, and the contrast between water and fat is comparable with the 6TE-Dixon images. The sUTE-Dixon water images contain signals within the anterior subcutaneous fat region (green arrows), which is prone to artifacts associated with abdominal breathing. Reproduced with permission from Kronthaler *et al.*, Magn. Reson. Med. **87**, 1771–1783 (2022). Copyright 2022 Wiley.[101]
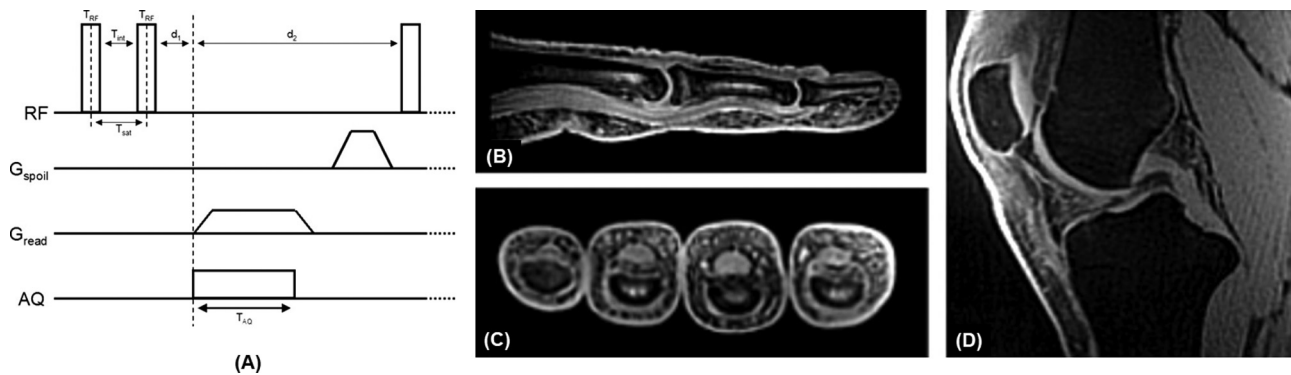
FIG. 14. Diagram of the 3D radial water-selective UTE sequence (a), which uses a 1–1 double RF pulse excitation and centric 3D radial mapping of k-space. Results are shown in (b)–(d) using a water-selective 3D UTE sequence on a 3 T clinical scanner. Tendons of the finger flexors are clearly depicted in sagittal (b) and axial (c) UTE images. The posterior cruciate ligament of the knee joint is also depicted with positive contrast (d). Reproduced with permission from Springer *et al.*, Magn. Reson. Med. **71**, 534–543 (2014). Copyright 2014 Wiley.[106]

short-T_2 magnetizations. As a result, the soft-hard composite pulse provides high signal and contrast imaging of knee joint tissues with much reduced short-T_2 signal attenuation.[108]

K. UTE spectroscopic imaging

With conventional chemical shift imaging, small phase encoding gradients are employed for spatial localization, followed by an FID acquisition and Fourier transformation in the time domain to generate spectroscopic information.[109] For long-T_2 tissues, this provides high spectral resolution but low spatial resolution. For short-T_2 tissues, it is essential to reduce the minimal TE. UTE spectroscopic imaging

combines highly undersampled interleaved projection reconstruction with multi-echo UTE data acquisitions at progressively increasing TEs [Fig. 15(a)].[110–112] The projections are divided into multiple interleaved groups [Fig. 15(b)]. Each group of projections sparsely but uniformly covers k-space, and view sharing with a sliding window reconstruction algorithm is used to reconstruct images at each TE.[113–115] Fourier transformation in the time domain (with images acquired at different TEs) is used to generate spectroscopic images. T_2^* can be derived from the exponential fitting of time-domain images or line shape fitting of the magnitude spectrum, and proton density and frequency shift can be quantified. Figures 15(c)–15(l) show time-domain and spectral domain UTE spectroscopic images of the tibial
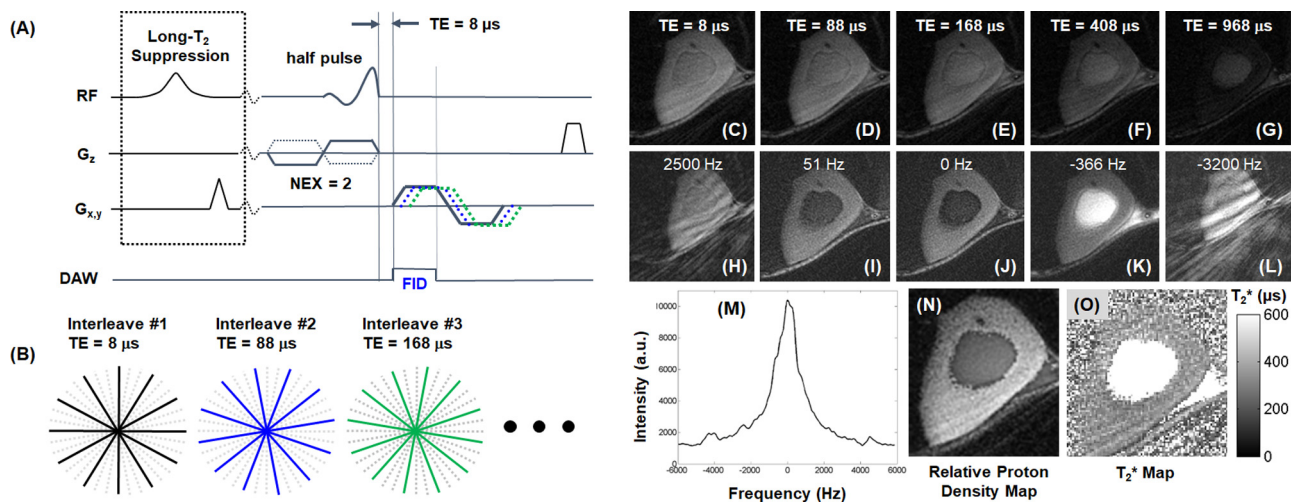
FIG. 15. Diagram of the 2D UTE spectroscopic imaging sequence (a) and the interleaved variable TE acquisition scheme (b). This technique employs highly undersampled interleaved acquisitions, where each group of projections uniformly covers k-space with its TE progressively delayed by a predefined time (e.g., 80 μs). An example is shown on long-T_2 suppressed UTE spectroscopic imaging of the tibial midshaft of a 29-year-old volunteer in the time-domain with TEs of 8 (c), 88 (d), 168 (e), 408 (f), and 968 μs (g), and in the spectral domain with frequency offsets of 2500 (h), 51 (i), 0 (j), −366 (k), and −3200 Hz (l). Undersampling streaks are shifted to high spectral frequencies, producing streak-free water (j) and fat (k) images. Signals from long-T_2 water and fat were suppressed using an adiabatic inversion pulse. A pixel-based UTE spectrum for cortical bone (m), a relative proton density map (n), and a T_2^* map (o) are also displayed. Reproduced with permission from Du *et al.*, Magn. Reson. Med. **58**, 1001–1009 (2007). Copyright 2007 Wiley.[110]

midshaft of a 29-year-old volunteer with muscle and fat signals suppressed by an adiabatic inversion pulse.[110] The interleaved acquisition produces oscillating streak artifacts, which are shifted to high frequencies in the spectral domain, resulting in streak-free bone images near the on-resonance frequencies. Figures 15(m)–15(o) show a single-pixel bone spectrum, relative PD, and T_2^* maps. T_2^* derived from line shape fitting ranges from 300 to 500 μs, broadly consistent with the literature.[58–60] Spectroscopic images can also be generated for many other short-T_2 tissues, including the osteochondral junction, menisci, ligaments, and tendons.[110–112] This technique provides short-T_2 images with high spatial resolution, moderate spectral resolution, and minor streak artifacts in clinically acceptable scan times.

L. Contrast mechanisms with other pulse sequences

The different UTE-type sequences can be combined with each of the above contrast mechanisms for high contrast imaging of various short-T_2 tissues and tissue components in the body. For example, adiabatic inversion recovery-based preparations can be combined with RHE,[45] ZTE,[45,116–118] and PETRA[44,119] sequences for high contrast imaging of cortical bone, myelin, and other short-T_2 tissues, respectively. On-resonance long-T_2 suppression or off resonance short-T_2 saturation can be applied to WASPI, SWIFT, PETRA, SPI, RHE, and ZTE sequences where echo subtraction is not easily applicable for creating short-T_2 contrast. For example, SWIFT has been combined with off resonance saturation to image the interface between cartilage and subchondral bone.[53] The use of many of the above contrast mechanisms with SPI, WASPI, AWSOS, PETRA, RHE, and ZTE sequences remains to be investigated.

M. Summary of contrast mechanisms

All the major MR vendors have implemented UTE-type sequences on their equipment for research purposes, and various morphological UTE imaging techniques have been developed. The technical performance in terms of B_1 and B_0 inhomogeneities, chemical shift artifacts, CNR and SNR efficiencies, significant advantages and disadvantages, promising and challenging clinical applications, and related references for each contrast mechanism are detailed in Table I. Among the different contrast mechanisms discussed above, dual-echo UTE with echo subtraction is the most time-efficient method. However, it is sensitive to chemical shift, off resonance, and susceptibility effects leading to inefficient long-T_2 suppression.[30,32] Long-T_2 saturation-based contrast mechanisms, including T_2-selective RF excitation,[49] dual-band UTE,[50,51] UTE with on-resonance or off resonance saturation,[52] and WASPI,[40,41] are sensitive to B_1 and B_0 inhomogeneities, which leads to incomplete long-T_2 signal suppression and therefore compromised short-T_2 contrast. UTE spectroscopic imaging[110–112] and water/fat separation techniques[97–101] have great potential for SNR-efficient imaging of short-T_2 tissues by avoiding the short-T_2 signal attenuation associated with chemical shift-based fat saturation pulses but lack long-T_2 water suppression. Adiabatic inversion recovery-based techniques, including basic IR-UTE,[56–73] dual-IR-UTE,[74–76] IR-FS-UTE,[78–80] and STAIR-UTE,[86–88] seem to be most promising as they provide more uniform suppression of long-T_2 water and fat signals than other contrast mechanisms due in large part to the insensitivity of adiabatic inversion pulses to B_1 and B_0 inhomogeneities.[56–58] Overall, the IR-based UTE techniques, especially

STAIR-UTE, seem the most promising approach for high contrast imaging of ultrashort T_2^* tissues such as the osteochondral junction, trabecular bone, and myelin. Dual-echo UTE with echo subtraction works best for high contrast imaging of short-T_2 tissues with relatively high proton densities (e.g., the menisci, ligaments, and tendons) but is more difficult with ultrashort-T_2 tissues that have low proton densities (e.g., bone and myelin) where efficient long-T_2 suppression is of critical importance. The basic UTE sequence seems to be the best option for high-resolution imaging of the lung, where motion compensation is a high priority.

V. PART II—TECHNICAL DEVELOPMENT IN QUANTITATIVE UTE MRI

The focus of current UTE techniques is to reduce TE and improve signal detection by implementing different data sampling and image reconstruction strategies, as well as novel contrast mechanisms. However, it is also essential to quantitatively evaluate short-T_2 tissue relaxation times and other MR properties, including T_1, T_2^*, T_2, $T_{1\rho}$, MTR, MT modeling of MMF, perfusion, diffusion, susceptibility, and water content.[5–8,120–127] These biomarkers may be beneficial for evaluating early degeneration and monitoring therapy.

Current standard clinical MR sequences cannot be used to quantify short-T_2 tissues due to a lack of signal.[5–8] For example, conventional inversion recovery-based T_1 quantification techniques are problematic for short-T_2 tissues such as cortical bone because the standard inversion pulse does not invert the longitudinal magnetization of cortical bone, and the transverse magnetization loses coherence too rapidly for spatial encoding.[123–127] Accurate quantification of short-T_2 tissues requires consideration of fast transverse relaxation during both magnetization preparation and spatial encoding. A series of quantitative UTE imaging techniques have been developed to assess the relaxation times and other MR properties of short-T_2 tissues using clinical MR scanners.

A. UTE T_1 measurement

Many techniques for mapping the T_1 of long-T_2 tissues have been developed,[14–16,128,129] with variable repetition time (VTR) and variable flip angle (VFA) methods being two of the most widely used techniques.[82,83] However, VTR and VFA methods are disadvantaged by sensitivity to B_1 field inhomogeneity. While the actual flip angle imaging (AFI) technique has been developed to overcome this challenge,[129] short-T_2 tissues still pose a problem with all currently available conventional T_1 mapping techniques due to the lack of detectable signal when conventional data acquisitions with a long TE are used. A combination of UTE, AFI, and VTR or VFA techniques (UTE-AFI-VTR/VFA) has been developed for accurate quantification of T_1 of short-T_2 tissues [Figs. 16(a) and 16(b)].[82,83] Figures 16(c)–16(h) show T_1 mapping of an agarose phantom, a bovine cortical bone sample, and the tibial midshaft of a healthy volunteer.[82] UTE-VTR-based T_1 maps show lower T_1 values and more B_1 spatial modulation than UTE-AFI-VTR-based T_1 maps. Furthermore, the UTE-AFI-VFI method provides fast and accurate T_1 mapping of short-T_2 tissues.[83] T_1 values for long-T_2 tissues, such as cartilage and muscle, obtained with this technique are generally consistent with the literature.[14–16] T_1 values for short-T_2 tissues, such as the menisci, ligaments, tendons, and cortical bone obtained in this way, remain to be validated using a

TABLE I. Summary of short-T_2 imaging contrast mechanisms, including echo subtraction, long-T_2 saturation, off resonance saturation, adiabatic inversion recovery, adiabatic inversion recovery with echo subtraction, dual adiabatic inversion recovery, adiabatic inversion recovery with fat saturation, short TR adiabatic inversion recovery, fat/water imaging, water excitation, and spectroscopic imaging, as well as the technical performance in terms of B_1 inhomogeneity, B_0 inhomogeneity, fat-related chemical shift artifacts, CNR efficiency, SNR efficiency, a summary of the significant advantages and disadvantages, promising and challenging clinical applications, and related references for each technique. OCJ = osteochondral junction.

Short-T_2 imaging contrast mechanisms	Technical Performance (*** best)					Summary of significant advantages and disadvantages		Applications		References
	B_1	B_0	Fat	CNR	SNR	Advantages	Disadvantages	Promising	Challenging	
Echo subtraction	**	*	*	*	***	High SNR, fast acquisition, easy to implement with UTE sequences	Low CNR, sensitive to B_0/susceptibility/off resonance, strong fat signal, difficulty with ZTE/WASPI/SWIFT/PETRA sequences	Most MSK tissues, liver, lung, iron overload, implants	Trabecular bone, myelin	6, 30, 32, 47, and 58
Long-T_2 saturation	*	*	*	*	**	Medium SNR, variety of long-T_2 suppression pulses	Low CNR, sensitive to B_1/B_0/susceptibility/ off resonance, strong residual fat signal	Most MSK tissues	Trabecular bone, myelin	32, 49–51, and 58
Off-resonance saturation	**	**	***	**	*	High CNR, suitable for UTE, ZTE, SWIFT, PETRA	Low SNR, slow acquisition (need two acquisitions with and without saturation)	Most MSK tissues (CEP, OCJ, etc.)	Trabecular bone, myelin	32 and 52–54
Adiabatic Inversion recovery	***	***	*	**	**	High CNR, robust to B_1/B_0 inhomogeneity, good for UTE, ZTE, SWIFT, PETRA	Low SNR, fat signal contamination, slow acquisition, difficulty in suppressing long-T_2 tissues with a broad range of T_1s	Most MSK tissues, iron overload	Trabecular bone, myelin	6, 32, and 55–60
Adiabatic inversion recovery + echo subtraction	***	**	**	***	*	High CNR, robust to B_1 inhomogeneity, magnitude, and complex subtraction	Low SNR, slow acquisition, difficulty in suppressing long-T_2 tissues with a broad range of T_1s	Most MSK tissues, iron overload, Myelin	Trabecular bone	55, 64–66, 68, and 70–73
Dual adiabatic inversion recovery	***	**	**	***	*	High CNR, robust to B_1 inhomogeneity, suppression of long-T_2 water and fat	Sensitive to B_0 inhomogeneity, off resonance, slow acquisition, difficulty in suppressing long-T_2 tissues with a broad range of T_1s	Most MSK tissues, especially the CEP, OCJ, etc.	Trabecular bone	32, 62, and 74–77
Adiabatic inversion recovery + fat saturation	***	**	**	***	*	High CNR, robust to B_1 inhomogeneity, suppression of long-T_2 water and fat	Sensitive to B_0 inhomogeneity, off resonance, slow acquisition, difficulty in suppressing long-T_2 tissues with a broad range of T_1s	Most MSK tissues, especially the CEP, OCJ, etc.	Trabecular bone	61 and 78–80

TABLE I. (*Continued.*)

| Short-T_2 imaging contrast mechanisms	Technical Performance (*** best)					Summary of significant advantages and disadvantages		Applications		References
	B_1	B_0	Fat	CNR	SNR	Advantages	Disadvantages	Promising	Challenging	
Short TR adiabatic inversion recovery	***	***	***	***	*	High CNR, robust to B_1/B_0 inhomogeneity, suppression of water/fat regardless of T_1	Low SNR, slow acquisition, reduced performance when imaging tissues with slightly longer T_2^*s and T_1s (e.g., meniscus, enthesis)	Cortical/trabecular bone, tendon, iron overload, myelin	Meniscus, enthesis	61 and 86–88
Fat/water imaging	**	**	**	*	***	High SNR, reasonable water/fat separation, fast acquisition	No long-T_2 suppression, low CNR for tissues with ultrashort T_2^*, and low PD (e.g., bone, myelin)	Menisci, ligaments, enthesis, tendons	Trabecular bone, myelin	97, 100, and 101
Water excitation	*	*	**	**	***	High SNR, reasonable water/fat separation	No long-T_2 suppression, low CNR for tissues with ultrashort T_2^*, and low PD (e.g., bone, myelin)	Menisci, ligaments, enthesis, tendons	Trabecular bone, myelin	106–108
Spectroscopic imaging	***	***	***	***	*	High CNR, excellent water/fat separation	No long-T_2 suppression, low CNR for tissues with ultrashort T_2^*, and low PD (e.g., bone, myelin)	Menisci, ligaments, enthesis, tendons	Trabecular bone, myelin	110–112
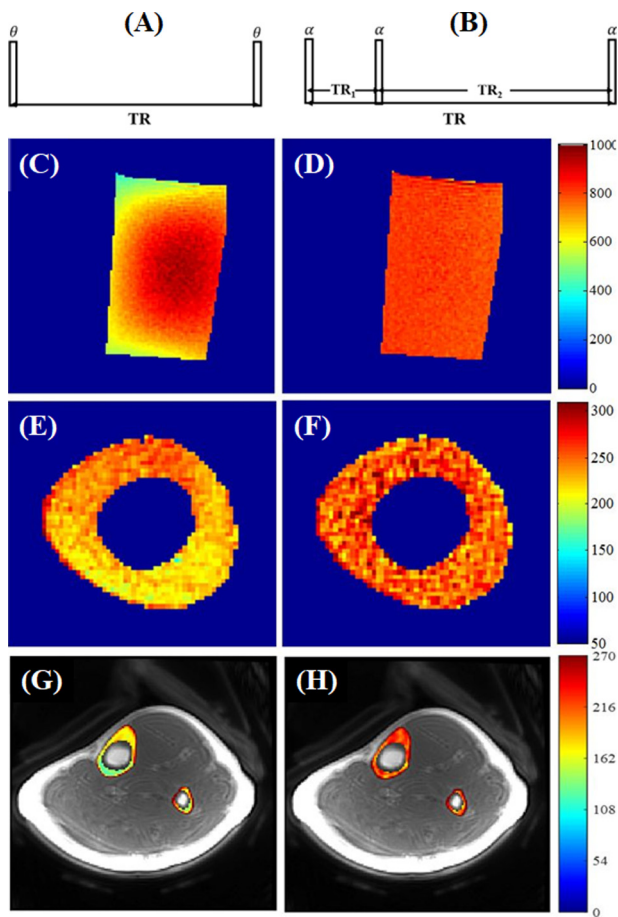
FIG. 16. The T_1 relaxation times of short-T_2 tissues can be measured with the 3D UTE sequence using a variable TR (VTR) method (a) or an actual flip angle imaging (AFI) VTR method (b). UTE-VTR T_1 mapping for a phantom (c), a bovine tibia (e), and the tibia and fibula midshaft of a volunteer (g), as well as UTE-AFI-VTR T_1 mapping for the phantom (d), the bovine tibia (f), and the tibia and fibula midshaft of a volunteer (h), respectively. The UTE-AFI-VTR method provides more homogenous T_1 maps (d), (f), (h), suggesting that it is more consistent than the UTE-VTR method. Reproduced with permission from Ma *et al.*, Magn. Reson. Med. **80**, 598–608 (2018). Copyright 2018 Wiley.[82]

spectrometer where higher RF and stronger gradient systems allow more accurate quantification.

B. UTE T_2^* measurement

Because of their fast signal decay, clinical MRI sequences have difficulty measuring T_2 and T_2^* values of short-T_2 tissues such as bone, ligaments, tendons, and menisci.[130–132] UTE-based T_2^* (UTE-T_2^*) overcomes this limitation and can assess collagen structural integrity and degeneration in articular cartilage, ligaments, and menisci.[130] UTE-T_2^* mapping of meniscus degeneration before the surface breakdown can be an important biomarker of early disease. Figure 17 shows three human meniscus samples assessed by UTE-T_2^*, polarized light microscopy, and alcian blue staining.[133] Samples with no clinical signs of tear or degeneration showed lower UTE-T_2^* values (≤ 8 ms) and

normal histopathological scores (≤ 3) [Fig. 17(a)]. In distinction, samples with grade I–III degeneration on the clinical MRIs showed highly heterogeneous UTE-T_2^* maps and relatively high histopathological scores (≥ 5) [Fig. 17(b)]. Specimens with evidence of tear and/or degenerated signal in the corresponding clinical MRI images of the posterior meniscus showed relatively high mean UTE-T_2^* values (≥ 10 ms) and degenerated histopathological scores (≥ 5) [Fig. 17(c)]. UTE-T_2^* values increased with increasing meniscus injury and decreased with healing.[125] These results suggest that UTE-T_2^* mapping can potentially identify joints at risk of degeneration and facilitate monitoring of therapeutic effects.

Most tissues in the body have multiple water components, which have different T_2 and T_2^* values.[134,135] For example, white matter of the brain has three distinct water components, including myelin water (water trapped in the myelin sheath), axon water (water within myelinated axons), and mixed water (interstitial water).[136] Most musculoskeletal tissues have free water and water bound to the organic matrix. Bound water typically has a short T_2 and is challenging to detect, especially in tissues such as cortical bone and tendons. UTE bi-component analysis facilitates the assessment of bound and free water in short-T_2 tissues.[137–145] Recent studies suggest that short and long T_2^* values and their fractions are significantly correlated with tissue properties.[141,142] Recently, a large-scale prospective study was conducted to investigate the association between UTE bi-component T_2^* analysis and symptoms during exercise therapy for patellar tendinopathy.[145] Among 76 athletes, a significant decrease in T_2^* was found consistent with the presence of degenerative tissue in the patellar tendon (Fig. 18).

C. UTE $T_{1\rho}$ measurement

$T_{1\rho}$ imaging has emerged as a useful noninvasive method for monitoring biochemical changes in various body tissues. It has been employed to probe macromolecules in the liver,[146,147] muscle,[148,149] spine,[150,151] brain,[152–154] and cartilage.[20–22,155] However, because conventional $T_{1\rho}$ imaging sequences cannot evaluate short-T_2 tissues due to the lack of detectable signal,[155,156] UTE-based $T_{1\rho}$ (UTE-$T_{1\rho}$) sequences have been developed to evaluate macromolecular changes (e.g., proteoglycan depletion) in short-T_2 tissues [Fig. 19(a)].[157–160] In this approach, a conventional continuous wave spin-lock pulse is used for magnetization preparation, with the magnetization stored along the z-axis subsequently detected by UTE data acquisition. This technique enables $T_{1\rho}$ imaging of various short-T_2 tissues such as the Achilles tendon, ligaments, menisci, and deep layers of articular cartilage. Figures 19(b)–19(d) show 3D UTE-$T_{1\rho}$ and 2D GRE-$T_{1\rho}$ imaging of the Achilles tendon in a young, healthy volunteer.[159] The GRE-$T_{1\rho}$ sequence provides little signal for the Achilles tendon because of its relatively long TE. In contrast, the 3D UTE-$T_{1\rho}$ sequence shows a much higher signal in the Achilles tendon and demonstrates a short mean $T_{1\rho}$ of 3.07 ± 0.35 ms.

A major limitation with conventional $T_{1\rho}$ imaging is the magic angle effect.[160–162] $T_{1\rho}$ values may be significantly increased when collagen fibers are reoriented from 0° to near 54° (the magic angle) relative to the B_0 field. Trains of adiabatic inversion pulses have been employed to generate a new contrast, termed AdiabT$_{1\rho}$,[163–165] which is less sensitive to the magic angle effect.[166] However, the AdiabT$_{1\rho}$ sequence can only be applied to long-T_2 tissues. To address this limitation, a UTE-based AdiabT$_{1\rho}$ (UTE-AdiabT$_{1\rho}$) sequence has been
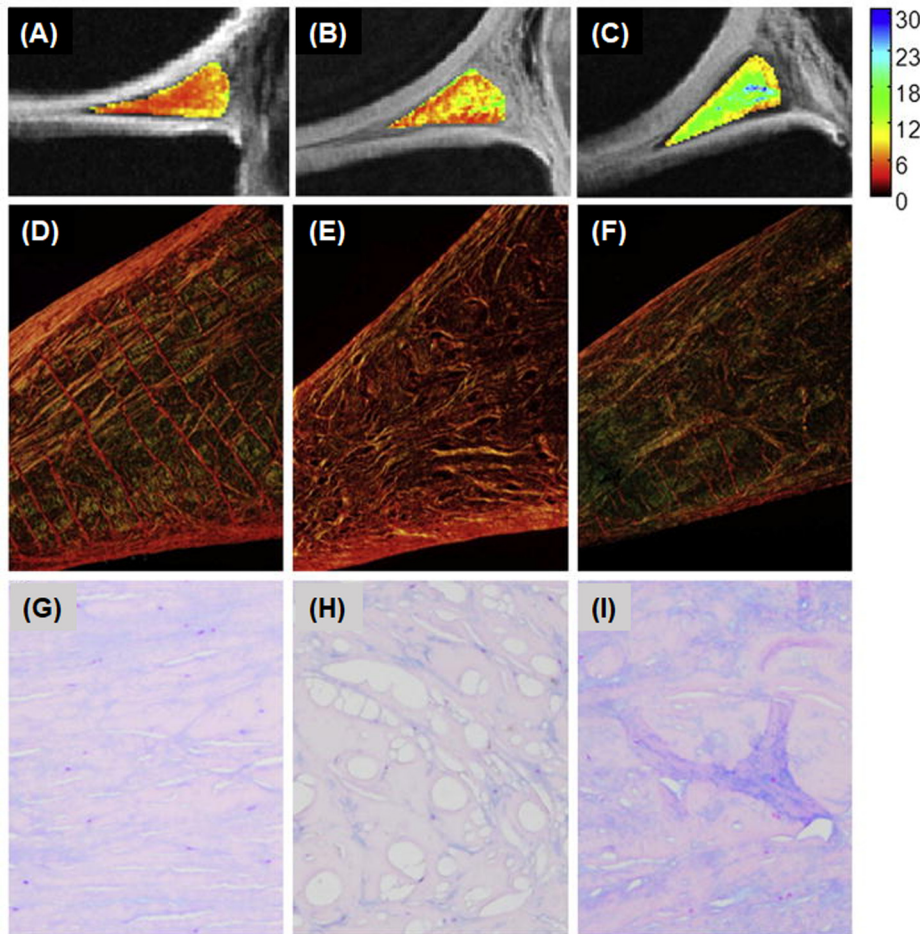
FIG. 17. UTE-T_2^* mapping (a)–(c), polarized light microscopy (d)–(f), and alcian blue staining (g)-(i) of three cadaveric human meniscus samples. The first sample from a 34-year-old female donor is a clinically unremarkable and histologically normal medial meniscus and shows a low mean UTE-T_2^* value [(a), $T_2^* = 7 \pm 2$ ms] with the matrix highly organized, tightly woven, and brightly birefringent on polarized light microscopy with a smooth ground substance [(d) and (g), histology score 0]. The second sample from a 76-year-old male donor is a clinically and histologically degenerate meniscus, and shows a heterogeneous UTE-T_2^* map with a relatively low mean UTE-T_2^* value [(b), $T_2^* = 8 \pm 3$ ms] with grade II degeneration exhibiting cyst formation and disorganized collagen fibers [(e) and (h), score 6]. The third sample from a 75-year-old male donor is a clinically diagnosed grade II degenerate meniscus, and shows an elevated mean UTE-T_2^* value [(c), $T_2^* = 13 \pm 4$ ms] with disorganized, less birefringent collagen and mucoid degeneration [(f), (i), histology score 7]. Reproduced with permission from Williams *et al.*, Osteoarthritis Cartilage **20**, 486–494 (2012). Copyright 2012 Elsevier.[133]
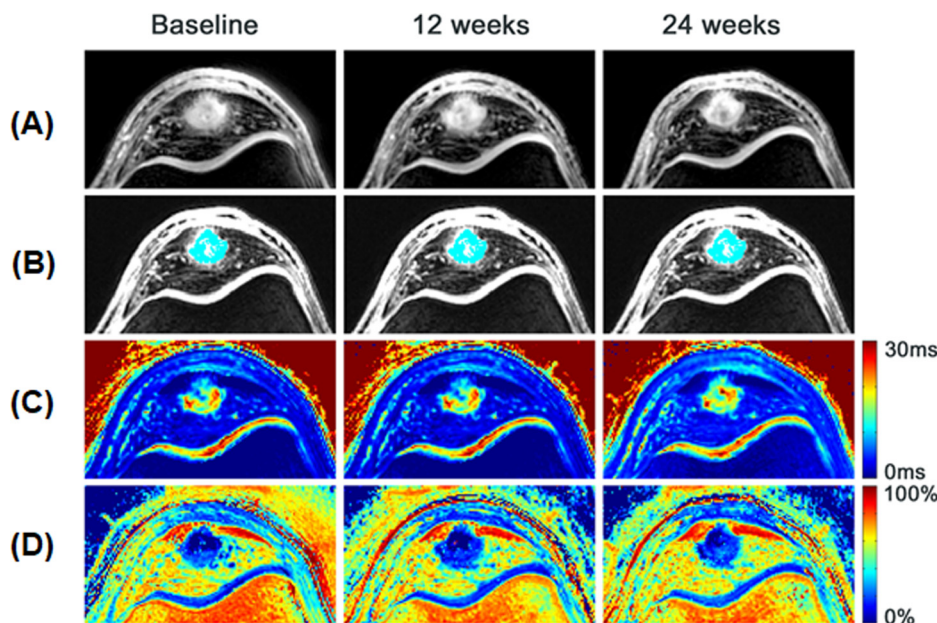
FIG. 18. A 19-year-old male volleyball player with patellar tendinopathy's proximal patellar tendinopathy was subject to 3D UTE imaging at baseline (left column), 12 weeks (middle column), and 24 weeks (right column) (a). UTE T_2^* analysis of automatically selected voxels (cyan) in degenerative tissue in the patellar tendon based on a fitting threshold indicating degeneration of 0%–30% short-T_2^* components (b). The mean UTE T_2^* decreased from 19.9 ± 7.3 ms at baseline to 17.2 ± 5.8 ms at 12 weeks and 16.8 ± 4.9 ms at 24 weeks. Single-component UTE T_2^* maps are on a scale from dark blue (short T_2^*) to red (long T_2^*) (c). Bi-exponential fitting shows the short-T_2^* fraction on a scale from dark blue (0% short-T_2^* components) to red (100% short-T_2^* components) (d). Reproduced with permission from Breda *et al.*, J. Magn. Reson. Imaging **54**, 1596–1605 (2021). Copyright 2021 Author(s), licensed under a Creative Commons Attribution (CC BY) License.[145]

FIG. 19. Diagram of the 3D UTE-$T_{1\rho}$ sequence (a), which employs a composite spin-lock pulse followed by multi-spoke UTE data acquisition. 3D UTE-$T_{1\rho}$ images (b) and 2D GRE-$T_{1\rho}$ images (c) of the Achilles tendon of a 38-year-old healthy volunteer were acquired with four different spin-lock times of 0.02, 1, 5, and 10 ms, respectively. The Achilles tendon 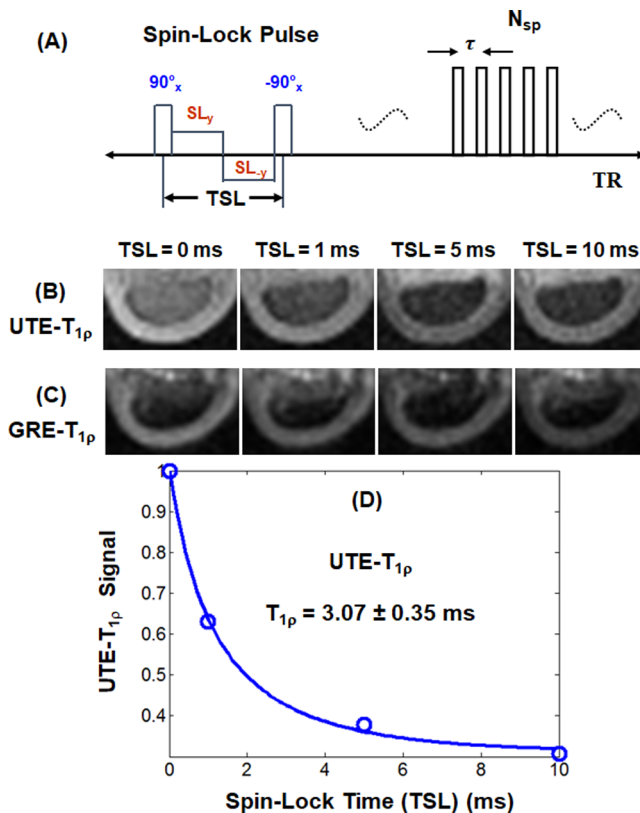shows a signal void with the 2D GRE-$T_{1\rho}$ sequence but a high signal with the 3D UTE-$T_{1\rho}$ sequence. It demonstrates a UTE-$T_{1\rho}$ value of 3.07 ± 0.35 ms using a single-component exponential fitting model (d). Reproduced with permission from Ma et al., NMR Biomed. **30**, 3709 (2017). Copyright 2017 Wiley.[159]

developed to provide robust $T_{1\rho}$ mapping of both short- and long-T_2 tissues on a clinical whole-body scanner.[167–170] The UTE-Adiab$T_{1\rho}$ sequence employs a series of adiabatic inversion pulses followed by 3D UTE data acquisition to generate $T_{1\rho}$ contrast [Fig. 20(a)]. As an example, the knee joint of a young, healthy volunteer was imaged with the 3D UTE-Adiab$T_{1\rho}$ sequence and showed high signal and contrast for all the principal joint tissues [Figs. 20(b)–20(g)].[167] More recent work suggests that the 3D UTE-Adiab$T_{1\rho}$ values show a much reduced magic angle effect compared to both the regular $T_{1\rho}$, UTE-$T_{1\rho}$, and UTE-T_2^* values.[170]

D. UTE proton density measurement

UTE imaging can map the PD of short-T_2 tissues by comparing their MR signal with that of a calibration phantom.[41,86–88] For example, bone water (BW) concentration can be quantified by comparing the UTE signal of bone with that of a water phantom, thereby providing a new metric for assessing bone quality without ionization radiation. In a recent study,[31] bone water concentration was measured in

the tibial midshaft of healthy pre- and postmenopausal women and patients with renal osteodystrophy (ROD). The UTE measurements were compared with bone mineral density (BMD) measured at the same site using peripheral quantitative computed tomography (CT), as well as with BMD of the lumbar spine and hip obtained with dual x-ray absorptiometry. Figure 21 shows cross-sectional images of the tibial midshaft in three representative subjects, as well as scatterplots of bone water and volumetric BMD, obtained from the three groups of women. Patients with renal osteodystrophy had 135% higher bone water content than the premenopausal group ($p < 0.001$) and 43% higher than the postmenopausal group ($p = 0.02$). A much more significant change was observed in bone water than in BMD. Compared with the premenopausal group, cortical thickness was lower by 25% in the postmenopausal group ($p < 0.05$) and by 28% in the renal osteodystrophy group ($p < 0.01$), with no significant difference between these two groups.[31] Manhard et al. developed UTE techniques further to map bound water and pore water in cortical bone and observed excellent correlations between bending strength and bound or pore water concentrations.[127]

E. UTE magnetization transfer imaging

Magnetization transfer (MT) refers to the transfer of spin magnetization from macromolecular protons to water protons. MT imaging allows indirect assessment of macromolecules with restricted motion and extremely short T_2s.[171,172] In this technique, a saturation pulse is placed at a frequency offset Δf away from the water peak to saturate macromolecular protons. These exchange with water protons (either by chemical exchange or magnetization transfer), leading to a significant reduction in the detectable signal. A simple way to quantify the MT effect is to measure the magnetization transfer ratio (MTR) or off resonance saturation ratio (OSR). Clinical MT sequences based on conventional data acquisitions cannot evaluate short-T_2 tissues such as bone. UTE-based MT (UTE-MT) sequences enable direct detection of water signals in short-T_2 tissues and indirect assessment of macromolecular signals (T_2^*s ~ 0.01 ms), which are invisible even with UTE sequences. The MTR in cortical bone was investigated by Springer et al. by combining the 3D UTE data acquisition with a Gaussian-shaped off resonance saturation pulse.[173] Grosse et al. employed OSR to study tendon degeneration.[174] Figure 22 shows ultrasound and MR images of a symptomatic patient with Achilles tendinopathy. The highest overall test performance in distinguishing healthy from pathologically altered tendons was achieved with OSR values at $\Delta f = 750$ Hz. OSR outperforms T_2^* and T_1 relaxation times in differentiating mild and severe tendinopathy from healthy controls. OSR is a clinically useful biomarker for detecting early tendon alterations. In interventional studies, it may help monitor patients with tendinopathic alterations.[174]

More comprehensive quantitative information can be derived through MT modeling, as MTRs or OSRs are only semi-quantitative and show a moderate correlation with tissue properties.[175] The widely used two-pool MT model includes a free pool (water protons) and a semisolid pool (collagen protons).[23,172,176,177] The free pool has a Lorentzian line shape, while the semisolid pool has a Gaussian or super-Lorentzian line shape due to its restricted molecular motion. As MT modeling requires repeated data acquisition with a series of MT powers and frequency offsets, the associated long scan time is a significant challenge for clinical applications. To reduce the total scan time,
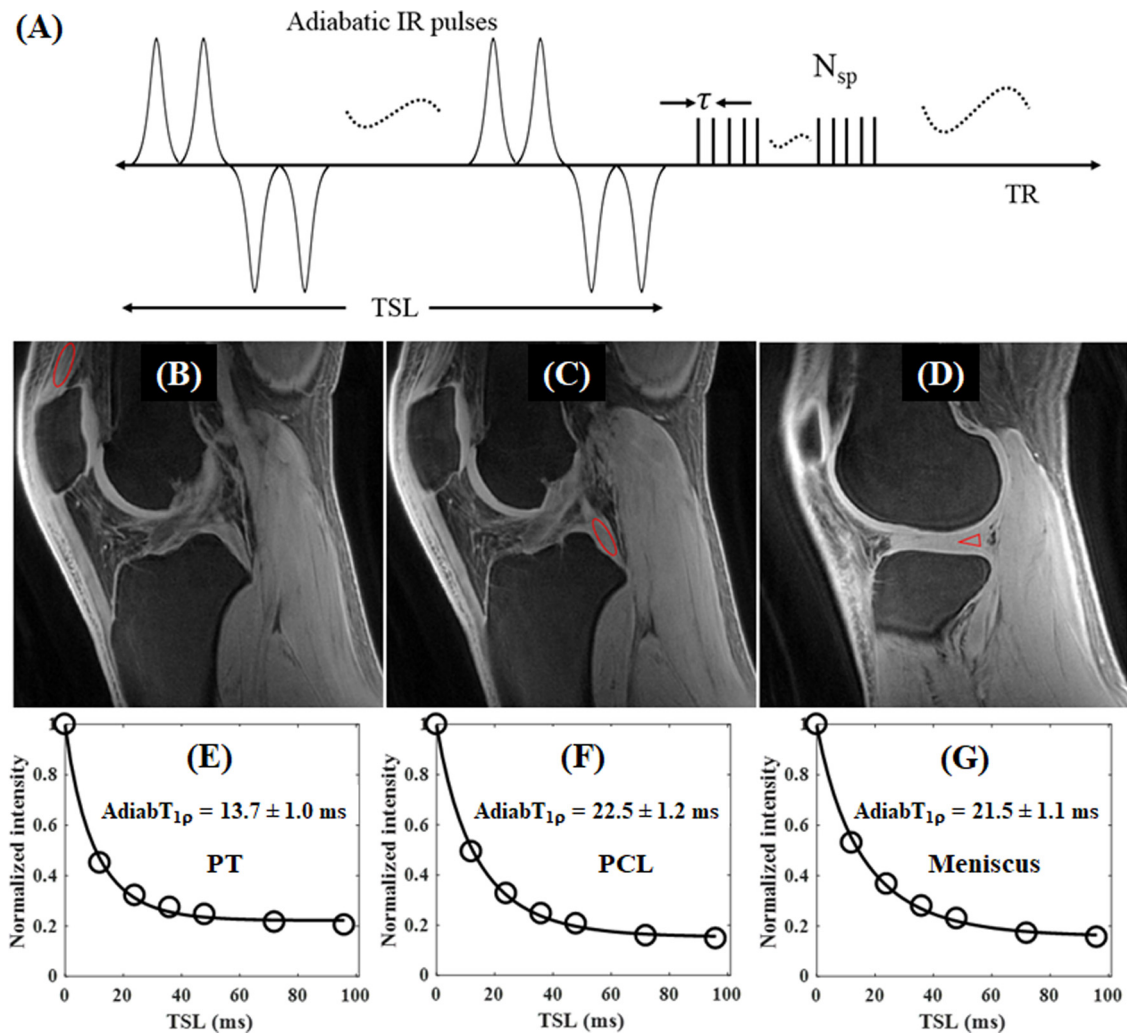
FIG. 20. Diagram of the 3D UTE-AdiabT$_{1\rho}$ sequence (a), which employs a train of adiabatic inversion pulses to generate T$_{1\rho}$ contrast followed by multi-spoke UTE data acquisition. Selected 3D UTE-AdiabT$_{1\rho}$ images of the knee joint of a 23-year-old healthy volunteer with regions of interest (red circles and triangle) drawn in the quadriceps tendon (b), the posterior cruciate ligament (c), and the meniscus (d), as well as the corresponding exponential fittings. These demonstrate UTE-AdiabT$_{1\rho}$ values of 13.7 ± 1.0 ms (e), 22.5 ± 1.2 ms (f), and 21.5 ± 1.1 ms (g), respectively. Reproduced with permission from Ma *et al.*, Magn. Reson. Med. **80**, 1429–1439 (2018). Copyright 2018 Wiley.[167]

multiple spokes (N$_{sp}$) can be acquired after each MT preparation, and a modified rectangular pulse approximation can be used to reduce the associated errors.[176] Figure 23 shows a UTE-MT sequence utilizing these approaches, as well as imaging of a cadaveric human Achilles tendon specimen with three different MT powers (300°, 700°, and 1100°) and five frequency offsets (2, 5, 10, 20, and 50 kHz). The Achilles tendon is invisible with conventional MRI but is visualized with a high signal on all the UTE-MT images [Figs. 23(c)–23(l)]. Relatively smooth maps were generated for MMF, transverse relaxation time T$_{2m}$, and water longitudinal relaxation rate R$_{1w}$, with increased variation observed in exchange rate RM$_{0m}$. MMF was orientation-independent[177] and was highly correlated with tissue biomechanical properties and histologically confirmed degeneration status.[178–181] Recent clinical studies suggest that MMF and MTR are decreased in cartilage and meniscus with mild and advanced osteoarthritis.[182,183]

F. UTE quantitative susceptibility mapping

Magnetic susceptibility is an important material property. Tissues generate local magnetic fields (i.e., dipole fields), which alter the local B$_0$ field. These perturbations of the B$_0$ field can be observed through phase accumulation in GRE sequences using MRI.[26,184–186] The observed static field at a specific spatial location includes contributions from surrounding tissues, which can be modeled as the sum of dipole fields generated by respective magnetic susceptibility sources. This can be approximated by convoluting the dipole kernel with the spatial susceptibility distribution. Quantitative susceptibility mapping
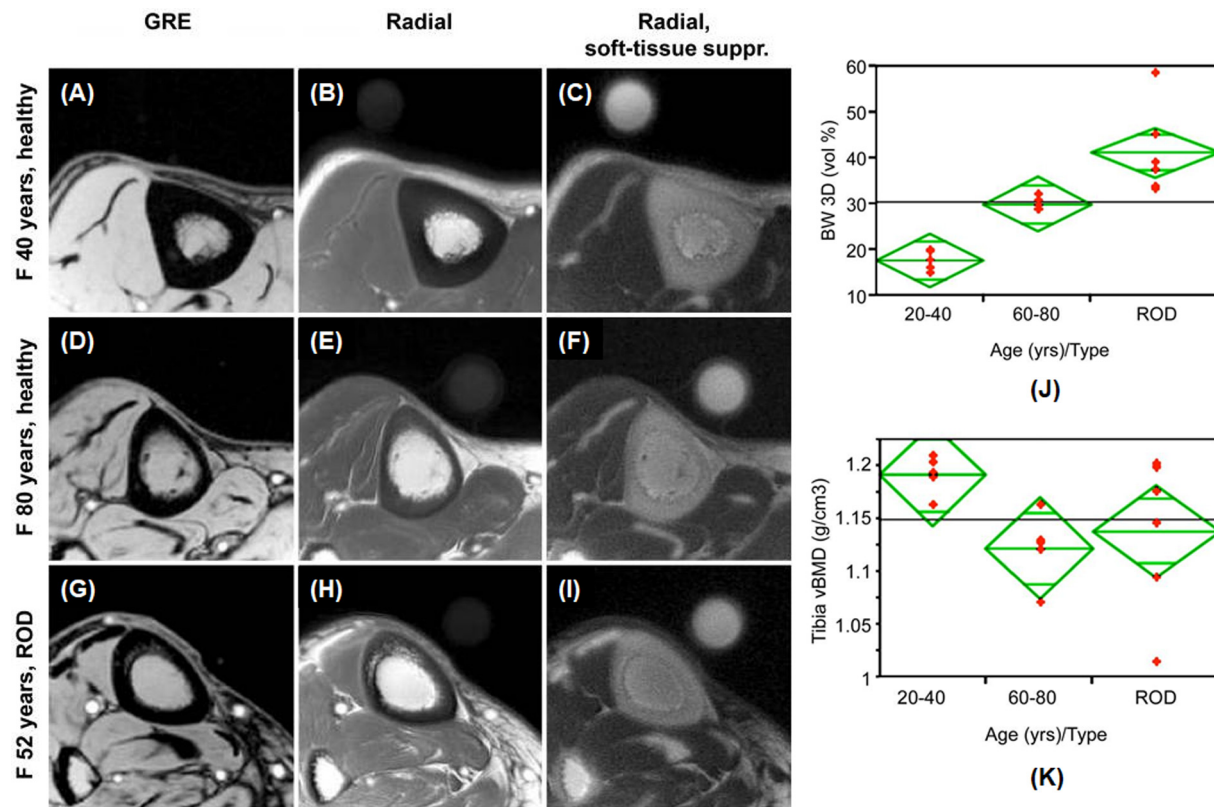
FIG. 21. Axial imaging of the tibial midshaft of a 40-year-old healthy volunteer with clinical GRE (a), radial UTE without (b) and with (c) soft-tissue suppression; that of an 80-year-old post-menopausal volunteer with GRE (d), radial UTE without (e) and with (f) soft-tissue suppression; and that of a 52-year-old patient with renal osteodystrophy (ROD) with GRE (g), radial UTE without (h) and with (i) soft-tissue suppression. Scatterplots show bone water (BW) concentration (j) and volumetric BMD (vBMD) (k) for the younger age group (20–40 year-old), the older age group (60–80 year-old), and the ROD group, respectively. The younger age group has a lower BW concentration and a higher vBMD, and the older age group has a higher BW concentration. The ROD patient group has an abnormally high BW concentration. Reproduced with permission from Techawiboonwong *et al.*, Radiology **248**, 824–833 (2008). Copyright 2008 Radiology Society of North America.[31]

(QSM) solves this ill-posed deconvolution (or dipole inversion) problem by estimating susceptibility from the measured field perturbance using nonlinear optimization techniques.[26] The method has become an important way of assessing iron and calcium content in soft tissues.[26,184] However, the susceptibility of bone and iron overload can be more challenging to measure due to the lack of detectable signal with conventional GRE sequences. UTE-based QSM sequences can accurately detect phase evolution in bone and iron overload.[187–192] The phase changes with increasing TEs can be used to evaluate bone susceptibility using various algorithms such as morphology-enabled dipole inversion.[26] Figure 24 shows a susceptibility map and the corresponding CT slice of a porcine specimen.[187] The close correspondence between diamagnetic regions in QSM and regions of high Hounsfield number on CT images is supported by a strong linear correlation ($R = 0.88$) [Fig. 24(c)]. Several other studies show the value of UTE-QSM for the quantitative assessment of bone mineral and iron overload. A close linear relationship was observed between UTE-QSM susceptibility and iron concentration measurements,[188–190] and excellent agreement was observed between UTE-QSM susceptibility maps and histological iron staining of synovial tissues in a 28-year-old hemophilia patient who subsequently underwent total knee arthropathy.[191]

UTE-QSM was reported to be positively correlated with cortical bone porosity ($R^2 = 0.46$) but negatively correlated with BMD ($R^2 = 0.49$).[192]

G. UTE perfusion

Perfusion plays a vital role in tissue growth and development, disease, and healing. For instance, reduced perfusion is observed in osteoporotic trabecular bone.[193] Decreased osseous vascularity contributes to increased fracture risk,[194] and specifically in vertebral trabecular bone, reduced perfusion occurs in synchrony with reduced BMD.[195] Perfusion also plays a crucial role in the recovery from a meniscus tear, tendon/ligament injury, and many other soft tissue injuries. Dynamic contrast-enhanced MR imaging allows the study of perfusion in various soft tissues. However, it is challenging to study perfusion in short-T_2 tissues such as cortical bone, menisci, ligaments, and tendons which show little or no detectable MR signal with conventional pulse sequences. UTE-based dynamic contrast-enhanced MRI resolves this challenge and can be used to evaluate perfusion in short-T_2 tissues.[196,197] For example, Robson *et al.* applied dynamic UTE MRI to study contrast enhancement in meninges, falx, tendons,
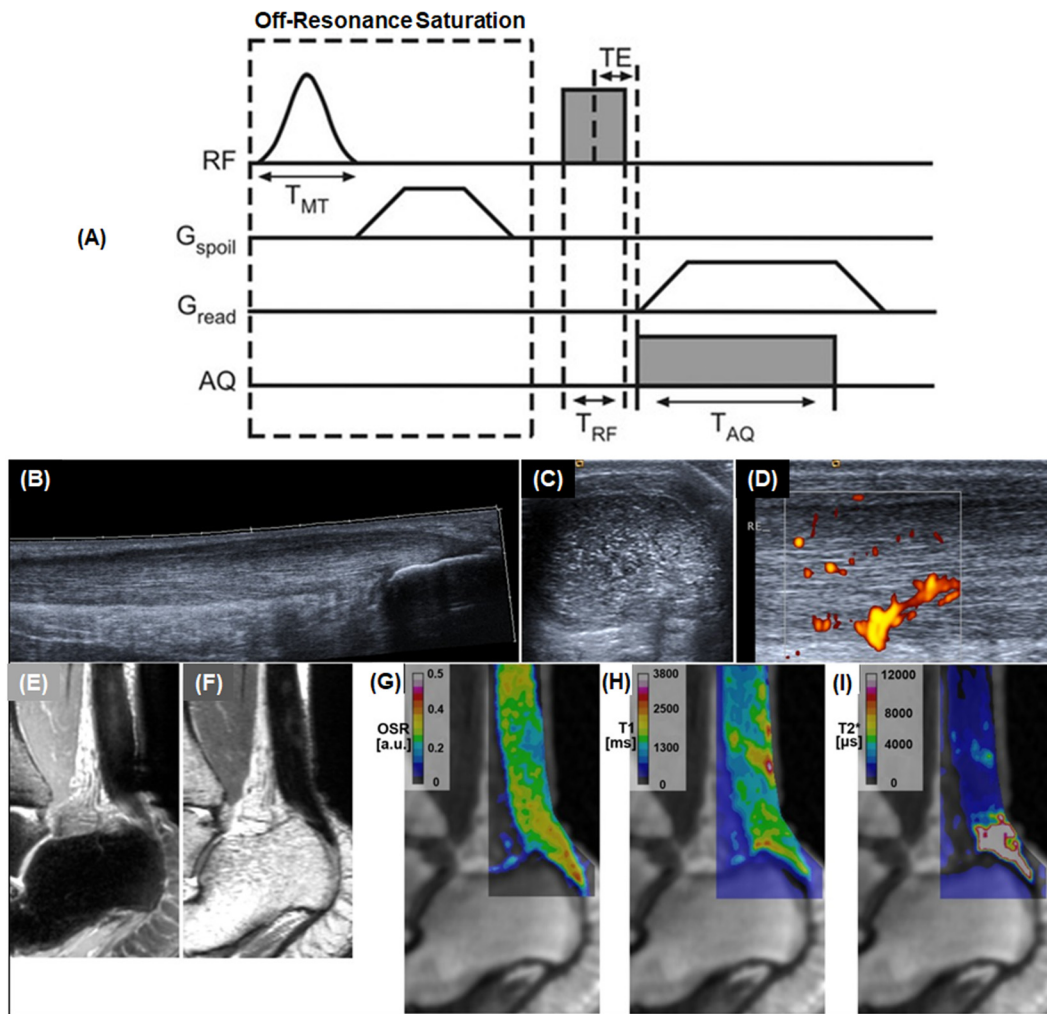
FIG. 22. Diagram of a 3D radial UTE sequence with off resonance saturation (a). Selected images of a symptomatic 45-year-old male patient with a one-year history of recurrent severe posterior heel pain (b)–(i). Panoramic (b), transverse (c), and power Doppler ultrasound image (d); PD-FSE (e) and T_2-FSE (f) images, calculated OSR maps at 2 kHz off resonance (g) as well as T_1 (h) and T_2^* maps (i) which demonstrate pathological tendon alterations over the whole tendon. There is a marked increase in T_2^* values in the tendon near the calcaneus (i), mainly due to the magic angle effect rather than pathological tendon alterations. Reproduced with permission from Grosse *et al.*, J. Magn. Reson. Imaging **41**, 964–973 (2015). Copyright 2015 Wiley.[174]
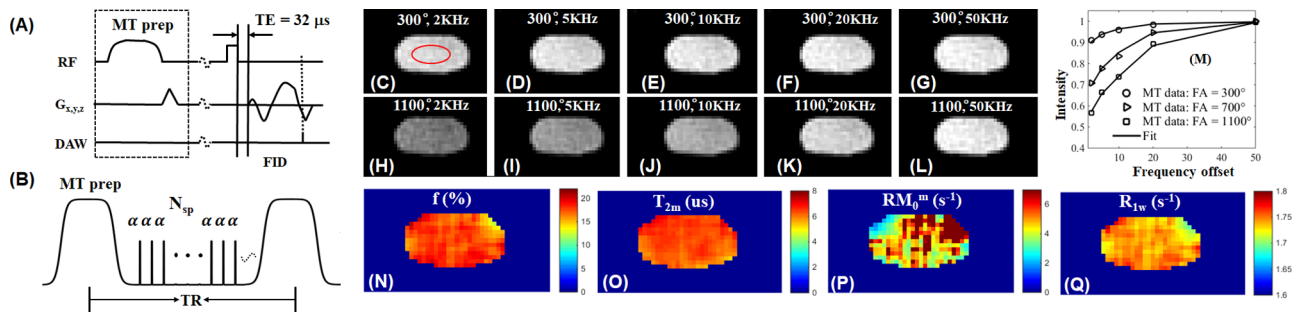
FIG. 23. Diagram of the 3D UTE-MT sequence (a), which employs a Fermi pulse for MT preparation followed by a Cones data acquisition with a minimal TE of 32 μs. Multiple spokes (N_{sp}) are acquired after each MT pulse to accelerate data sampling by a factor of N_{sp} (b). UTE-MT images of an Achilles tendon sample with an MT power of 300° and five frequency offsets of 2 (c), 5 (d), 10 (e), 20 (f), and 50 kHz (g), as well as an MT power of 1100° and five frequency offsets of 2 (h), 5 (i), 10 (j), 20 (k), and 50 kHz (l), are shown. Two-pool modeling (m) allows mapping of macromolecular proton fraction f (n), T_{2m} (o), RM_{0m} (p), and R_{1w} (q). Reproduced with permission from Ma *et al.*, Magn. Reson. Med. **79**, 692–700 (2018). Copyright 2018 Wiley.[176]

FIG. 24. CT (a) and UTE-QSM (b) of a porcine hoof specimen, where UTE-QSM values in ppb and CT values in Hounsfield units (HU) show a high correlation ($R^2 = 0.77$) (c), indicating that UTE-QSM can be used to evaluate bone mineral content. Reproduced with permission from Dimov *et al.*, Magn. Reson. Med. **79**, 121–128 (2018). Copyright 2018 Wiley.[187]

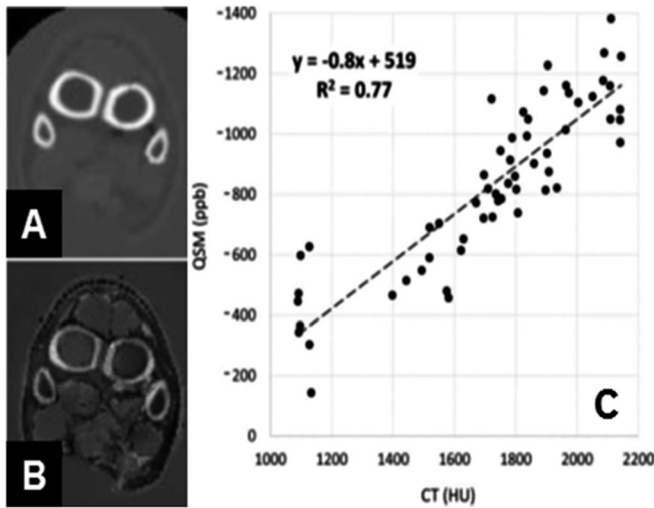reflects the size of the extravascular extracellular space that contrast agents can penetrate. In contrast, K_{ep} and the slope of the enhancement curve reflect the speed of contrast agent entry and washout.[198] Therefore, UTE-based perfusion and pharmacokinetic modeling may increase our understanding of vascularity, metabolism, and related diseases in bone and other short-T_2 tissues, which are otherwise difficult to evaluate with different techniques.

H. UTE diffusion

Double echo steady state (DESS) MRI has been widely used due to its versatility and options for flexible control of T_1, T_2, and diffusion weighting.[198–202] Recently, UTE-based DESS (UTE-DESS) imaging has been introduced.[203,204] This technique is effective for imaging the knee joint and characterizing tissues with short and long T_2s. Free induction decay-like UTE signal (S+) and echo-like signal (S−) are acquired with a pair of balanced readout and read-in gradients for center-out and fly-back data acquisitions which are separated by a trapezoidal spoiling gradient. The fly-back acquisition of S− signal is prone to imaging artifacts such as blurriness and displacement of pixels due to the deviations in trajectory and phase errors in the k-space data caused by eddy currents. It is necessary to compensate for the linear and B_0 eddy current effects by using, for example, a thin-slice excitation approach which requires a one-time phantom calibration.[205] The resultant S+ and S− signals include contributions from the current RF excitation and the stimulated echoes of the preceding RF excitations.[200] Typically, the S− images are more associated with T_2 and diffusion weighting than S+ images are. The T_2 weighting mainly

ligaments, menisci, periosteum, and cortical bone.[196] More recently, Wan *et al.* investigated perfusion in the tibial midshaft of a 38-year-old healthy volunteer. Kinetic analyses demonstrated a mean K^{trans} of $0.23 \pm 0.09 \, \text{min}^{-1}$ and K_{ep} of $0.58 \pm 0.11 \, \text{min}^{-1}$ (Fig. 25).[197] K^{trans}
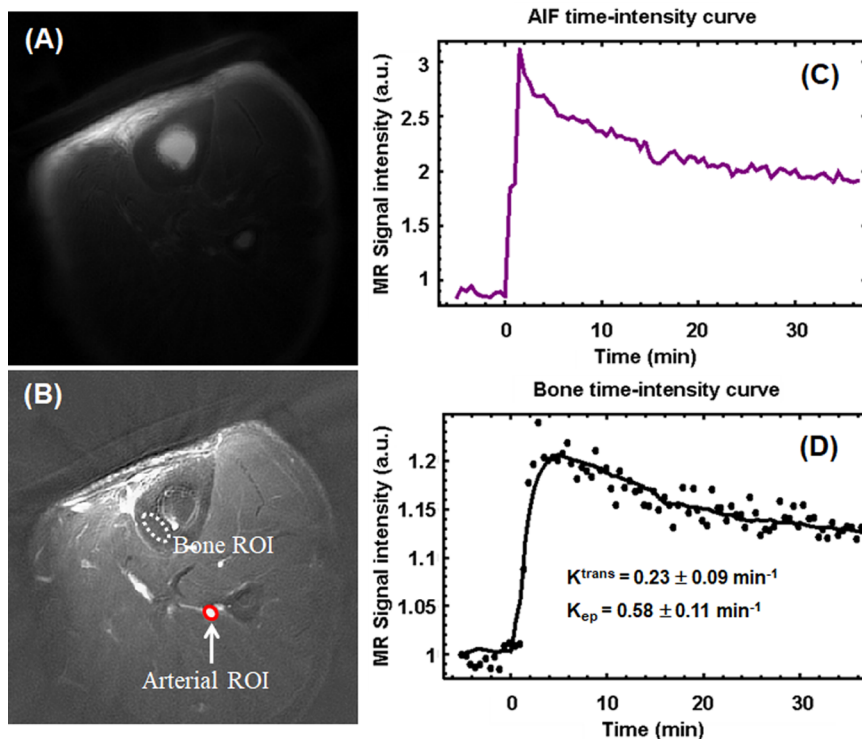
FIG. 25. UTE-based dynamic imaging of the tibial midshaft of a 38-year-old volunteer: baseline image (a), peak-enhancement image minus baseline image (b), contrast enhancement curves for an arterial region of interest (ROI) (c), and a bone ROI (d). Pharmacokinetic modeling demonstrates a K^{trans} of $0.23 \, \text{min}^{-1}$ and a K_{ep} of $0.58 \, \text{min}^{-1}$ for the tibial midshaft of this volunteer (d). Reproduced with permission from Wan *et al.*, Quant. Imaging Med. Surg. **9**, 1383–1393 (2019). Copyright 2018 AME Publishing Company.[197]

occurs during TR, with a longer TR resulting in higher T_2 weighting. The diffusion weighting mainly occurs during TR and is modulated by the flip angle and the gradient moment of the spoiling gradient, which equals $\int G \, d\tau$. Longer TR, lower flip angle, and a larger gradient moment yield higher diffusion weighting. The signal model used for DESS is also applicable to UTE-DESS.[200,204] Four parameters, PD, T_1, T_2, and diffusivity, can be estimated by fitting the S+ and S− signal intensity using this signal model. Figure 26 shows the UTE-DESS sequence and its application in a 52-year-old patient with synovitis and knee osteoarthritis. In long-T_2 tissues such as the synovium, UTE-DESS T_2 and apparent diffusion coefficient (ADC) values match closely with values obtained using conventional techniques. UTE-DESS assessment of diffusion in short-T_2 tissues, such as menisci, ligaments, and tendons, remains to be investigated. Reference ADC values can be derived from tissue samples using a spectrometer with much stronger RF and gradient systems than clinical systems to assess the accuracy of quantification of diffusion in short-T_2 tissues.

I. Other quantitative UTE MRI techniques

Many other techniques have been proposed for quantitatively mapping short-T_2 tissues or tissue components. For example, the organic matrix density in bone can be quantified by comparing its WASPI signal with a calibration phantom.[41] Cartilage T_1 can be mapped with a variable flip angle SWIFT (VFA-SWIFT) approach.[206] VFA-SWIFT allows robust T_1 mapping in deep cartilage and subchondral regions that appear as low or no signal areas with conventional sequences and whose T_1s cannot be reliably quantified. The ZTE sequence cannot be used to measure T_2^* values of short-T_2 tissues based on the traditional variable TE approach because ZTE requires a minimal delay between RF excitation and data acquisition to minimize the loss of the k-space center. To overcome this problem, Wiesinger *et al.* developed a Looping Star pulse sequence where multiple magnetic coherences are excited and gradient-refocused in the form of a looping k-space trajectory to generate FID and multiple gradient echo images for T_2^* mapping.[207] Looping Star imaging can also be used for
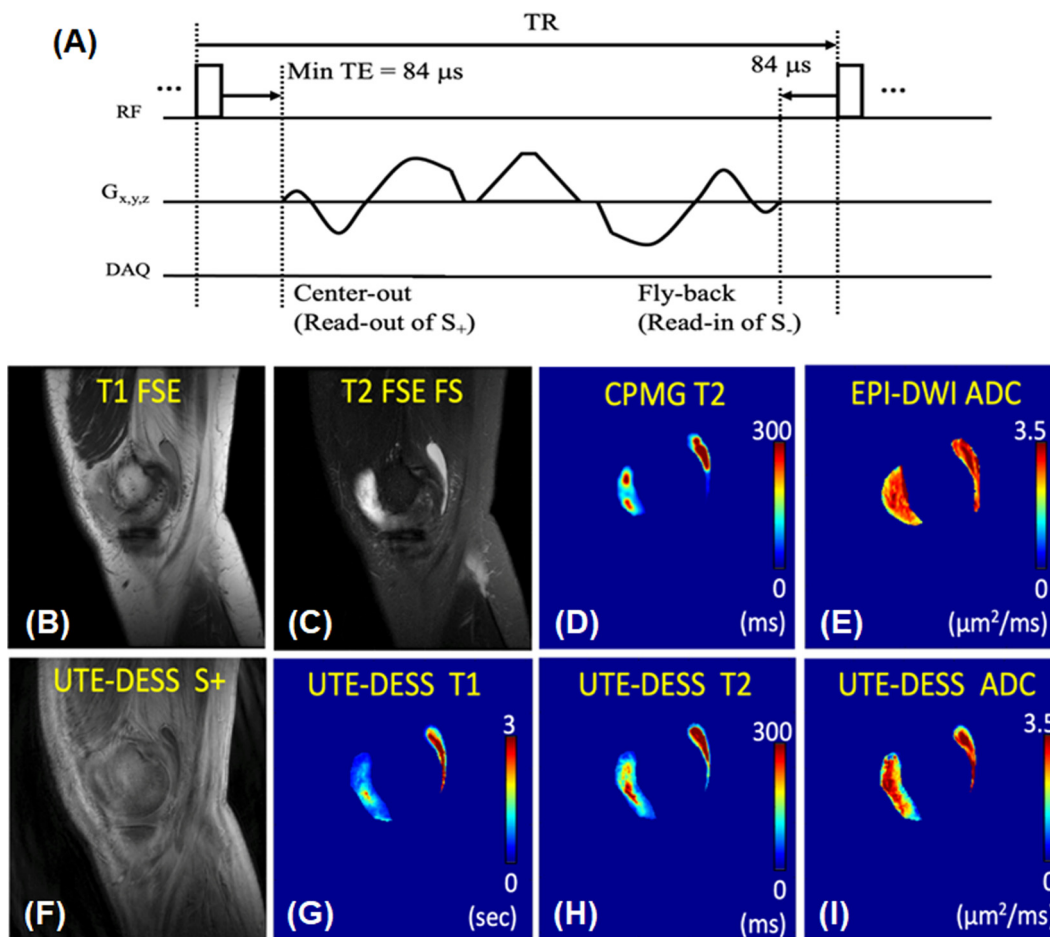
FIG. 26. Diagram of the 3D UTE-DESS sequence (a), which employs balanced center-out spiral readout gradients (S+) and fly-back spiral readout gradients (S−) with a spoiler gradient in-between to spoil the residual transverse magnetization from S+. An example is shown on the knee joint of a 52-year-old female patient with synovitis and osteoarthritis using T_1-FSE (b), T_2-FSE with fat saturation (FS) (c), Carr–Purcell–Meiboom–Gill (CPMG)-T_2 (d), echo planar imaging (EPI)-based DWI ADC (e), UTE-DESS S+ (f), UTE-DESS S− (g), UTE-DESS T_2 (h), and UTE-DESS ADC (i). The UTE-DESS sequence provides T_2 and ADC maps similar to standard CPMG-T_2 and EPI-DWI ADC maps. (a) Reproduced with permission from Jang *et al.*, Magn. Reson. Med. **86**, 881–892 (2021). Copyright 2021 Wiley.[204]

QSM and functional MRI.[207,208] The robustness and quantification accuracy of these techniques remain to be investigated.

J. Summary of quantitative UTE MRI techniques

A variety of quantitative UTE imaging techniques have been developed. These techniques have great potential for improving diagnosis, as summarized in Table II, wherein the targeted tissue component, the major confounding factor (e.g., the magic angle effect), changes with degeneration, and clinical applications for each biomarker are detailed. UTE-based T_2^* mapping allows quantitative evaluation of collagen degradation in short-T_2 tissues such as the menisci, ligaments, and tendons.[130–133,137–145] UTE-based $T_{1\rho}$ allows assessment of proteoglycan depletion in both short- and long-T_2 tissues.[157–160,167–170] UTE-MT imaging, especially signal modeling, enables quantitative mapping of macromolecular fractions and exchange changes in the menisci, ligaments, tendons, and bone.[173–183] UTE-QSM can directly quantify hemosiderin deposition in hemophilic joints and calcium in bone.[187–192] UTE perfusion permits robust separation of the red zone from the white zone in the meniscus, evaluation of bone physiology at the molecular level, and monitoring of bone fracture healing.[196,197] UTE diffusion has the potential for assessment of early disease-stage changes in highly ordered tissues such as the menisci, ligaments, and tendons.[203,204] An important application is the assessment of cartilaginous endplate diffusivity, which is a crucial factor affecting spine disk degeneration.[81] Intervertebral disk degeneration is closely related to a reduction in diffusivity of the cartilaginous endplate.[209] Direct quantitative UTE imaging of the cartilaginous endplate is highly significant in diagnosing disk degeneration and managing back pain.[47,210]

The magic angle effect is a major source of error in quantitative UTE imaging,[158–162] with both T_2 and $T_{1\rho}$ being highly sensitive to it (Fig. 27).[161] The highly ordered collagen fibers in the short-T_2 tissues are subject to strong dipole–dipole interactions, which are modulated by the term $3\cos^2(\theta) - 1$, where θ is the angle between the fiber orientation and the main magnetic field B_0.[211] Previous studies show that $T_{1\rho}$ values can increase more than 200% in the middle and deep zones of articular cartilage and 300% in ligaments when θ is oriented from $0°$ to $54°$.[161] A strong magic angle effect has also been observed in MR neurography with T_2 values enhanced by 37% for the sciatic nerve from 74.5 ± 13.4 ms at $0°$ to 104.0 ± 16.9 ms at $55°$ relative to B_0. The significant $T_{1\rho}$ changes due to the magic angle effect complicate the evaluation of tissue degeneration. Changes in $T_{1\rho}$, T_2 or T_2^* caused by the magic angle effect can be significantly higher than changes caused by degeneration, typically in the range of 10%–30% in osteoarthritis-related changes,[212] posing a problem for accurate clinical diagnosis and treatment monitoring. Magic angle-insensitive techniques, such as UTE-AdiabT$_{1\rho}$[167–170] [Fig. 27(l)] and UTE-MT modeling[176–183] [Fig. 27(n)], are of particular interest for robust assessment of both short- and long-T_2 tissue degeneration.[213]

VI. PART III—APPLICATIONS

Various UTE techniques developed over the last two decades allow direct imaging of short-T_2 tissues throughout the body. The methods have been employed for morphological and quantitative assessment of short-T_2 tissues invisible with conventional clinical MRI sequences. As a result, early changes in short-T_2 tissues can now be evaluated with UTE-type sequences. This is likely to have critical

TABLE II. Summary of quantitative short-T_2 imaging techniques, including UTE-based T_1, T_2, T_2^*, $T_{1\rho}$, adiabatic $T_{1\rho}$, proton density (PD), magnetization transfer ratio (MTR), macromolecular fraction (MMF), quantitative susceptibility (QSM), perfusion, and diffusion, as well as the targeting tissue component, the major confounding factor—the magic angle effect, changes with degeneration, clinical applications, and related references for each biomarker.

Quantitative short-T_2 imaging techniques	Target tissue component	Magic angle effect	Changes with degeneration	Clinical applications	References
UTE-T_1	Water	Minimal	Increase with degeneration/ bone porosity	Osteoporosis, osteoarthritis, liver/ joint iron, lung, etc.	31, 82, 83, and 125
UTE-T_2^*	Collagen	Strong	Increase or decrease with degeneration	Osteoarthritis, hemophilia, liver/joint iron, lung, etc.	130–133 and 137–145
UTE-$T_{1\rho}$	Proteoglycan	Strong	Increase with degeneration	Osteoarthritis, ankle/shoulder/spine degeneration, etc.	157–160
UTE-adiabT$_{1\rho}$	Proteoglycan	Minimal	Increase with degeneration	Osteoarthritis, ankle/shoulder/spine degeneration, etc.	167–170
UTE-PD	Water, Myelin	Minimal	Increase with bone porosity, Decrease in brain lesion	Bound/pore water mapping in bone (osteoporosis) Myelin mapping (multiple sclerosis, Alzheimer's disease, etc.)	31, 41, 58, 64, 86–88, 117, and 127
UTE-MTR	Collagen	Medium	Decrease with degeneration/bone porosity	Osteoporosis, osteoarthritis, ankle/shoulder/ spine degeneration	173–175 and 178
UTE-MMF	Collagen	Minimal	Decrease with degeneration	Osteoporosis, osteoarthritis, ankle/shoulder/ spine degeneration	176, 177, 179–183
UTE-QSM	Iron, calcium	Minimal	Increase with iron/calcium deposition	Osteoporosis, liver/joint iron, Parkinson's disease, etc.	187–192
UTE-perfusion	Blood	Minimal	Increase with degeneration/fracture	Bone/tendons/ligaments fracture, meniscal tear, etc.	196 and 197
UTE-diffusion	Collagen	Minimal	Increase with degeneration	Menisci/ligaments/tendons degeneration, etc.	203 and 204
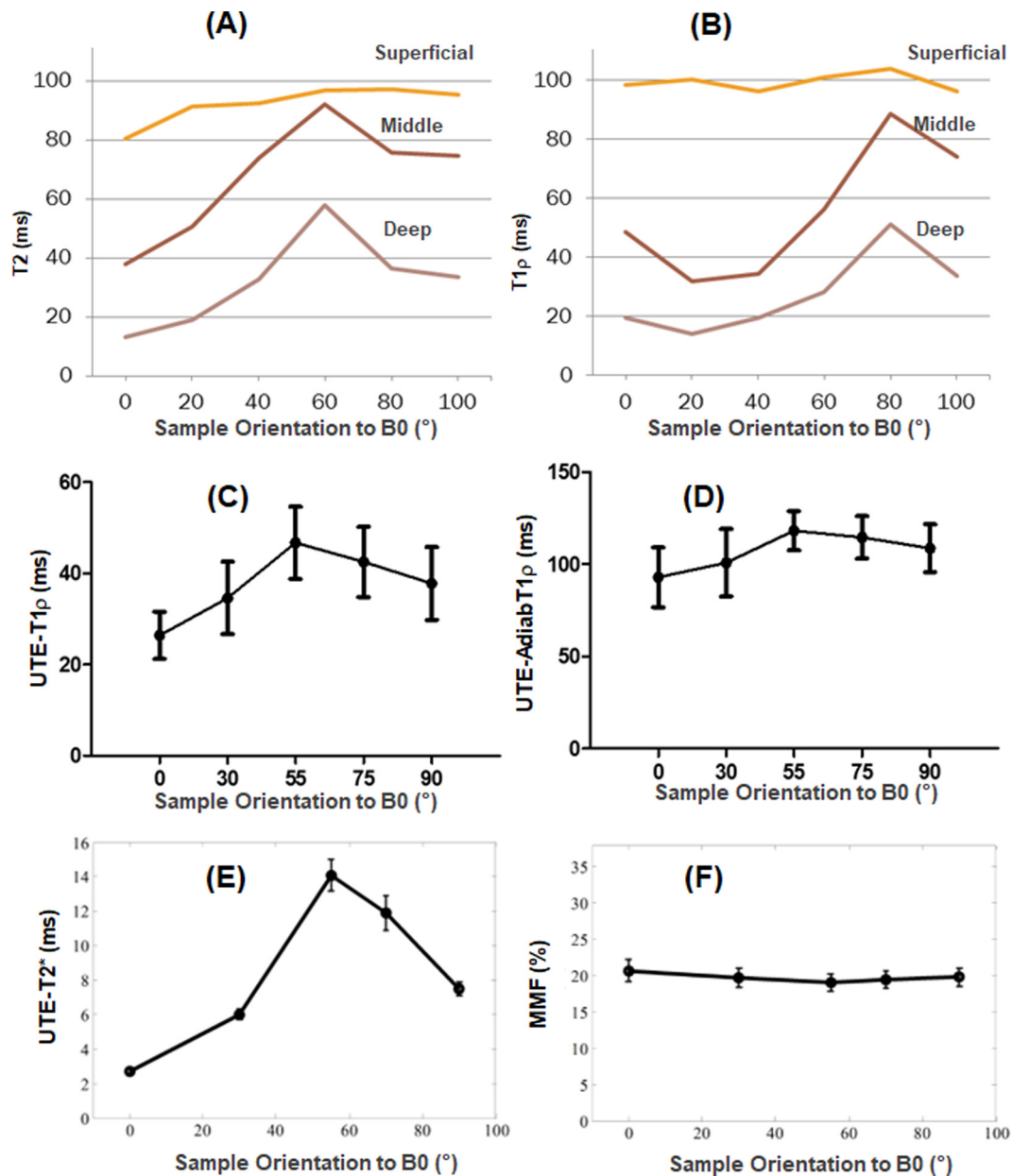
FIG. 27. The angular dependence of T_2 (a) and $T_{1\rho}$ (b) for the superficial, middle, and deep layers of articular cartilage. Both T_2 and $T_{1\rho}$ show strong magic angle effects in the middle and deep layers, where the collagen fibers are highly organized. UTE-$T_{1\rho}$ shows a similar magic angle effect (c), while UTE-Adiab$T_{1\rho}$ shows a much reduced angular dependence (d). The Achilles tendon shows a strong angular dependence in UTE-T_2^* (e) but almost no angular dependence in MMF derived from two-pool UTE-MT modeling (f). (a) and (b) Reproduced with permission from Shao et al., Osteoarthritis Cartilage **25**, 2022–2030 (2017). Copyright 2017 Elsevier.[161] (c) and (d) Reproduced with permission from Wu et al., Magn. Reson. Med. **84**, 2551–2560 (2020). Copyright 2020 Wiley.[170] (e) and (f) Reproduced with permission from Ma et al., NMR Biomed. **29**, 1546–1552 (2016). Copyright 2016 Wiley.[177]

applications in the musculoskeletal, nervous, respiratory, gastrointestinal, and cardiovascular systems, as summarized below.

A. UTE MRI in the musculoskeletal system

The musculoskeletal system has many connective tissues with short or ultrashort T_2/T_2^* relaxation times, such as the osteochondral junction, menisci, ligaments, tendons, and bone. These are primarily invisible with conventional clinical MRI sequences.[213] The ability to directly capture signals from these short-T_2 tissues or tissue components can significantly change how musculoskeletal diseases such as osteoarthritis and osteoporosis are diagnosed.

Osteoarthritis is historically considered a cartilage disease; however, cartilage damage may not necessarily result in osteoarthritis.[214]

There is a shift in the understanding of osteoarthritis from a cartilage disease to a "whole joint organ" disease.[215] Damage to the medial and lateral menisci, anterior cruciate, posterior cruciate, collateral ligaments, quadriceps and popliteus tendons, subchondral bone–cartilage interface, and subchondral bone all influence the initiation and progression of cartilage damage.[216,217] Any joint tissue deterioration is likely to have a negative impact on cartilage integrity, thereby leading to failure of the joint as a whole.[218–224] For instance, the meniscus functions not only as a facilitator of load distribution and shock absorption[221] but also plays a crucial role in proprioception,[222–224] an essential aspect of its protective function. Hunter et al. studied the connection between meniscal pathologic changes and loss of cartilage in symptomatic knee osteoarthritis and reported a strong correlation between meniscal position/damage and cartilage loss.[218] Each aspect of meniscal abnormality (either damage or a change in position) significantly affected the risk of cartilage loss. Structural changes in the collateral ligaments and tendons of the interphalangeal joints may precede morphological changes in cartilage and eventually contribute to subsequent cartilage degeneration.[219] Therefore, quantifying both short- and long-T_2 tissues of the joint using UTE-type sequences is likely to be more effective in detecting alterations in the early stages of osteoarthritis than conventional clinical sequences alone, which only assess long-T_2 tissues.[179–183,225] UTE imaging can also be used to track superparamagnetic iron oxide nanoparticles labeled multipotent mesenchymal stem/stromal cells injected into joints containing osteochondral defects, thereby providing a method for monitoring the treatment of osteoarthritis.[226]

Osteoporosis leads to increased bone fragility and fracture risk due to low bone mass and microarchitectural deterioration of bone. Bone consists of mineral, organic matrix, and water with a volume fraction of ∼43%, ∼35%, and ∼22%, respectively,[227–229] with the three bone components ordered in a complex hierarchical structure.[230] Stiffness and strength are determined by bone minerals,[231] whereas ductility and the ability to absorb energy before fracturing are determined by collagen.[232] Viscoelasticity and poroelasticity are determined by bone water.[233] Over the last several decades, the contributions of organic matrix and water to bone quality have largely been neglected, with bone minerals drawing the focus of scientific thinking.[234] The diagnostic gold standard in clinical practice is x-ray-based BMD measurement. However, ∼60% of bone by volume is composed of the organic matrix and water, which make significant contributions to the mechanical properties of bone but cannot be evaluated with x-ray-based techniques. As a result, BMD alone predicts fractures poorly, with an accuracy of only 30%–50%.[235–237] Methods capable of simultaneous assessment of organic matrix, water, and mineral are needed for a more comprehensive evaluation of bone quantity and quality.

UTE MRI techniques can potentially evaluate all three major components in bone: water, organic matrix, and mineral.[238–246] Total water proton density (TWPD) and bound water proton density (BWPD) can be measured with UTE and IR-UTE sequences, respectively, with pore water proton density (PWPD) estimated by subtracting BWPD from TWPD.[58] Bone MMF can be measured with UTE-MT imaging and two-pool signal modeling,[176] and macromolecular proton density (MMPD) can be estimated as a function of MMF and TWPD. Several bone sample studies have demonstrated that TWPD, PWPD, and MMF are significantly correlated with bone porosity, BMD, and mechanical properties.[90–92,240–242] Higher TWPD and PWPD values but lower BWPD, MMF, and MMPD values were observed in older human subjects compared to young subjects.[242] Figure 28 shows various proton density maps generated from a 34-year-old female volunteer and a 75-year-old female volunteer.[242] PWPD was generally higher in older subjects than in younger subjects, but BWPD and MMPD were lower in older subjects.

Bound water and pore water contribute differently to the mechanical properties of bone, with bound water correlated with bone strength and toughness, and pore water inversely correlated with the modulus of elasticity.[243] There are other bone imaging biomarkers, such as the porosity index, which is defined as the ratio of signal intensities between a long TE and the shortest TE obtained by the UTE imaging,[125,244] and the suppression ratio, which is defined as the ratio
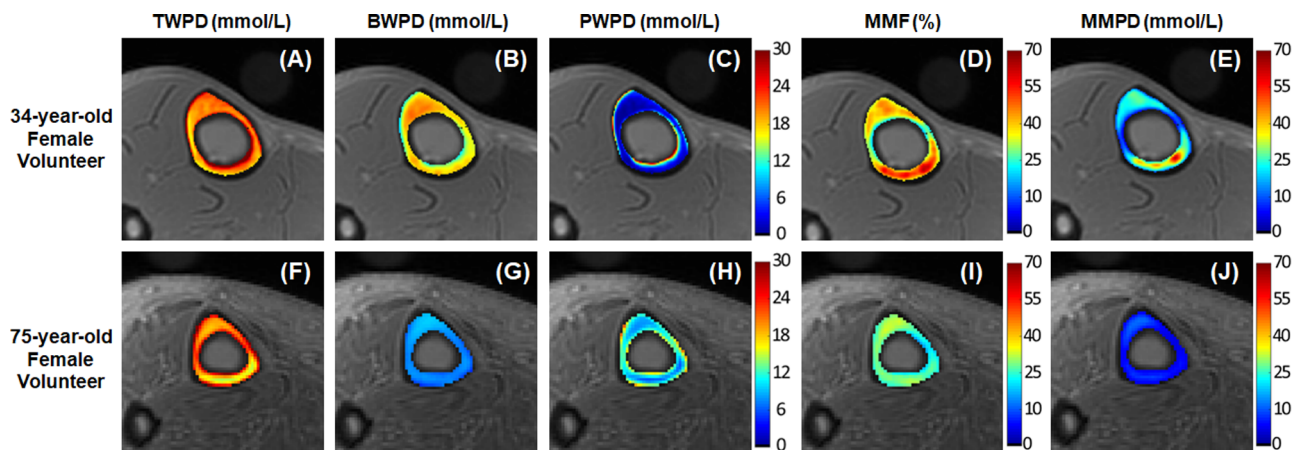
FIG. 28. The tibial midshaft of a 34-year-old female volunteer was subject to total water proton density (TWPD) mapping from PD-weighted UTE imaging (a), bound water PD (BWPD) mapping from IR-UTE imaging (b), pore water PD (PWPD) mapping from the subtraction of TWPD from BWPD (c), macromolecular fraction (MMF) mapping from UTE-MT modeing (d), and macromolecular PD (MMPD) mapping from TWPD combined with MMF (e). Also shown are maps of TWPD (f), BWPD (g), PWPD (h), MMF (i), and MMPD (j) of the tibial midshaft of a 75-year-old female volunteer. The older volunteer has higher PWPD, but lower BWPD and MMPD than the younger volunteer. Reproduced with permission from Jerban et al., Bone **127**, 120–128 (2019). Copyright 2019 Elsevier.[242]

between bone UTE signal without long-T_2 suppression and with long-T_2 suppression.[245] The porosity index is significantly correlated with μCT-based porosity, mechanical stiffness, age, and collagen estimation from near-infrared spectroscopy.[244] In contrast, the suppression ratio correlates significantly with bone porosity and age.[125] These UTE-based biomarkers will likely have significant advantages over the current gold standard BMD. One example concerns raloxifene, a Food and Drug Administration (FDA)-approved agent that is designed to treat bone loss, decrease fracture risk, and improve bone mechanical properties. Notably, these benefits are essentially independent of bone mass changes and are mediated by an increase in matrix-bound water as measured by UTE MRI.[246] The hydroxyl groups on raloxifene provide a possible explanation for the therapeutic effect of raloxifene. It is important to identify a cell-independent mechanism that can be utilized for novel pharmacological approaches to enhancing bone strength.[246]

Morphological and quantitative UTE imaging of short-T_2 tissues also has applications in other musculoskeletal diseases such as spine degeneration,[79–81] rotator cuff disorders,[179,247] tendinopathy,[144,145,248,249] psoriatic arthropathy,[250] hemophilia arthropathy,[191] and temporomandibular disorders.[251–253] Direct imaging of short-T_2 tissues may have a significant impact on the diagnosis and therapeutic management of such diseases.

B. UTE MRI in the nervous system

Myelin integrity is crucial for the normal function of the nervous system.[254–269] Myelin is a lipid-rich, multilaminar sheath, which is wrapped around axons and facilitates fast propagation of action potentials in axons. Normal cognitive function and behavior are highly dependent on the presence of myelin, which can increase action potential transmission speed by ~100-fold and decrease refractory time by ~30-fold. Those factors together increase brain "connectivity" or the brain's information processing capacity by ~3000-fold, making myelin indispensable for the development and maintenance of elaborate cognitive functions.[254–256] The speed at which neuron signals are transmitted is directly related to the thickness of the myelin wrapping and neuronal myelin content, and generation of oligodendrocytes and myelin is required for learning complex motor skills.[257–263] Myelin impairment can disrupt axonal transport, integrity, and plasticity, leading to a massive reduction in signal transduction.[264–266] Given its essential role in the development and maintenance of elaborate cognitive functions, myelin plays a crucial role in the pathogenesis of many neurological diseases such as multiple sclerosis,[267] Alzheimer's disease,[268] Parkinson's disease,[269] epilepsy,[270] and traumatic brain injury.[271]

It is of central importance to develop advanced MRI techniques to measure myelin content and its MR properties. However, conventional MRI techniques have TEs that are too long to detect signals from the non-aqueous protons in myelin which have extremely short T_2s ($\ll 1$ ms).[272] As a result, conventional MRI focuses on long-T_2 water components (CSF, intracellular water, extracellular water, and myelin water). This approach provides high-resolution images of gray and white matter structures and volumes but not of short-T_2 components. It is, therefore, highly desirable to develop novel MRI techniques that can detect myelin signals and reliably quantify myelin content and MR relaxation times. Over the past two decades, most researchers in this field have focused on myelin water (via multi-component T_2 or

T_2^* analysis),[273–275] magnetization transfer,[276] or diffusion[277] to indirectly assess myelin with suboptimal results. For example, most conventional MRI-based techniques cannot distinguish the several cardinal pathological substrates of multiple sclerosis, namely, demyelination, remyelination, inflammation, edema, axonal loss, and gliosis.[278–281] Furthermore, these indirect imaging techniques cannot quantify myelin properties such as its T_1 and T_2^*.

Direct assessment of the integrity of myelin may be of value for diagnosing and assessing prognosis in many neurological diseases, including multiple sclerosis.[55,63–73,116–118] UTE-type sequences with TEs < 0.1 ms allow direct imaging of myelin.[63–73] The main challenge to this approach is selectivity because long-T_2 water components show far higher signals than myelin.[71] Adiabatic inversion pulses can uniformly invert and suppress the longitudinal magnetizations of various water components, making it possible to selectively image myelin with the IR-UTE sequences.[55,57] Figures 29(a)–29(d) show representative clinical and IR-UTE brain images from a 28-year-old female donor with confirmed multiple sclerosis.[67] Areas of normal appearing white matter show a high signal on the IR-UTE echo subtraction image, while areas of abnormality appear with a low signal. Some lesions on the IR-UTE images correspond to T_2 hyperintense areas of abnormality on conventional T_2-weighted images and hypointense areas on T_2-weighted fluid-attenuated inversion recovery (T_2-FLAIR) images. However, the abnormalities seen on the IR-UTE images extend into adjacent areas that are seen as normal appearing white matter on conventional images, demonstrating how the IR-UTE sequence show areas of abnormality that are invisible on conventional T_2-weighted and T_2-FLAIR images. Figures 29(e)–(h) show results from a 69-year-old female patient with multiple sclerosis. Clinical magnetization-prepared rapid gradient echo (MP-RAGE) and T_2-FLAIR images are shown for comparison.[87] Lesions detected with these two clinical sequences show a signal loss on the STAIR-UTE images. In a feasibility study of four healthy volunteers (21–47 years of age, three males, one female) and four patients with multiple sclerosis (49–69 years of age, four females), lesions in patients showed a lower mean myelin proton fraction value of $5.7 \pm 0.7\%$ compared with the value of $8.9 \pm 0.6\%$ in normal white matter (NWM) of healthy volunteers.[87] The difference was statistically significant ($p < 0.0001$). Normal gray matter (NGM) had a myelin proton fraction value of $5.9 \pm 0.3\%$. These results suggest that STAIR-UTE-measured myelin proton fraction may be a valuable biomarker for multiple sclerosis diagnosis and therapeutic monitoring.

Several other UTE-based techniques have been developed for imaging myelin *in vivo*. Long-T_2 saturated 2D UTE imaging can detect myelin loss in patients with multiple sclerosis.[50] UTE-MT has been proposed for myelin imaging and quantification, with UTE-based MTRs showing a strong correlation ($R^2 = 0.71$) with percent coverage of myelin basic protein immunostaining.[282] More recently, a novel hybrid filling technique has been developed to directly image myelin with improved scan efficiency using ZTE imaging with significant dead time gaps.[118] However, T_1 variations in different regions of the human brain may lead to imperfect suppression of signals from long-T_2 white matter and gray matter. A novel technique called dual-echo sliding inversion recovery UTE imaging has been developed to provide robust signal suppression from various water components regardless of their T_1 values.[283] This technique potentially allows more accurate whole-brain myelin mapping. Direct morphological and quantitative
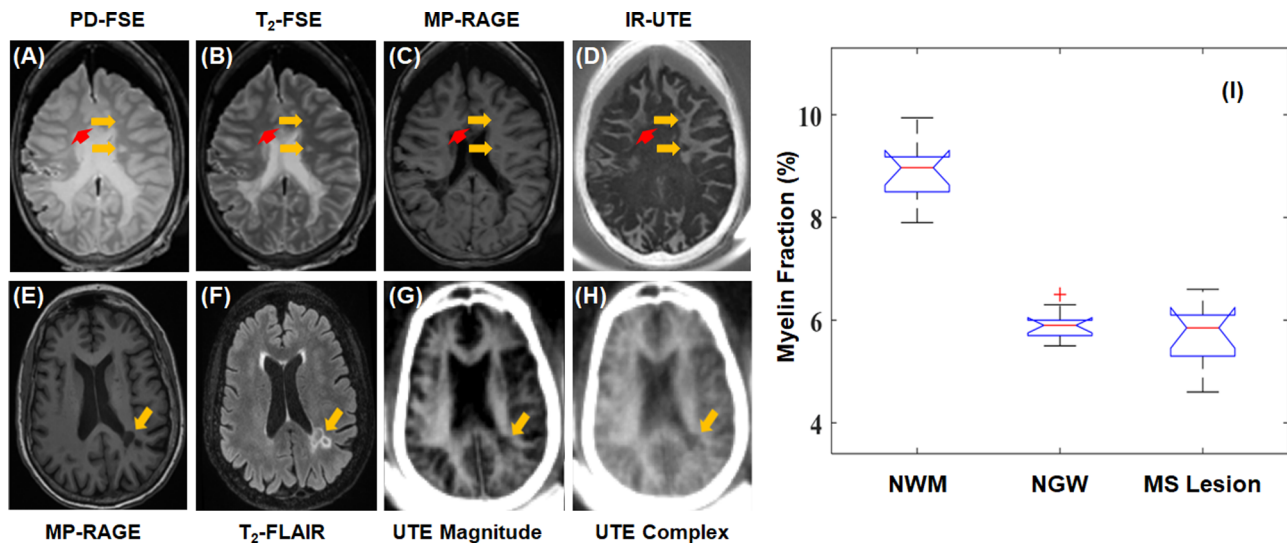
FIG. 29. A brain specimen from a 28-year-old female donor with confirmed multiple sclerosis (MS) was imaged with clinical PD-FSE (a), T_2-FSE (b), and MP-RAGE sequences (c), as well as the IR-UTE sequence (d). Lesions (yellow arrows) are hyperintense on PD-FSE and T_2-FSE images but hypointense on MP-RAGE and IR-UTE images. Partial myelin loss can only be detected with the IR-UTE sequence [red arrowhead in panel (d)] and appear normal [red arrowheads in panels (a)–(c)] with the PD-FSE, T_2-FSE, and MP-RAGE sequences. A 69-year-old female MS patient was imaged with MP-RAGE (e) and T_2-FLAIR sequences (f), as well as the STAIR-UTE sequence with magnitude subtraction (g) and complex subtraction (h) with obvious myelin loss indicated by yellow arrows. MS lesions in four patients showed a lower mean myelin fraction of $5.7 \pm 0.7\%$ compared with $8.9 \pm 0.6\%$ for normal white matter (NWM) and $5.9 \pm 0.3\%$ for normal gray matter (NGM) in four healthy volunteers. (a)–(d) Reproduced with permission from Sheth *et al.*, NeuroImage **136**, 37–44 (2016). Copyright 2016 Elsevier.[67] (e)–(i) Reproduced with permission from Ma *et al.*, J. Magn. Reson. **323**, 106898 (2021). Copyright 2021 Elsevier.[87]

imaging of myelin with 3D UTE-type sequences, rather than indirect imaging of myelin or long-T_2 water components with conventional MRI sequences, is likely to improve the diagnosis and monitoring of the effectiveness of treatment in many neurological diseases.

C. UTE MRI in the respiratory and gastrointestinal systems

A short TE is necessary for direct imaging of organs such as the lung[284–291] and organs such as the liver that can incur high iron overload.[292–294] The lung parenchyma is poorly visualized with conventional MRI due to its low PD and short T_2^* resulting from the air and soft-tissue interfaces within the lung. While the liver is typically visible, hemochromatosis or iron overload may significantly reduce its T_2^*, thus rendering it invisible. UTE-type sequences have been employed to resolve this challenge. However, using a short TE alone is frequently insufficient to provide robust imaging of the lung and liver, which are both subject to respiratory motion.

Respiratory motion-compensation (MoCo) strategies based on motion tracking for retrospective motion correction or compensation have been developed.[287–290] The motion can be indirectly tracked by measuring the respiratory-induced abdominal movement using external respiratory belts. MoCo reconstruction resolves motion by aligning all motion state images to the same state via image-based registration. A new free-breathing motion-corrected pulmonary MRI strategy, iterative MoCo reconstruction UTE (iMoCo UTE), has been developed for high-resolution lung MRI.[290] The technique employs a pseudo-random UTE sequence with motion-resolved reconstruction and motion estimation and a novel iMoCo reconstruction with

compressed sensing. The reconstruction algorithm iteratively fits the data to a nonrigid motion model and uses compressed sensing principles to suppress noise and artifacts. Figure 30 shows volumetric UTE imaging of a non-sedated 10-week-old infant with pulmonary interstitial glycogenosis, with an isotropic resolution of 0.9 mm and a total scan time of 5 min.[290] Vessel structures (red arrow) and airways (green arrows) are depicted much better with iMoCo reconstruction. The bulk motion of the infant was captured with an image-based navigator, whereby any data corrupted by bulk motion was rejected [Fig. 30(b)]. Bulk motion rejection improves the sharpness of both the vessels and diaphragm (red arrows) [Fig. 30(c)].

Several other UTE techniques have been developed for lung imaging. Ohno *et al.* compared UTE MRI with multidetector CT for pulmonary function assessment and clinical stage classification of chronic obstructive pulmonary disease (COPD) in smokers.[285] They found that the mean T_2^* value of the moderate COPD group was significantly different from that of the severe or severe COPD group ($P < 0.05$). UTE MRI is potentially as valuable as multidetector CT for pulmonary function loss assessment and clinical stage classification of COPD in smokers. Recently, UTE sequences have also been employed for lesion-based comparative analysis in patients with COVID-19.[291] UTE-MRI is expected to have significant clinical potential for assessing COVID-19, including screening, diagnosis, surveillance, and treatment monitoring.

UTE MRI has also been developed for morphological and quantitative imaging of the gastrointestinal system. Hematologic disorders such as β-thalassemia and sickle cell anemia require frequent therapeutic blood transfusions to prevent disease complications, but this can lead to iron overload, most notably in the liver, and is treated with
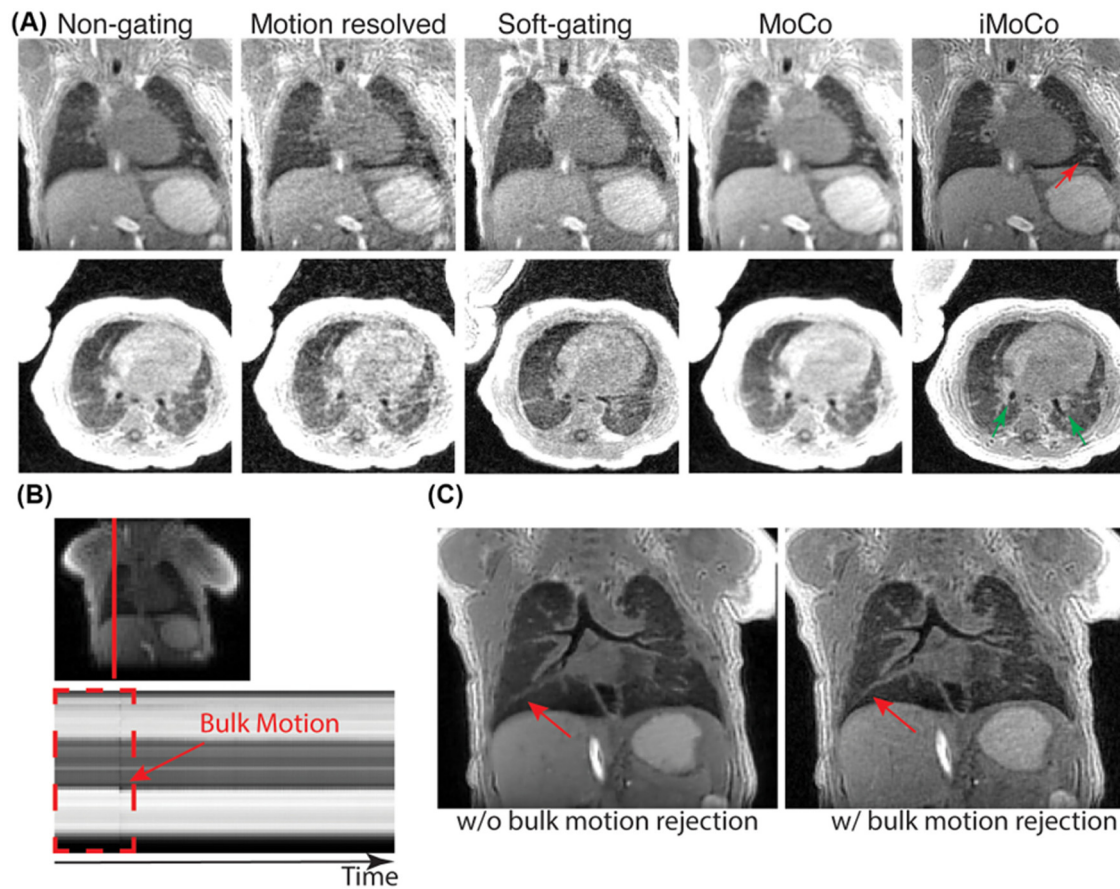
FIG. 30. Volumetric imaging of the lung of a 10-week-old infant. Representative coronal (first row) and axial (second row) slices reconstructed with different motion correction and reconstruction strategies are displayed (a). The iMoCo images depict vessels (red arrows) and airways (green arrows) better than the non-gating, motion resolved, soft-gaging, and MoCo images. An image-based navigator was used to reject data acquired outside the bulk movement (red dashed outline in time window) (b). The iMoCo reconstructed images with bulk motion rejection depict small vessels (red arrows) much better than those without bulk motion rejection (c). Reproduced with permission from Zhu et al., Magn. Reson. Med. **83**, 1208–1221 (2019). Copyright 2019 Wiley.[290]

iron chelation therapy.[292] A reliable quantitative assessment of the hepatic iron content is essential for disease management and monitoring treatment response to iron chelation therapy.[293] Krafft et al. employed UTE T_2^* to quantify hepatic iron content[294] and found that UTE-T_2^* was consistent with biopsied hepatic iron content in patients with massive iron overload at 1.5 and 3 T. A thorough biopsy-referenced trial is needed before the path to clinical adoption of these methods can advance.

D. UTE MRI in the cardiovascular system

UTE sequences have obvious advantages over conventional MRI sequences in imaging complex flow,[295–297] very fast flow,[298] clipped cerebral aneurysms, and coil embolizations,[299,300] as well as vascular calcifications.[301–304] UTE reduces artifacts related to rapid, turbulent flow.[295–298] The self-gated 4D phase contrast UTE sequence provides robust and accurate flow velocity mapping of the mouse heart in vivo at high magnetic fields, with SNR, gating efficiency, flow artifacts, and image quality all improved compared to conventional GRE-based 4D phase contrast imaging.[295] ZTE shows much-reduced susceptibility artifact compared with conventional time-of-flight MR angiography and improved intracranial vascular stenosis assessment.[297] UTE is also less sensitive to off resonance artifacts from metallic implants[305] and is therefore advantageous for imaging clipped aneurysms and coil embolizations.[299,300] Furthermore, UTE allows direct imaging of vascular calcification, which may have a T_2^* value similar to that of cortical bone and make it invisible with conventional MRI.[301–304]

An example of UTE's applicability in the cardiovascular system is carotid plaque calcification which has a major impact on the biomechanical stability of atherosclerotic plaques.[306–308] Particular calcification patterns may help in grading lesions and may further indicate stability.[307] However, there is a lack of a reliable noninvasive imaging technique that can assess carotid plaque calcification with the soft tissue components of atherosclerotic plaques. Conventional MRI provides high signal and contrast for the artery lumen, fibrous tissue, and lipid core, but not carotid plaque calcification, which has a very short T_2 and appears as a signal void, precluding direct imaging and quantitative characterization. Thus, carotid plaque calcification is invisible to

the regular UTE sequence compared with the high signal from the surrounding soft tissues. The IR-UTE sequence, on the other hand, selectively suppresses signals from the long-T_2 tissue components and results in an excellent depiction of carotid plaque calcification.[301–304] There is a strong correlation between IR-UTE and micro-CT morphological images of carotid plaque calcification.[303] Carotid plaque calcification varies significantly from sample to sample, with a significant increase in T_1 and T_2^* with free water concentration and a substantial decrease in free water concentration with mineral density.[304] Therefore, the utility of UTE-based measurements is likely to play an essential role in the management of atherosclerosis.

Another example of the advantages offered by UTE imaging in the cardiovascular context is an endovascular treatment involving coil embolization, which has been widely used to manage both ruptured and unruptured intracranial aneurysms.[299] Radiofrequency shielding and susceptibility artifacts make it difficult to visualize flow in intracranial stents with commonly used 3D time-of-flight MR angiography techniques. UTE-type sequences, such as ZTE, are less sensitive to the susceptibility artifacts associated with metallic devices and can be used for a more accurate assessment of intracranial anterior circulation aneurysms treated with stent-assisted coil embolization. Figure 31 shows an example of a 73-year-old woman. The aneurysm occlusion

FIG. 31. Stent-assisted coil embolization of the anterior communicating artery was performed in a 73-year-old woman with the aneurysm remnant indicated by the long white arrow and stent edges indicated by short black arrows (a). X-ray digital angiography shows the stent edges indicated by short black arrows (b). A minimal signal loss was observed on silent MR angiography at the stented segment (outlined arrow), with the aneurysm remnant well depicted (long white arrow) (c). A complete signal loss was observed in the stented segments (outlined arrows), with the aneurysm remnant invisible in 3D time-of-flight MR angiography (d). Reproduced with permission from Takano *et al.*, Am. J. Neuroradiology **38**, 1610–1616 (2017). Copyright 2017 the American Society of Neuroradiology.[299]

was better depicted with the ZTE MR angiography than with 3D time-of-flight MR angiography.

E. Summary of UTE MRI applications

We have only briefly discussed applications of UTE imaging in the musculoskeletal, nervous, respiratory, gastrointestinal, and cardiovascular systems. There are many other applications as well, including iron-labeled stem cell tracking,[226] where UTE-based T_1, T_2^*, and QSM techniques are expected to help map stem cells, especially when they are labeled with highly concentrated iron (thus resulting in very short T_2^*s).[190,191] UTE MRI can potentially be used to evaluate macrocalcifications, including their water, collagen, and mineral contents in the breast.[187–192,240–242,303] UTE MRI may also find applications in iron oxide nanoparticle-based hyperthermia,[309] where an alternating magnetic field heats the iron oxide nanoparticles for cancer therapy. It is challenging to monitor temperature because of the high concentration of iron oxide nanoparticles, typically on the order of 30 mM or higher,[309] leading to an ultrashort T_2^* of tens to hundreds of microseconds.[189,190] UTE-based techniques can capture these phase changes to monitor T_1 or temperature changes. More research is needed to evaluate UTE performance across myriad clinical applications systematically.

VII. CONCLUSIONS AND OUTLOOK

Direct imaging of short-T_2 tissues can be used to improve the diagnosis of various diseases in the body's musculoskeletal, nervous, respiratory, gastrointestinal, and cardiovascular systems. UTE imaging with high signal, high spatial resolution, and contrast of otherwise invisible tissues or tissue components will likely improve the classification and staging of diseases in a significant way. For example, the most widely used MRI scoring method, known as WORMS,[310] in osteoarthritis MR imaging incorporates 14 features mostly related to articular cartilage, although osteoarthritis is a whole organ disease. There are no widely accepted imaging scoring systems for the menisci, ligaments, tendons, and bone primarily due to the poor signal and contrast that results from conventional MRI. UTE imaging of all significant tissue components in the joint may significantly improve morphological assessment of joint degeneration.

Another example of UTE imaging's potential to reinvent diagnosis and monitoring relates to the Pfirrmann grading system, which is widely used to evaluate intervertebral disk degeneration.[311,312] While the cartilaginous endplate plays a vital role in the transportation of oxygen and nutrients necessary to maintain disk health,[313] it is difficult to image with conventional MRI sequences. High contrast UTE imaging of the cartilaginous endplate, however, is likely to improve the performance of the Pfirrmann grading system.[79–81] The power of combined morphological and quantitative UTE imaging for both short- and long-T_2 tissues facilitates a more comprehensive assessment of tissue degeneration, directly influencing the development and advancement of new grading systems not only for musculoskeletal diseases but other diseases throughout the body as well.

Although UTE imaging has provided excellent preliminary results in many areas, clinical applications are still limited at this stage of the technique's development. The significant challenges in UTE MRI lie in the following areas:

First, short-T_2 imaging is typically associated with low SNR and spatial blurring because of the relatively low proton densities of the
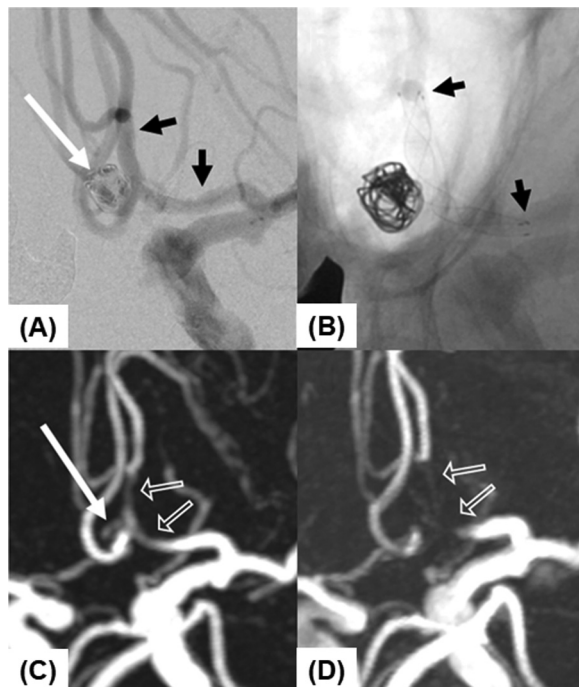
tissues of interest and the fast signal decay during data sampling.[30,32] A short sampling window is required to minimize spatial blurring, which limits spatial resolution.[30] An effective strategy would be to develop stronger gradient and RF systems. For example, Weiger *et al.* employed a high-performance gradient insert that provided a maximum strength of 200 mT/m and a slew rate of 600 mT/m/ms, both of which are 4–5 times stronger than the typical gradient strength of $\sim$40 mT/m and slew rate of $\sim$150 mT/m/ms on clinical scanners.[118] The gradient inserts allowed UTE imaging of short-T_2 tissues such as myelin with higher spatial resolution, less blurring, and higher SNR. A higher power RF system also augments UTE imaging's capabilities as transverse relaxation during RF excitation becomes essential for short-T_2 tissues. A shorter pulse with a higher power helps to minimize signal loss during RF excitation. Local parallel transmission becomes vital in some cases, such as myelin imaging of the brain, where the specific absorption rate (SAR) is limited for safety considerations. The parallel transmission allows stronger RF pulses without SAR constraints[313] and can be used for more efficient excitation of myelin magnetization. This is crucial for accurate myelin density mapping or trabecular bone density mapping. Stronger RF and gradient systems are expected to benefit all UTE-type sequences, particularly STAIR-UTE type sequences, due to the requirement for a short TR to suppress long-T_2 signals[86–88] efficiently.

Second, eddy currents are a significant factor limiting clinical applications. UTE sequences are based on non-Cartesian sampling and are typically more sensitive to eddy current effects than Cartesian techniques.[205,314] 2D UTE sequences are susceptible to eddy currents due to the use of half-pulse excitation, where two acquisitions with opposite slice selection gradient polarities are needed to form a single slice. Eddy currents may shift or distort the k-space trajectories, leading to out-of-slice excitation, affecting morphological and quantitative 2D UTE imaging.[27–29] While the 3D UTE sequences based on nonselective rectangular pulse excitation are less sensitive to eddy currents due to the elimination of slab-selection gradients,[30–37] eddy currents can still distort the radial and spiral trajectories, especially for later echoes in multi-echo acquisitions. Eddy current compensation and k-space trajectory measurement are critical in facilitating more reliable UTE imaging.[205,314] In comparison, ZTE is insensitive to eddy currents because the k-space data are sampled after gradient ramp-up,[46] increasing interest in imaging cortical bone with ZTE sequences.[315,316] ZTE can be used to visualize cortical bone and intraosseous lesions that are occult using CT. A recent study demonstrated that cysts seen with ZTE differed from the subchondral ganglion cysts identified during grading, which were subsequently confirmed in patients' standard-of-care MRI examinations.[315]

Third, quantitative UTE imaging is also subject to long-T_2 water and fat signal contamination errors. Because long-T_2 tissues typically have higher proton densities, long-T_2 signal contamination has a significant impact on the quantification accuracy in short-T_2 imaging. This is especially the case for quantitative imaging of thin structures such as the osteochondral junction (0.1–0.2 mm thick)[317] and the cartilaginous endplate (0.5–1 mm thick), which anchors the disk to the vertebral body and is responsible for nutrient transport and waste product elimination.[318] Regular UTE with variable TEs can be used for T_2^* mapping of these structures, but the value will likely be subject to significant errors due to partial volume effects and long-T_2 signal contamination.[74–78,319] Efficient long-T_2 suppression is a critically

important factor to consider for accurate T_2^* mapping and quantification of T_1, T_2, T_2^*, $T_{1\rho}$, and PD of the cartilaginous endplate, osteochondral junction, trabecular bone, and other short-T_2 tissues.[74–78]

Fourth, fat contamination and related off resonance artifacts are other potential sources of error with UTE imaging.[32,94,102] Fat contamination can significantly affect MR relaxation times (e.g., T_1, T_2, T_2^*, $T_{1\rho}$) and tissue properties (e.g., water content, MMF, susceptibility, perfusion, diffusion). Furthermore, UTE sequences employ center-out radial or spiral mapping of k-space, which can lead to off resonance artifacts (e.g., spatial blurring due to the ring-shaped point spread function) that are notably different from those seen with a Cartesian sampling of k-space.[102] For example, displacements of fat in the red bone marrow of the skull may simulate subdural hematomas. Displacement of perivesical fat signal centrally over the bladder wall mimics a bladder tumor, and displacement of fat signal from red bone marrow in the lumbar spine to the intervertebral disks simulates their cartilaginous endplates.[102] Chemical shift-based artifacts in UTE imaging are significant to recognize as they can easily mimic normal structures and/or diseases.

Fifth, the magic angle effect should be considered in both morphological and quantitative UTE imaging.[158–162] Most short-T_2 tissues are collagen-rich, so their UTE signal intensities can be highly angular-dependent. Many biomarkers, including UTE-T_2^* and UTE-$T_{1\rho}$ also show strong angular dependency. Angular independent biomarkers such as UTE-AdiabT$_{1\rho}$[167–170] and UTE-MT modeling[176–183] may allow more reliable quantification of tissue degeneration and monitoring of treatment. UTE-DESS-derived ADC may also be insensitive to the magic angle effect, but further research on this technique is needed.[203,204]

Finally, UTE MRI requires comprehensive and time-consuming data analysis involving various tissues or tissue components. The successful application and integration of deep learning-based automatic segmentation and quantitative relaxometry could be used to facilitate the translational study of the novel morphological and quantitative UTE MRI techniques discussed herein.[320–323] These advances may have a significant impact on the diagnosis and treatment monitoring of various diseases in the musculoskeletal, nervous, respiratory, gastrointestinal, and cardiovascular systems of the body.

ACKNOWLEDGMENTS

AUTHOR DECLARATIONS
Conflict of Interest

The authors have no conflicts to disclose.

Author Contributions

Yajun Ma, Hyungseok Jang, and Saeed Jerban contributed equally to this paper.

Yajun Ma: Writing – original draft (equal); Writing – review & editing (equal). **Hyungseok Jang:** Writing – original draft (equal); Writing – review & editing (equal). **Saeed Jerban:** Writing – original draft

(equal); Writing – review & editing (equal). **Eric Y Chang:** Writing – original draft (equal); Writing – review & editing (equal). **Christine B Chung:** Writing – original draft (equal); Writing – review & editing (equal). **Graeme M Bydder:** Writing – original draft (equal); Writing – review & editing (equal). **Jiang Du:** Conceptualization (lead); Funding acquisition (lead); Investigation (lead); Methodology (lead); Writing – original draft (lead); Writing – review & editing (lead).

DATA AVAILABILITY

The data that support the findings of this study are available from the corresponding author upon reasonable request.

REFERENCES

[1]P. C. Lauterbur, "Image formation by induced local interactions: Examples of employing nuclear magnetic resonance," Nature **242**, 190–191 (1973).

[2]E. M. Haacke, R. W. Brown, M. R. Thompson, and R. Venkatesan, *Magnetic Resonance Imaging: Physical Principles and Sequence Design* (Wiley-Liss, New York, 1999).

[3]D. B. Plewes and W. Kucharczyk, "Physics of MRI: A primer," J. Magn. Reson. Imaging **35**, 1038–1054 (2012).

[4]L. G. Hanson, "Is quantum mechanics necessary for understanding magnetic resonance?," Concepts Magn. Reson., Part A **32A**, 329–340 (2008).

[5]G. M. Bydder, G. D. Fullerton, and I. R. Young, *MRI of Tissues with Short T2s or T2*s* (Wiley-Liss, New York, 2012).

[6]M. D. Robson, P. D. Gatehouse, M. Bydder, and G. M. Bydder, "Magnetic resonance: An introduction to ultrashort TE (UTE) imaging," J. Comput. Assist Tomogr. **27**, 825–846 (2003).

[7]A. Masoud-Afsahi, Y. Ma, H. Jang, S. Jerban, C. Chung, E. Y. Chang, and J. Du, "Ultrashort echo time (UTE) MRI techniques: MET and UNMET needs in musculoskeletal imaging," J. Magn. Reson. Imaging **55**, 1597–1612 (2022).

[8]S. Mastrogiacomo, W. Dou, J. A. Jansen, and X. F. Walboomers, "Magnetic resonance imaging of hard tissues and hard tissue engineered bio-substitutes," Mol. Imaging Biol. **21**, 1003–1019 (2019).

[9]J. Hennig, "K-space sampling strategies," Eur. Radiol. **9**, 1020–1031 (1999).

[10]I. R. Young, N. M. Szeverenyi, J. Du, and G. M. Bydder, "Pulse sequences as tissue property filter (TP-filters): A way of understanding the signal, contrast and weighting of magnetic resonance images," Quant. Imaging Med. Surg. **10**, 1080–1120 (2020).

[11]W. R. Nitz and P. Reimer, "Contrast mechanisms in MR imaging," Eur. Radiol. **9**, 1032–1046 (1999).

[12]Y. Ma, H. Shao, X. Lu, S. Fan, J. Du, I. R. Young, and G. M. Bydder, "New options for increasing the sensitivity, specificity and scope of synergistic contrast MRI (scMRI) using MASTIR (Multiplied, Added, Subtracted and/or FiTted) pulse sequences," Quant. Imaging Med. Surg. **10**, 2030–2065 (2020).

[13]A. Mezer, A. Rokem, S. Berman, T. Hastie, and B. A. Wandell, "Evaluating quantitative proton-density-mapping methods," Hum. Brain Mapp. **37**, 3623–3635 (2016).

[14]G. E. Gold, E. Han, J. Stainsby, G. A. Wright, J. Brittain, and C. Beaulieu, "Musculoskeletal MRI at 3.0 T: Relaxation times and image contrast," Am. J. Roentgenol. **183**, 343–351 (2004).

[15]N. Stikov, M. Boudreau, I. R. Levesque, C. L. Tardif, J. K. Barral, and G. B. Pike, "On the accuracy of T$_1$ mapping: Searching for common ground," Magn. Reson. Med. **73**, 514–522 (2015).

[16]G. J. Stanisz, E. E. Odrobina, J. Pun, M. Escaravage, S. J. Graham, M. J. Bronskill, and R. M. Henkelman, "T1, T2 relaxation and magnetization transfer in tissue at 3T," Magn. Reson. Med. **54**, 507–512 (2005).

[17]N. Ben-Eliezer, D. K. Sodickson, and T. K. Block, "Rapid and accurate T2 mapping from multi-spin echo data using Block-simulation-based reconstruction," Magn. Reson. Med. **73**, 809–817 (2015).

[18]M. Chalian, X. Li, A Guermazi et al., "The QIBA profile for MRI-based compositional imaging of knee cartilage," Radiology **301**, 423–432 (2021).

[19]P. Triadyaksa, M. Oudkerk, and P. E. Sijens, "Cardiac T2* mapping: Techniques and clinical applications," J. Magn. Reson. Imaging **52**, 1340–1351 (2020).

[20]U. Duvvuri, R. Reddy, S. D. Patel, J. H. Kaufman, J. B. Kneeland, and J. S. Leigh, "T1rho-relaxation in articular cartilage: Effects of enzymatic degradation," Magn. Reson. Med. **38**, 863–867 (1997).

[21]R. R. Regatte, S. V. S. Akella, A. J. Wheaton, G. Lech, A. Borthakur, J. B. Kneeland, and R. Reddy, "3D-T1ρ-relaxation mapping of articular cartilage: *In vivo* assessment of early degenerative changes in symptomatic osteoarthritic subjects," Acad. Radiol. **11**, 741–749 (2004).

[22]X. Li, B. Ma, T. M. Link, D. Castillo, G. Blumenkrantz, J. Lozano, J. Carballido-Gamio, M. Ries, and S. Majumdar, "*In vivo* T1ρ and T2 mapping of articular cartilage in osteoarthritis of the knee using 3T MRI," Osteoarthritis Cartilage **15**, 789–797 (2007).

[23]J. G. Sled and G. B. Pike, "Quantitative imaging of magnetization transfer exchange and relaxation properties *in vivo* using MRI," Magn. Reson. Med. **46**, 923–931 (2001).

[24]J. F. Griffith, D. K. W. Yeung, G. E. Antonio et al., "Vertebral bone mineral density, marrow perfusion, and fat content in healthy men and men with osteoporosis: Dynamic contrast-enhanced MR imaging and MR spectroscopy," Radiology **236**, 945–951 (2005).

[25]D. Le Bihan, E. Breton, D. Lallemand, P. Grenier, E. Cabanis, and M. Laval-Jeantet, "MR imaging of intravoxel incoherent motions: Application to diffusion and perfusion in neurologic disorders," Radiology **161**, 401–407 (1986).

[26]Y. Wang and T. Liu, "Quantitative susceptibility mapping (QSM): Decoding MRI data for a tissue magnetic biomarker," Magn. Reson. Med. **73**, 82–101 (2015).

[27]S. Conolly, D. Nishimura, A. Macovski, and G. Glover, "Variable-rate selective excitation," J. Magn. Reson. **78**, 440–458 (1988).

[28]G. E. Gold, D. R. Thedens, J. M. Pauly et al., "MR imaging of articular cartilage of the knee: New methods using ultrashort TEs," Am. J. Roentgenol. **170**, 1223–1226 (1998).

[29]J. Du, A. Takahashi, M. Bydder, and C. B. Chung, "Two dimensional ultrashort echo time imaging using a spiral trajectory," Magn. Reson. Imaging **26**, 304–312 (2008).

[30]J. Rahmer, P. Bornert, J. Groen, and C. Bos, "Three-dimensional radial ultrashort echo-time imaging with T2 adapted sampling," Magn. Reson. Med. **55**, 1075–1082 (2006).

[31]A. Techawiboonwong, H. K. Song, M. B. Leonard, and F. W. Wehrli, "Cortical bone water: *In vivo quantification* with ultrashort echo-time MR imaging," Radiology **248**, 824–833 (2008).

[32]J. Du, M. Bydder, A. M. Takahashi, M. Carl, C. B. Chung, and G. M. Bydder, "Short T2 contrast with three-dimensional ultrashort echo time imaging," Magn. Reson. Imaging **29**, 470–482 (2011).

[33]R. Krug, P. E. Z. Larson, C. Wang, A. J. Burghardt, D. A. C. Kelley, T. M. Link, X. Zhang, D. B. Vigneron, and S. Majumdar, "Ultrashort echo time MRI of cortical bone at 7 T field strength: A feasibility study," J. Magn. Reson. Imaging **34**, 691–595 (2011).

[34]P. E. Z. Larson, M. Han, R. Krug et al., "Ultrashort echo time and zero echo time MRI at 7 T," MAGMA **29**, 359–370 (2016).

[35]F. E. Boada, J. S. Gillen, G. X. Shen, S. Y. Chang, and K. R. Thulborn, "Fast three dimensional sodium imaging," Magn. Reson. Med. **37**, 706–715 (1997).

[36]P. T. Gurney, B. A. Hargreaves, and D. G. Nishimura, "Design and analysis of a practical 3D cones trajectory," Magn. Reson. Med. **55**, 575–582 (2006).

[37]M. Carl, G. M. Bydder, and J. Du, "UTE imaging with simultaneous water and fat signal suppression using a time-efficient multi-spoke inversion recovery pulse sequence," Magn. Reson. Med. **76**, 577–582 (2016).

[38]B. J. Balcom, "Single-point ramped imaging with T-1 enhancement," J. Magn. Reson. A **123**, 131–134 (1996).

[39]Z. Fang, D. Hoepfel, and K. Winter, "Application of single point imaging (SPI) to solid state materials," Magn. Reson. Imaging **19**, 501–503 (2001).

[40]Y. Wu, D. A. Chesler, M. L. Glimcher, L. Garrido, J. Wang, H. J. Jiang, and J. L. Ackerman, "Multinuclear solid state three dimensional MRI of bone and synthetic calcium phosphates," Proc. Natl. Acad. Sci. U. S. A. **96**, 1574–1578 (1999).

[41]H. Cao, J. L. Ackerman, M. I. Hrovat, L. Graham, M. J. Glimcher, and Y. Wu, "Quantitative bone matrix density measurement by water- and fat-suppressed proton projection MRI (WASPI) with polymer calibration phantoms," Magn. Reson. Med. **60**, 1433–1443 (2008).

[42]D. Idiyatullin, C. Corum, J. Y. Park, and M. Garwood, "Fast and quiet MRI using a swept radiofrequency," J. Magn. Reson. **181**, 342–349 (2006).

[43]Y. Qian, A. Williams, C. R. Chu, and F. E. Boada, "High-resolution ultrashort echo time (UTE) imaging on human knee with AWSOS sequence at 3.0 T," J. Magn. Reson. Imaging **35**, 204–210 (2012).

[44]D. M. Grodzki, P. M. Jakob, and B. Heismann, "Ultrashort echo time imaging using pointwise encoding time reduction with radial acquisition (PETRA)," Magn. Reson. Med. **67**, 510–518 (2012).

[45]H. Jang, C. N. Wiens, and A. B. McMillan, "Ramped hybrid encoding for improved ultrashort echo time imaging," Magn. Reson. Med. **76**, 814–825 (2016).

[46]M. Weiger, K. P. Pruessmann, and F. Hennel, "MRI with zero echo time: Hard versus sweep pulse excitation," Magn. Reson. Med. **66**, 379–389 (2011).

[47]Y. J. Kim, J. G. Cha, Y. S. Shin, A. S. Chaudhari, Y. J. Suh, S. H. Yoon, and G. E. Gold, "3D ultrashort TE MRI for evaluation of cartilaginous endplate of cervical disk *in vivo*: Feasibility and correction with disk degeneration in T2-weighted spin-echo sequence," Am. J. Roentgenol. **210**, 1131–1140 (2018).

[48]J. Rahmer, P. Bornert, and S. P. M. Dries, "Assessment of anterior cruciate ligament reconstruction using 3D ultrashort echo-time MR imaging," J. Magn. Reson. Imaging **29**, 443–448 (2009).

[49]M. S. Sussman, J. M. Pauly, and G. A. Wright, "Design of practical T2-selective RF excitation (TELEX) pulses," Magn. Reson. Med. **40**, 890–899 (1998).

[50]P. E. Larson, P. T. Gurney, K. Nayak, G. E. Gold, J. M. Pauly, and D. G. Nishimura, "Designing long-T2 suppression pulses for ultrashort echo time imaging," Magn. Reson. Med. **56**, 94–103 (2006).

[51]C. Li, J. F. Magland, H. S. Rad, H. W. Song, and F. W. Wehrli, "Comparison of optimized soft-tissue suppression schemes for ultra-short echo time (UTE) MRI," Magn. Reson. Med. **68**, 680–689 (2012).

[52]J. Du, A. Takahashi, M. Bydder, C. B. Chung, and G. M. Bydder, "Ultrashort TE imaging with off-resonance saturation contrast (UTE-OSC)," Magn. Reson. Med. **62**, 527–531 (2009).

[53]J. Rautiainen, E. N. Salo, V. Tiitu, M. A. J. Finnila, O. M. Aho, S. Saarakkala, P. Lehenkari, J. Ellermann, M. J. Nissi, and M. T. Nieminen, "Assessment of human tibial cartilage-bone interface in osteoarthritis using SWIFT," in *Proceedings of ISMRM 21st Annual Meeting, Salt Lake City, Utah, USA* (ISMRM, 2013), p. P0434.

[54]H. Wei, P. Cao, A. Bischof, R. G. Henry, P. E. Z. Larson, and C. Liu, "MRI gradient-echo phase contrast of the brain at ultra-short TE with off-resonance saturation," NeuroImage **175**, 1–11 (2018).

[55]A. Waldman, J. H. Rees, C. S. Brock, M. D. Robson, P. D. Gatehouse, and G. M. Bydder, "MRI of the brain with ultra-short echo time pulse sequences," Neuroradiology **45**, 887–892 (2003).

[56]I. L. H. Reichert, M. D. Robson, P. D. Gatehouse, T. He, K. E. Chappell, J. Holmes, S. Girgis, and G. M. Bydder, "Magnetic resonance imaging of cortical bone with ultrashort TE pulse sequences," Magn. Reson. Imaging **23**, 611–618 (2005).

[57]P. E. Larson, S. M. Conolly, J. M. Pauly, and D. G. Nishimura, "Using adiabatic inversion pulses for long-T2 suppression in ultrashort echo time (UTE) imaging," Magn. Reson. Med. **58**, 952–961 (2007).

[58]J. Du, M. Carl, M. Bydder, A. Takahashi, C. B. Chung, and G. M. Bydder, "Qualitative and quantitative ultrashort echo time (UTE) imaging of cortical bone," J. Magn. Reson. **207**, 304–311 (2010).

[59]R. Horch, D. Gochberg, J. Nyman, and M. Does, "Clinically-compatible MRI strategies for discriminating bound and pore water in cortical bone," Magn. Reson. Med. **68**, 1774–1784 (2012).

[60]J. Du and G. M. Bydder, "Qualitative and quantitative ultrashort-TE MRI of cortical bone," NMR Biomed. **26**, 489–506 (2013).

[61]Y. Ma, S. Fan, H. Shao, J. Du, N. M. Szeverenyi, I. R. Young, and G. M. Bydder, "Clinical use of multiplied, subtracted and/or fitted inversion recovery (MASTIR) pulse sequences," Quant. Imaging Med. Surg. **10**, 1334–1369 (2020).

[62]M. Garwood and L. DelaBarre, "The return of the frequency sweep: Designing adiabatic pulses for contemporary NMR," J. Magn. Reson. **153**, 155–177 (2001).

[63]R. A. Horch, J. C. Gore, and M. D. Does, "Origins of the ultrashort T2 1H NMR signals in myelinated nerve: A direct measure of myelin content?," Magn. Reson. Med. **66**, 24–31 (2011).

[64]M. J. Wilhelm, H. H. Ong, S. L. Wehrli, C. Li, P. H. Tsai, D. B. Hackney, and F. W. Wehrli, "Direct magnetic resonance detection of myelin and prospects for quantitative imaging of myelin density," Proc. Natl. Acad. Sci. U. S. A. **109**, 9605–9610 (2012).

[65]J. Du, G. Ma, S. Li, M. Carl, N. Szeverenyi, S. VandenBerg, J. Corey-Bloom, and G. M. Bydder, "Ultrashort TE echo time (UTE) magnetic resonance imaging of the short T2 components in white matter of the brain using a clinical 3T scanner," NeuroImage **87**, 32–41 (2013).

[66]J. Du, V. Sheth, Q. He, M. Carl, J. Chen, J. Corey-Bloom, G. M. Bydder, and J. Du, "Measurement of T1 of the ultrashort T2* components in white matter of the brain at 3T," PLosOne **9**, e103296 (2013).

[67]V. Sheth, H. Shao, J. Chen, S. VandenBerg, J. Corey-Bloom, G. M. Bydder, and J. Du, "Magnetic resonance imaging of myelin using ultrashort echo time (UTE) pulse sequence: Phantom, specimen, volunteers and multiple sclerosis patient studies," NeuroImage **136**, 37–44 (2016).

[68]V. Sheth, S. Fan, Q. He, Y. Ma, J. Annesse, R. Switzer, J. Corey-Bloom, G. M. Bydder, and J. Du, "Inversion recovery UTE magnetic resonance imaging: A method for simultaneous direct detection of myelin and high signal demonstration of iron deposition in the brain—A feasibility study," Magn. Reson. Imaging **38**, 87–94 (2017).

[69]Q. He, M. Ma, H. Shao, V. Sheth, G. Bydder, and J. Du, "Direct magnitude and phase imaging of myelin using ultrashort echo time (UTE) pulse sequences: A feasibility study," Magn. Reson. Imaging **39**, 194–199 (2017).

[70]S. Fan, Y. Ma, E. Y. Chang, G. M. Bydder, and J. Du, "Inversion recovery ultrashort echo time imaging of ultrahort T_2 tissue components in ovine brain at 3T: A sequential D_2O exchange study," NMR Biomed. **30**, e3767 (2017).

[71]S. Fan, Y. Ma, A. Searleman, Y. Zhu, G. M. Bydder, and J. Du, "Yet more evidence that myelin protons can be directly imaged with ultrashort echo time (UTE) sequences on a clinical 3T scanner: Bi-component T2* analysis of native and deuterated ovine brain specimens," Magn. Reson. Med. **80**, 538–547 (2018).

[72]H. Jang, Y. Ma, A. C. Searleman, M. Carl, J. Corey-Bloom, E. Y. Chang, and J. Du, "Inversion recovery UTE based volumetric myelin imaging in human brain using interleaved hybrid encoding," Magn. Reson. Med. **83**, 950–961 (2020).

[73]Y. Ma, H. Jang, Chang, E. Y *et al.*, "Ultrashort echo time (UTE) magnetic resonance imaging of myelin: Technical developments and challenges," Quant. Imaging Med. Surg. **10**, 1186–1203 (2020).

[74]J. Du, A. Takahashi, W. C. Bae, C. B. Chung, and G. M. Bydder, "Dual inversion recovery, ultrashort echo time (DIR UTE) imaging: Creating high contrast for short-T2 species," Magn. Reson. Med. **63**, 447–455 (2010).

[75]W. Bae, J. R. Dwek, R. Znamirowski, S. Statum, J. C. Hermida, D. D. D'Lima, R. L. Sah, J. Du, and C. B. Chung, "Ultrashort echo time MR imaging of osteochondral junction of the knee at 3 T: Identification of anatomic structures contributing to signal intensity," Radiology **254**, 837–845 (2009).

[76]J. Du, M. Carl, W. C. Bae, S. Statum, E. Y. Chang, G. M. Bydder, and C. B. Chung, "Dual inversion recovery ultrashort echo time (DIR-UTE) imaging and quantification of the zone of calcified cartilage (ZCC)," Osteoarthritis Cartilage **21**, 77–85 (2013).

[77]Y. J. Ma, Y. Zhu, X. Lu, M. Carl, E. Y. Chang, and J. Du, "Short T2 imaging using a 3D double adiabatic inversion recovery prepared ultrashort echo time cones (3D DIR-UTE-Cones) sequence," Magn. Reson. Med. **79**, 2555–2563 (2018).

[78]Y. Ma, S. Jerban, M. Carl, L. Wan, T. Guo, H. Jang, G. M. Bydder, E. Y. Chang, and J. Du, "Imaging of the region of the osteochondral junction (OCJ) using a 3D adiabatic inversion recovery prepared ultrashort echo time Cones (3D IR-UTE Cones) sequence at 3T," NMR Biomed. **32**, e4080 (2019).

[79]Z. Wei, A. Lombardi, R. Lee, M. Wallace, M. Koichi, E. Y. Chang, J. Du, G. M. Bydder, W. Yang, and Y. Ma, "Comprehensive assessment of *in vivo* lumbar spine intervertebral discs using a 3D adiabatic $T_{1\rho}$ prepared ultrashort echo time (UTE-Adiab-$T_{1\rho}$) pulse sequence," Quant. Imaging Med. Surg. **12**, 269–280 (2022).

[80]A. Lombardi, Z. Wei, J. Wong, M. Carl, R. Lee, M. Wallace, M. Koichi, E. Y. Chang, J. Du, and Y. Ma, "High contrast cartilaginous endplate imaging using a 3D adiabatic inversion-recovery-prepared fat-saturated ultrashort echo time (3D IR-FS-UTE) sequence," NMR Biomed. **34**, e4579 (2021).

[81] A. J. Fields, M. Han, R. Krug, and J. C. Lotz, "Cartilaginous end plates: Quantitative MR imaging with very short echo times—orientation dependence and correlation with biochemical composition," Radiology **274**, 482–489 (2015).

[82] Y. J. Ma, X. Lu, M. Carl, Y. Zhu, N. M. Szeverenyi, G. M. Bydder et al., "Accurate T1 mapping of short T2 tissues using a three-dimensional ultrashort echo time cones actual flip angle imaging-variable repetition time (3D UTE-Cones AFI-VTR) method," Magn. Reson. Med. **80**, 598–608 (2018).

[83] Y. J. Ma, W. Zhao, L. Wan, T. Guo, A. Searleman, H. Jang, et al., "Whole knee joint T1 values measured in vivo at 3T by combined 3D ultrashort echo time cones actual flip angle and variable flip angle methods," Magn. Reson. Med. **81**, 1634–1644 (2019).

[84] Z. Cai, Z. Wei, M. Wu, S. Jerban, H. Jang, S. Li et al., "Knee osteochondral junction imaging using a fast 3D T1-weighted ultrashort echo time cones sequence at 3T," Magn. Reson. Imaging **73**, 76–83 (2020).

[85] H. Jang, Y. Ma, M. Carl, A. F. Lombardi, E. Y. Chang, and J. Du, "Feasibility of an inversion recovery-prepared fat-saturated zero echo time sequence for high contrast imaging of the osteochondral junction," Front. Endocrinol. **12**, 777080 (2021).

[86] Y. Ma, H. Jang, Z. Wei, Z. Cai, Y. Xue, E. Y. Chang, J. Corey-Bloom, and J. Du, "Myelin imaging in human brain using a short repetition time adiabatic inversion recovery prepared ultrashort echo time (STAIR-UTE) MRI sequence in multiple sclerosis," Radiology **297**, 392–404 (2020).

[87] Y. Ma, H. Jang, Z. Wei, M. Wu, E. Y. Chang, J. Corey-Bloom, G. M. Bydder, and J. Du, "Brain ultrashort T2 component imaging using a short TR adiabatic inversion recovery prepared dual-echo ultrashort TE sequence with complex echo subtraction (STAIR-dUTE-ES)," J. Magn. Reson. **323**, 106898 (2021).

[88] Y. Ma, Y. Chen, L. Li, Z. Cai, W. Zhao, S. Jerban, H. Jang, E. Y. Chang, and J. Du, "Trabecular bone imaging using a 3D adiabatic inversion recovery prepared ultrashort echo time cones sequence at 3T," Magn. Reson. Med. **83**, 1640–1651 (2020).

[89] M. C. Wurnig, M. Calcagni, D. Kenkel, M. Vich, M. Weiger, G. Andreisek, F. W. Wehrli, and A. Boss, "Characterization of trabecular bone density with ultra-short echo-time MRI at 1.5, 3.0, and 7.0 T - comparison with micro-computed tomography," NMR Biomed. **27**, 1159–1166 (2014).

[90] S. Jerban, Y. Ma, Z. Wei, H. Jang, E. Y. Chang, and J. Du, "Quantitative magnetic resonance imaging of cortical and trabecular bone," Semin. Musculoskeletal Radiol. **24**, 386–401 (2020).

[91] S. Jerban, X. Lu, E. W. Dorthe, S. Alenezi, Y. Ma, L. Kakos, H. Jang, R. L. Sah, E. Y. Chang, D. D'Lima, and J. Du, "Correlation of cortical bone microstructural and mechanical properties with water proton fractions obtained from ultrashort echo time (UTE) MRI tricomponent T2* model," NMR Biomed. **33**, e4233 (2020).

[92] Y. Ma, S. Jerban, H. Jang, D. Chang, E. Y. Chang, and J. Du, "Quantitative ultrashort echo time (UTE) magnetic resonance imaging of bone: An update," Front. Endocrinol. **11**, 667–676 (2020).

[93] M. Carl, Y. Ma, and J. Du, "Theoretical analysis and optimization of ultrashort echo time (UTE) imaging contrast with off-resonance saturation," Magn. Reson. Imaging **50**, 12–16 (2018).

[94] D. J. Tyler, M. D. Robson, R. M. Henkelman, I. R. Young, and G. M. Bydder, "Magnetic resonance imaging with ultrashort TE (UTE) pulse sequence: Technical considerations," J. Magn. Reson. Imaging **25**, 279–289 (2007).

[95] W. T. Dixon, "Simple proton spectroscopic imaging," Radiology **153**, 189–194 (1984).

[96] S. B. Reeder, A. R. Pineda, Z. Wen et al., "Iterative decomposition of water and fat with echo asymmetry and least-squares estimation (IDEAL): Application with fast spin-echo imaging," Magn. Reson. Med. **54**, 636–644 (2005).

[97] K. Wang, H. Yu, J. H. Brittain, S. Reeder, and J. Du, "K-space water-fat decomposition with T2* estimation and multifrequency fat spectrum modeling for ultrashort echo time imaging," J. Magn. Reson. Imaging **31**, 1027–1034 (2010).

[98] H. Yu, S. B. Reeder, C. A. McKenzie, A. C. S. Brau, A. Shimakawa, J. H. Brittain, and N. J. Pelc, "Single acquisition water-fat separation: Feasibility study for dynamic imaging," Magn. Reson. Med. **55**, 413–422 (2006).

[99] J. Ma, "A single-point dixon technique for fat-suppressed fast 3D gradient-echo imaging with a flexible echo time," J. Magn. Reson. Imaging **27**, 881–890 (2008).

[100] H. Jang, M. Carl, Y. Ma, S. Jerban, T. Guo, W. Zhao, E. Chang, and J. Du, "Fat suppression for ultrashort echo time imaging using a single point dixon method," NMR Biomed. **32**, e4069 (2019).

[101] S. Kronthaler, C. Boehm, G. Feuerriegel, P. Börnert, U. Katscher, K. Weiss, M. R. Makowski, B. J. Schwaiger, A. S. Gersing, and D. C. Karampinos, "Assessment of vertebral fractures and edema of the thoracolumbar spine based on water-fat and susceptibility-weighted images derived from a single ultra-short echo time scan," Magn. Reson. Med. **87**, 1771–1783 (2022).

[102] M. Bydder, M. Carl, G. M. Bydder, and J. Du, "MRI chemical shift artifact produced by center-out radial sampling of k-space: A potential pitfall in clinical diagnosis," Quant. Imaging Med. Surg. **11**, 3677–3683 (2021).

[103] M. Carl, A. Nazaran, G. M. Bydder, and J. Du, "Effects of fat saturation on short T2 quantification," Magn. Reson. Imaging **43**, 6–9 (2017).

[104] R. M. Henkelman, G. J. Stanisz, and S. J. Graham, "Magnetization transfer in MRI: A review," NMR Biomed. **14**, 57–64 (2001).

[105] S. Li, L. Ma, E. Y. Chang, H. Shao, J. Chen, C. B. Chung, G. M. Bydder, and J. Du, "Effects of inversion time on inversion recovery prepared ultrashort echo time (IR-UTE) imaging of bound and pore water in cortical bone," NMR Biomed. **28**, 70–78 (2015).

[106] F. Springer, G. Steidle, P. Martirosian, U. Grosse, R. Syha, C. Schabel, C. D. Claussen, and F. Schick, "Quick water-selective excitation of fast relaxing tissues with 3D UTE sequences," Magn. Reson. Med. **71**, 534–543 (2014).

[107] F. Schick, "Simultaneous highly selective MR water and fat imaging using a simple new type of spectral-spatial excitation," Magn. Reson. Med. **40**, 194–202 (1998).

[108] Y. Ma, S. Jerban, H. Jang, E. Y. Chang, and J. Du, "Fat suppression for UTE imaging using a novel soft-hard composite RF pulse," Magn. Reson. Med. **82**, 2178–2187 (2019).

[109] T. R. Brown, B. M. Kincaid, and K. Ugurbil, "NMR chemical shift imaging in three dimensions," Proc. Natl. Acad. Sci. U. S. A. **79**, 3523–3526 (1982).

[110] J. Du, G. Hamilton, A. Takahashi, M. Bydder, and C. B. Chung, "Ultrashort echo time spectroscopic imaging (UTESI) of cortical bone," Magn. Reson. Med. **58**, 1001–1009 (2007).

[111] J. Du, A. M. Takahashi, and C. B. Chung, "Ultrashort TE spectroscopic imaging (UTESI): Application to the imaging of short T2 relaxation tissues in the musculoskeletal system," J. Magn. Reson. Imaging **29**, 412–421 (2009).

[112] J. Du, A. J. Chiang, C. B. Chung, S. Statum, R. Znamirowski, A. M. Takahashi, and G. M. Bydder, "Orientational analysis of the Achilles tendon and enthesis using an ultrashort echo time spectroscopic imaging sequence," Magn. Reson. Imaging **28**, 178–184 (2010).

[113] J. Du, T. J. Carroll, E. Brodsky, A. M. Lu, T. M. Grist, C. A. Mistretta, and W. F. Block, "Contrast enhanced peripheral magnetic resonance angiography using time-resolved vastly undersampled isotropic projection reconstruction," J. Magn. Reson. Imaging **20**, 894–900 (2004).

[114] H. K. Song and L. Dougherty, "Dynamic MRI with projection reconstruction and KWIC processing for simultaneous high spatial and temporal resolution," Magn. Reson. Med. **52**, 815–824 (2004).

[115] C. A. Mistretta, O. Wieben, J. Velikina, W. Block, J. Perry, Y. Wu, K. Johnson, and Y. Wu, "Highly constrained backprojection for time-resolved MRI," Magn. Reson. Med. **55**, 30–40 (2006).

[116] H. Jang, M. Carl, Y. Ma, A. C. Searleman, S. Jerban, E. Y. Chang, J. Corey-Bloom, and J. Du, "Inversion recovery zero echo time (IR-ZTE) imaging for direct myelin detection in human brain: A feasibility study," Quant. Imaging Med. Surg. **10**, 895–906 (2020).

[117] A. C. Seifert, C. Li, M. J. Wilhelm, S. L. Wehrli, and F. W. Wehrli, "Towards quantification of myelin by solid-state MRI of the lipid matrix protons," NeuroImage **163**, 358–367 (2017).

[118] M. Weiger, R. Froidevaux, E. L. Baadsvik, D. O. Brunner, M. B. Rosler, and K. P. Pruessmann, "Advances in MRI of the myelin bilayer," NeuroImage **217**, 116888 (2020).

[119] C. Li, J. F. Magland, X. Zhao, A. C. Seifert, and F. W. Wehrli, "Selective in vivo bone imaging with long-T suppressed PETRA MRI," Magn. Reson. Med. **77**, 989–997 (2017).

[120] F. Eckstein, D. Burstein, and T. M. Link, "Quantitative MRI of cartilage and bone: Degenerative changes in osteoarthritis," NMR Biomed. **19**, 822–854 (2006).

[121] R. de Mello, Y. Ma, Y. Ji, J. Du, and E. Y. Chang, "Quantitative MRI MSK techniques: An update," Am. J. Roentgenol. **213**, 524–533 (2019).

[122]J. C. van den Noort, M. Maas, E. H. G. Oei, and R. Hemke, "Quantitative MRI and imaging biomarkers of the musculoskeletal system," in *Imaging of Motion & Performance: Stress & Strain*, edited by A. Vieira, L. Sconfienza, and F. Kainberger (European Society of Radiology, Vienna, 2019), pp. 176–181.

[123]A. Techawiboonwong, H. K. Song, and F. W. Wehrli, "*In vivo* MRI of submillisecond T2 species with two-dimensional and three-dimensional radial sequences and applications to the measurement of cortical bone water," NMR Biomed. **21**, 59–70 (2008).

[124]H. S. Rad, S. C. Lam, J. F. Magland, H. Ong, C. Li, H. K. Song, J. Love, and F. W. Wehrli, "Quantifying cortical bone water *in vivo* by three-dimensional ultra-short echo-time MRI," NMR Biomed. **24**, 855–864 (2011).

[125]S. Rajapakse, M. Bashoor-Zadeh, C. Li, W. Sun, A. C. Wright, and F. W. Wehrli, "Volumetric cortical bone porosity assessment with MR imaging: Validation and clinical feasibility," Radiology **276**, 526–535 (2015).

[126]J. Chen, S. Grawn, H. Shao, D. D'Lima, G. M. Bydder, and J. Du, "Evaluation of bound and pore water in cortical bone using ultrashort echo time (UTE) magnetic resonance imaging," NMR Biomed. **28**, 1754–1762 (2015).

[127]M. K. Manhard, S. Uppuganti, M. Granke, D. F. Gochberg, J. S. Nyman, and M. D. Does, "MRI-derived bound and pore water concentrations as predictors of fracture resistance," Bone **87**, 1–10 (2016).

[128]S. C. Deoni, B. K. Rutt, and T. M. Peters, "Rapid combined T$_1$ and T2 mapping using gradient recalled acquisition in the steady state," Magn. Reson. Med. **49**, 515–526 (2003).

[129]V. L. Yarnykh, "Actual flip-angle imaging in the pulsed steady state: A method for rapid three-dimensional mapping of the transmitted radiofrequency field," Magn. Reson. Med. **57**, 192–200 (2007).

[130]C. R. Chu, A. A. Williams, R. V. West, Y. Qian, F. H. Fu, B. H. Do, and S. Bruno, "Quantitative magnetic resonance imaging UTE-T2* mapping of cartilage and meniscus healing after anatomic anterior cruciate ligament reconstruction," Am. J. Sports Med. **42**, 1847–1856 (2014).

[131]A. Williams, Y. Qian, D. Bear, and C. R. Chu, "Assessing degeneration of human articular cartilage with ultra-short echo time (UTE) T2* mapping," Osteoarthritis Cartilage **18**, 539–546 (2010).

[132]A. Williams, Y. Qian, and C. R. Chu, "UTE-T2* mapping of human articular cartilage *in vivo*: A repeatability assessment," Osteoarthritis Cartilage **19**, 84–88 (2011).

[133]A. Williams, Y. Qian, S. Golla, and C. R. Chu, "UTE-T2* mapping detects subclinical meniscus injury after anterior cruciate ligament tear," Osteoarthritis Cartilage **20**, 486–494 (2012).

[134]S. J. Graham, P. L. Stanchev, and M. J. Bronskill, "Criteria for analysis of multicomponent tissue T2 relaxation data," Magn. Reson. Med. **35**, 370–378 (1996).

[135]D. A. Reiter, P. C. Lin, K. W. Fishbein, and R. G. Spencer, "Multicomponent T2 relaxation analysis in cartilage," Magn. Reson. Med. **61**, 803–809 (2009).

[136]K. P. Whittall and A. L. MacKay, "Quantitative interpretation of NMR relaxation data," J. Magn. Reson. **84**, 134–152 (1969).

[137]Y. Qian, A. Williams, C. R. Chu, and F. E. Boada, "Multi-component T2* mapping of knee cartilage: Technical feasibility *ex vivo*," Magn. Reson. Med. **64**, 1426–1431 (2010).

[138]E. Diaz, C. B. Chung, W. C. Bae *et al.*, "Ultrashort echo time spectroscopic imaging (UTESI): An efficient method for quantifying bound and free water," NMR Biomed. **25**, 161–168 (2012).

[139]J. Du, E. Diaz, M. Carl, W. Bae, C. Chung, and G. M. Bydder, "Ultrashort echo time imaging with bicomponent analysis," Magn. Reson. Med. **67**, 645–649 (2012).

[140]R. Biswas, W. Bae, E. Diaz *et al.*, "Ultrashort echo time (UTE) imaging with bi-component analysis: Bound and free water evaluation of bovine cortical bone subject to sequential drying," Bone **50**, 749–755 (2012).

[141]W. C. Bae, P. C. Chen, C. B. Chung, K. Masuda, D. D'Lima, and J. Du, "Quantitative ultrashort echo time (UTE) MRI of human cortical bone: Correlation with porosity and biomechanical properties," J. Bone Miner. Res. **27**, 848–857 (2012).

[142]C. Pauli, W. C. Bae, M. Lee *et al.*, "Ultrashort-echo time MR imaging of the patella with bicomponent analysis: Correlation with histopathologic and polarized light microscopic findings," Radiology **264**, 484–493 (2012).

[143]H. Shao, E. Y. Chang, S. Zanganeh *et al.*, "UTE bi-component analysis of T2* relaxation in articular cartilage," Osteoarthritis Cartilage **24**, 364–373 (2016).

[144]R. Kijowski, J. J. Wilson, and F. Liu, "Bicomponent ultrashort echo time T2* analysis for assessment of patients with patellar tendinopathy," J. Magn. Reson. Imaging **46**, 1441–1447 (2017).

[145]S. J. Breda, R. J. de Vos, D. H. J. Poot, G. P. Krestin, J. A. Hernandez-Tamames, and E. H. G. Oei, "Association between T2* relaxation times derived from ultrashort echo time MRI and symptoms during exercise therapy for patellar tendinopathy: A large prospective study," J. Magn. Reson. Imaging **54**, 1596–1605 (2021).

[146]Y. X. Wang, J. Yuan, E. S. Chu, M. Y. Go, H. Huang, A. T. Ahuja, J. J. Sung, and J. Yu, "T1ρ MR imaging is sensitive to evaluate liver fibrosis: An experimental study in a rat biliary duct ligation model," Radiology **259**, 712–719 (2011).

[147]T. Allkemper, F. Sagmeister, V. Cicinnati, S. Beckebaum, H. Kooijman, C. Kanthak, C. Stehling, and W. Heindel, "Evaluation of fibrotic liver disease with whole-liver T1ρ MR imaging: A feasibility study at 1.5 T," Radiology **271**, 408–415 (2014).

[148]A. Virta, M. Komu, N. Lundbom, and M. Kormano, "T1 rho MR imaging characteristics of human anterior tibial and gastrocnemius muscles," Acad. Radiol. **5**, 104–110 (1998).

[149]A. E. Lamminen, J. I. Tanttu, R. E. Sepponen, H. Pihko, and O. A. Korhola, "T1 rho dispersion imaging of diseased muscle tissue," Br. J. Radiol. **66**, 783–787 (1993).

[150]W. Johannessen, J. D. Auerbach, A. J. Wheaton *et al.*, "Assessment of human disc degeneration and proteoglycan content using T1rho-weighted magnetic resonance imaging," Spine **31**, 1253–1257 (2006).

[151]Y. X. Wang, F. Zhao, J. F. Griffith, G. S. Mok, J. C. Leung, A. T. Ahuja, and J. Yuan, "T1rho and T2 relaxation times for lumbar disc degeneration: An *in vivo* comparative study at 3.0-T MRI," Eur. Radiol. **23**, 228–234 (2013).

[152]A. T. Markkola, H. J. Aronen, T. Paavonen, E. Hopsu, L. M. Sipilä, J. I. Tanttu, and R. E. Sepponen, "Spin lock and magnetization transfer imaging of head and neck tumors," Radiology **200**, 369–375 (1996).

[153]A. Borthakur, T. Gur, A. J. Wheaton *et al.*, "*In vivo* measurement of plaque burden in a mouse model of Alzheimer's disease," J. Magn. Reson. Imaging **24**, 1011–1017 (2006).

[154]I. Nestrasil, S. Michaeli, T. Liimatainen, C. E. Rydeen, C. M. Kotz, J. P. Nixon, T. Hanson, and P. J. Tuite, "T1rho and T2rho MRI in the evaluation of Parkinson's disease," J. Neurol. **257**, 964–968 (2010).

[155]R. R. Regatte, S. V. S. Akella, A. Borthakur, B. Kneeland, and R. Reddy, "Proteoglycan depletion-induced changes in transverse relaxation maps of cartilage: Comparison of T2 and T1," Acad. Radiol. **9**, 1388–1394 (2002).

[156]X. Li, E. T. Han, B. Ma, R. F. Busse, and S. Majumdar, "*In vivo* T1ρ mapping in cartilage using 3D magnetization-prepared angle-modulated partitioned k-space spoiled gradient echo snapshots (3D MAPSS)," Magn. Reson. Med. **59**, 298–307 (2008).

[157]J. Du, M. Carl, E. Diaz *et al.*, "Ultrashort TE T1rho (UTE T1rho) imaging of the Achilles tendon and meniscus," Magn. Reson. Med. **64**, 834–842 (2010).

[158]J. Du, S. Statum, R. Znamirowski, G. M. Bydder, and C. B. Chung, "Ultrashort TE T1rho magic angle imaging," Magn. Reson. Med. **69**, 682–687 (2013).

[159]Y. J. Ma, M. Carl, H. Shao, A. S. Tadros, E. Y. Chang, and J. Du, "Three-dimensional ultrashort echo time cones T1rho (3D UTE-cones-T1rho) imaging," NMR Biomed. **30**, 3709 (2017).

[160]F. W. Roemer, R. Kijowski, and A. Guermazi, "From theory to practice—the challenges of compositional MRI in osteoarthritis research," Osteoarthritis Cartilage **25**, 1923–1925 (2017).

[161]H. Shao, C. Pauli, S. Li, Y. Ma, A. S. Tadros, A. Kavanaugh *et al.*, "Magic angle effect plays a major role in both T1rho and T2 relaxation in articular cartilage," Osteoarthritis Cartilage **25**, 2022–2030 (2017).

[162]V. Mlynarik, P. Szomolanyi, R. Toffanin, F. Vittur, and S. Trattnig, "Transverse relaxation mechanisms in articular cartilage," J. Magn. Reson. **169**, 300–307 (2004).

[163]J. Ellermann, W. Ling, M. J. Nissi, E. Arendt, C. S. Carlson, M. Garwood, S. Michaeli, and S. Mangia, "MRI rotating frame relaxation measurements for articular cartilage assessment," Magn. Reson. Imaging **31**, 1537–1543 (2013).

[164]J. Rautiainen, M. J. Nissi, T. Liimatainen, W. Herzog, R. K. Korhonen, and M. T. Nieminen, "Adiabatic rotating frame relaxation of MRI reveals early cartilage degeneration in a rabbit model of anterior cruciate ligament transection," Osteoarthritis Cartilage **22**, 1444–1452 (2014).

[165]V. Casula, M. J. Nissi, J. Podlipska *et al.*, "Elevated adiabatic T1ρ and T2ρ in articular cartilage are associated with cartilage and bone lesions in early osteoarthritis: A preliminary study," J. Magn. Reson. Imaging **46**, 678–689 (2017).

[166]N. Hänninen, J. Rautiainen, L. Rieppo, S. Saarakkala, and M. J. Nissi, "Orientation anisotropy of quantitative MRI relaxation parameters in ordered tissue," Sci. Rep. **7**, 9606 (2017).

[167]Y. Ma, M. Carl, A. Searleman, X. Lu, E. Y. Chang, and J. Du, "Three dimensional adiabatic T1ρ prepared ultrashort echo time Cones (3D AdiabT1ρ UTE-Cones) sequence for whole knee imaging," Magn. Reson. Med. **80**, 1429–1439 (2018).

[168]M. Wu, W. Zhao, L. Wan *et al.*, "Quantitative three-dimensional ultrashort echo time cones imaging of the knee joint with motion correction," NMR Biomed. **33**, e4214 (2020).

[169]M. Wu, Y. Ma, L. Wan *et al.*, "Magic angle effect on adiabatic T1ρ imaging of the Achilles tendon using 3D ultrashort echo time cones trajectory," NMR Biomed. **33**, e4322 (2020).

[170]M. Wu, Y. Ma, A. Kasibhatla *et al.*, "Convincing evidence for magic angle less-sensitive quantitative T1ρ imaging of articular cartilage using the 3D ultrashort echo time cones adiabatic T1ρ (3D UTE cones-adiabT1ρ) Sequence," Magn. Reson. Med. **84**, 2551–2560 (2020).

[171]S. D. Wolff and R. S. Balaban, "Magnetization transfer contrast (MTC) and tissue water proton relaxation *in vivo*," Magn. Reson. Med. **10**, 135–144 (1989).

[172]R. M. Henkelman, X. Huang, Q. Xiang, G. J. Stanisz, S. D. Swanson, and M. J. Bronskill, "Quantitative interpretation of magnetization transfer," Magn. Reson. Med. **29**, 759–766 (1993).

[173]F. Springer, P. Martirosian, J. Machann, N. F. Schwenzer, C. D. Claussen, and F. Schick, "Magnetization transfer contrast imaging in bovine and human cortical bone applying an ultrashort echo time sequence at 3 T," Magn. Reson. Med. **61**, 1040–1048 (2009).

[174]U. Grosse, R. Syha, T. Hein, S. Gatidis *et al.*, "Diagnostic value of T1 and T2* relaxation times and off-resonance saturation effects in the evaluation of Achilles tendinopathy by MRI at 3 T," J. Magn. Reson. Imaging **41**, 964–973 (2015).

[175]E. Y. Chang, W. C. Bae, H. Shao *et al.*, "Ultrashort echo time magnetization transfer (UTE-MT) imaging of cortical bone," NMR Biomed. **28**, 873–880 (2015).

[176]Y. Ma, M. Carl, E. Y. Chang, and J. Du, "Quantitative magnetization transfer ultrashort echo time imaging using a time-efficient 3D multispoke cones sequence," Magn. Reson. Med. **79**, 692–700 (2018).

[177]Y. Ma, H. Shao, E. Y. Chang, and J. Du, "UTE magnetization transfer (UTE-MT) imaging and modeling: Magic angle independent biomarkers of tissue properties," NMR Biomed. **29**, 1546–1552 (2016).

[178]Y. Ma, A. S. Tadros, J. Du, and E. Y. Chang, "Quantitative two-dimensional ultrashort echo time magnetization transfer (2D UTE-MT) imaging of cortical bone," Magn. Reson. Med. **79**, 1941–1949 (2017).

[179]Y. Zhu, X. Cheng, Y. Ma *et al.*, "Rotator cuff tendon assessment using magic-angle insensitive 3D ultrashort echo time cones magnetization transfer (UTE-Cones-MT) imaging and modeling with histological correlation," J. Magn. Reson. Imaging **48**, 160–168 (2018).

[180]S. Jerban, Y. Ma, L. Wan *et al.*, "Collagen proton fraction from ultrashort echo time magnetization transfer (UTE-MT) MRI modeling correlates significantly with cortical bone porosity measured with micro-computed tomography (μCT)," NMR Biomed. **32**, e4045 (2019).

[181]S. Jerban, Y. J. Ma, A. Nazaran *et al.*, "Detecting stress injury (fatigue fracture) in fibular cortical bone using quantitative ultrashort echo time-magnetization transfer (UTE-MT): An *ex vivo* study," NMR Biomed. **31**, e3994 (2018).

[182]Y. Xue, Y. Ma, M. Wu *et al.*, "Quantitative 3D ultrashort echo time magnetization transfer (3D UTE-MT) imaging for evaluation of knee cartilage degeneration *in vivo*," J. Magn. Reson. Imaging **54**, 1294–1302 (2021).

[183]X. Zhang, Y. Ma, Z. Wei *et al.*, "Macromolecular fraction (MMF) from 3D ultrashort echo time cones magnetization transfer (3D UTE-Cones-MT) imaging predicts meniscal degeneration and knee osteoarthritis," Osteoarthritis Cartilage **29**, 1173–1180 (2021).

[184]W. Li, B. Wu, and C. Liu, "Quantitative susceptibility mapping of human brain reflects spatial variation in tissue composition," NeuroImage **55**, 1645–1656 (2011).

[185]M. N. Diefenbach, J. Meineke, S. Ruschke, T. Baum, A. Gersing, and D. C. Karampinos, "On the sensitivity of quantitative susceptibility mapping for measuring trabecular bone density," Magn. Reson. Med. **81**, 1739–1754 (2018).

[186]N. Sollmann, M. T. Loffler, S. Kronthaler, C. Bohm, M. Dieckmeyer, S. Ruschke, J. S. Kirschke, J. Carballido-Gamio, D. C. Karampinos, R. Krug, and T. Baum, "MRI-based quantitative osteoporosis imaging at the spine and femur," J. Magn. Reson. Imaging **54**, 12–35 (2021).

[187]A. V. Dimov, Z. Liu, P. Spincemaille, M. R. Prince, J. Du, and Y. Wang, "Bone quantitative susceptibility mapping using a chemical species-specific R2* signal model with ultrashort and conventional echo data," Magn. Reson. Med. **79**, 121–128 (2018).

[188]H. Jang, X. Lu, A. Searleman *et al.*, "True phase quantitative susceptibility mapping using continuous single point imaging: A feasibility study," Magn. Reson. Med. **81**, 1907–1914 (2019).

[189]X. Lu, Y. Ma, E. Y. Chang *et al.*, "Simultaneous quantitative susceptibility mapping (QSM) and R2* for high iron concentration quantification with 3D ultrashort echo time sequences: An echo dependence study," Magn. Reson. Med. **79**, 2315–2322 (2018).

[190]X. Lu, H. Jang, Y. Ma, E. Y. Chang, and J. Du, "Ultrashort echo time quantitative susceptibility mapping (UTE-QSM) of highly concentrated magnetic nanoparticles: A comparison study about different sampling strategies," Molecules **24**, 1143 (2019).

[191]H. Jang, A. von Drygalski, J. Wong *et al.*, "Ultrashort echo time quantitative susceptibility mapping (UTE-QSM) for detection of hemosiderin deposition in hemophilic arthropathy: A feasibility study," Magn. Reson. Med. **84**, 3246–3255 (2020).

[192]S. Jerban, X. Lu, H. Jang *et al.*, "Significant correlations between human cortical bone mineral density and quantitative susceptibility mapping (QSM) obtained with 3D Cones ultrashort echo time magnetic resonance imaging (UTE-MRI)," Magn. Reson. Imaging **62**, 104–110 (2019).

[193]Y. X. Wang, J. F. Griffith, A. W. Kwok, J. C. Leung, D. K. Yeung, A. T. Ahuja, and P. C. Leung, "Reduced bone perfusion in proximal femur of subjects with decreased bone mineral density preferentially affects the femoral neck," Bone **45**, 711–715 (2009).

[194]A. Biffar, S. Sourbron, O. Dietrich, G. Schmidt, M. Ingrisch, M. F. Reiser, and A. Baur-Melnyk, "Combined diffusion-weighted and dynamic contrast-enhanced imaging of patients with acute osteoporotic vertebral fractures," Eur. J. Radiol. **76**, 298–303 (2010).

[195]J. Zhu, L. Zhang, X. Wu, Z. Xiong, Y. Qiu, T. Hua, and G. Tang, "Reduction of longitudinal vertebral blood perfusion and its likely causes: A quantitative dynamic contrast-enhanced MR imaging study of a rat osteoporosis model," Radiology **282**, 369–380 (2017).

[196]M. D. Robson, P. D. Gatehouse, P. W. So, J. D. Bell, and G. M. Bydder, "Contrast enhancement of short T2 tissues using ultrashort TE (UTE) pulse sequences," Clin. Radiol. **59**, 720–726 (2004).

[197]L. Wan, M. Wu, V. Sheth, H. Shao, H. Jang, G. M. Bydder, and J. Du, "Evaluation of cortical bone perfusion using dynamic contrast enhanced ultrashort echo time (UTE) imaging: A feasibility study," Quant. Imaging Med. Surg. **9**, 1383–1393 (2019).

[198]S. Seah, D. Wheaton, L. Li, J. P. Dyke, C. Talmo, W. F. Harvey, and D. J. Hunter, "The relationship of tibial bone perfusion to pain in knee osteoarthritis," Osteoarthritis Cartilage **20**, 1527–1533 (2012).

[199]P. A. Hardy, M. P. Recht, D. Piraino, and D. Thomasson, "Optimization of a dual-echo in the steady state (DESS) free-precession sequence for imaging cartilage," J. Magn. Reson. Imaging **6**, 329–335 (1996).

[200]O. Bieri, C. Ganter, and K. Scheffler, "Quantitative *in vivo* diffusion imaging of cartilage using double echo steady-state free precession," Magn. Reson. Med. **68**, 720–729 (2012).

[201]E. Staroswiecki, K. L. Granlund, M. T. Alley, G. E. Gold, and B. A. Hargreaves, "Simultaneous estimation of T₂ and apparent diffusion coefficient in human articular cartilage *in vivo* with a modified three-dimensional double echo steady state (DESS) sequence at 3 T," Magn. Reson. Med. **67**, 1086–1096 (2012).

[202]S. Kohl, S. Meier, S. S. Ahmad, H. Bonel, A. K. Exadaktylos, A. Krismer, and D. S. Evangelopoulos, "Accuracy of cartilage-specific 3-T 3D-DESS magnetic

resonance imaging in the diagnosis of chondral lesions: Comparison with knee arthroscopy," J. Orthop. Surg. Res. **10**, 191 (2015).

[203] A. S. Chaudhari, B. Sveinsson, C. J. Moran, E. J. McWalter, E. M. Johnson, T. Zhang, G. E. Gold, and B. A. Hargreaves, "Imaging and T2 relaxometry of short-T2 connective tissues in the knee using ultrashort echo-time double-echo steady-state (UTEDESS)," Magn. Reson. Med. **78**, 2136–2148 (2017).

[204] H. Jang, Y. Ma, M. Carl, S. Jerban, E. Y. Chang, and J. Du, "Ultrashort echo time cones double echo steady state (UTE-DESS) for rapid morphological imaging of short T2 tissues," Magn. Reson. Med. **86**, 881–892 (2021).

[205] J. H. Duyn, Y. Yang, J. A. Frank, and J. W. van der Veen, "Simple correction method for k-space trajectory deviations in MRI," J. Magn. Reson. **132**, 150–153 (1998).

[206] M. S. Nissi, L. J. Lehto, C. A. Corum et al., "Measurement of T_1 relaxation time of osteochondral specimens using VFA-SWIFT," Magn. Reson. Med. **74**, 175–184 (2015).

[207] F. Wiesinger, A. Menini, and A. B. Solana, "Looping star," Magn Reson. Med. **81**, 57–68 (2019).

[208] B. Dionisio-Parra, F. Wiesinger, P. G. Samann, M. Czisch, and A. B. Solana, "Looping star fMRI in cognitive tasks and resting state," J. Magn. Reson. Imaging **52**, 739–751 (2020).

[209] A. J. Fields, A. Ballatori, E. C. Liebenberg, and J. C. Lotz, "Contribution of the endplates to disc degeneration," Curr. Mol. Biol. Rep. **4**, 151–160 (2018).

[210] W. C. Bae, S. Statum, Z. Zhang, T. Yamaguchi, T. Wolfson, A. C. Gamst, J. Du, G. M. Bydder, K. Masuda, and C. B. Chung, "Morphology of the cartilaginous endplates in human intervertebral disks with ultrashort echo time MR Imaging," Radiology **266**, 564–574 (2013).

[211] G. D. Fullerton, I. L. Cameron, and V. A. Ord, "Orientation of tendons in the magnetic field and its effect on T2 relaxation time," Radiology **155**, 433–435 (1985).

[212] T. J. Mosher, Z. Zhang, R. Reddy, S. Boudhar, B. N. Milestone, W. B. Morrison et al., "Knee articular cartilage damage in osteoarthritis: Analysis of MR image biomarker reproducibility in ACRIN-PA 4001 multicenter trial," Radiology **258**, 832–842 (2011).

[213] E. Chang, J. Du, and C. Chung, "UTE imaging in the musculoskeletal system," J. Magn. Reson. Imaging **41**, 870–883 (2015).

[214] G. Meachim and I. H. Emery, "Quantitative aspects of patello-femoral cartilage fibrillation in Liverpool necropsies," Ann. Rheum. Dis. **33**, 39–47 (1974).

[215] D. Hayashi, A. Guermazi, and D. J. Hunter, "OARSI year in review 2010: Imaging," Osteoarthritis Cartilage **19**, 354–360 (2011).

[216] Y. Wang, H. W. Wei, T. C. Yu, and C. K. Cheng, "Parametric analysis of the stress distribution on the articular cartilage and subchondral bone," Biomed. Mater. Eng. **17**, 241–247 (2007).

[217] E. L. Radin and R. M. Rose, "Role of subchondral bone in the initiation and progression of cartilage damage," Clin. Orthop. Relat. Res. **213**, 34–40 (1986).

[218] D. J. Hunter, Y. Q. Zhang, J. B. Niu, X. Tu, S. Amin, M. Clancy, A. Guermazi, M. Grigorian, D. Gale, and D. T. Felson, "The association of meniscal pathologic changes with cartilage loss in symptomatic knee osteoarthritis," Arthritis Rheum. **54**, 795–801 (2006).

[219] A. L. Tan, H. Toumi, M. Benjamin, A. J. Grainger, S. F. Tanner, P. Emery, and D. McGonagle, "Combined high-resolution magnetic resonance imaging and histological examination to explore the role of ligaments and tendons in the phenotypic expression of early hand osteoarthritis," Ann. Rheum. Dis. **65**, 1267–1272 (2006).

[220] K. D. Brandt, E. L. Radin, P. A. Dieppe, and L. Putte, "Yet more evidence that osteoarthritis is not a cartilage disease," Ann. Rheum. Dis. **65**, 1261–1264 (2006).

[221] I. McDermott, "Meniscal tears, repairs and replacement: Their relevance to osteoarthritis of the knee," Br. J. Sports Med. **45**, 292–297 (2011).

[222] E. L. Radin, de F. Lamotte, and P. Maquet, "Role of the menisci in the distribution of stress in the knee," Clin. Orthop. Relat. Res. **185**, 290–294 (1984).

[223] A. P. Assimakopoulos, P. G. Katonis, M. V. Agapitos, and E. I. Exarchou, "The innervation of the human meniscus," Clin. Orthop. Relat. Res. **275**, 232–236 (1992).

[224] Y. Thijs, E. Witvrouw, B. Evens, P. Coorevits, F. Almqvist, and R. Verdonk, "A prospective study on knee proprioception after meniscal allograft transplantation," Scand. J. Med. Sci. Sports **17**, 223–229 (2007).

[225] C. R. Chu, A. A. Williams, H. Christian, and M. E. Bowers, "Early diagnosis to enable early treatment of pre-osteoarthritis," Arthritis Res. Ther. **14**, 212 (2012).

[226] J. D. Kaggie, H. Markides, M. J. Graves, J. MacKay, G. Houston, A. El Haj, F. Gilbert, and F. Henson, "Ultra short echo time MRI of iron-labelled mesenchymal stem cells in an ovine osteochondral defect model," Sci. Rep. **10**, 8451 (2020).

[227] S. Lees, "A mixed pacing model for bone collagen," Calcif. Tissue Int. **33**, 591–602 (1981).

[228] W. F. Neuman and M. W. Neuman, *Skeletal Dynamics the Chemical Dynamics of Bone Mineral* (University of Chicago Press, Chicago, 1958), p. 101.

[229] F. W. Wehrli, H. K. Song, P. K. Saha, and A. C. Wright, "Quantitative MRI for the assessment of bone structure and function," NMR Biomed. **19**, 731–764 (2006).

[230] R. O. Ritchie, M. J. Buehler, and P. Hansma, "Plasticity and toughness in bone," Phys. Today **62**(6), 41–47 (2009).

[231] C. H. Turner, "Bone strength: Current concepts," Ann. N. Y. Acad. Sci. **1068**, 429–446 (2006).

[232] S. Viquet-Carrin, P. Garnero, and P. D. Delmas, "The role of collagen in bone strength," Osteoporosis Int. **17**, 319–336 (2006).

[233] S. C. Cowin, "Bone poroelasticity," J. Biomech. **32**, 217–238 (1999).

[234] E. Seeman and P. D. Delmas, "Bone quality—the material and structural basis of bone strength and fragility," N. Engl. J. Med. **354**, 2250–2261 (2006).

[235] K. G. Faulkner, "Bone matters: Are density increases necessary to reduce fracture risk?," J. Bone Miner. Res. **15**, 183–187 (2000).

[236] S. C. E. Schuit, M. van der Klift, A. E. A. M. Weel, C. E. D. H. de Laet, H. Burger, E. Seeman, A. Hofman, A. G. Uitterlinden, J. P. T. M. van Leeuwen, and H. A. P. Pols, "Fracture incidence and association with bone mineral density in elderly men and women: The Rotterdam study," Bone **34**, 195–202 (2004).

[237] K. Trajanoska, J. D. Schoufour, E. A. L. de Jonge, B. C. T. Kieboom, M. Mulder, B. H. Stricker, T. Voortman, A. G. Uitterlinden, E. H. G. Oei, M. A. Ikram, M. C. Zillikens, F. Rivadeneira, and L. Oei, "Fracture incidence and secular trends between 1989 and 2013 in a population based cohort: The Rotterdam study," Bone **114**, 116–124 (2018).

[238] J. S. Nyman, Q. Ni, D. P. Nicolella, and X. Wang, "Measurements of mobile and bound water by nuclear magnetic resonance correlate with mechanical properties of bone," Bone **42**, 193–199 (2008).

[239] R. A. Horch, J. S. Nyman, D. F. Gochberg, R. D. Dortch, and M. D. Does, "Characterization of 1H NMR signal in human cortical bone for magnetic resonance imaging," Magn. Reson. Med. **64**, 680–687 (2010).

[240] S. Jerban, J. Ma, J. Wong, A. Nazaran, A. Searleman, L. Wan, J. Williams, J. Du, and E. Y. Chang, "Ultrashort echo time magnetic resonance imaging (UTE-MRI) of cortical bone correlates well with histomorphometric assessment of bone microstructure," Bone **123**, 8–17 (2019).

[241] S. Jerban, Y. Ma, E. W. Dorthe, L. Kakos, N. Le, S. Alenezi, R. L. Sah, E. Y. Chang, D. D'Lima, and J. Du, "Assessing cortical bone mechanical properties using collagen proton fraction from ultrashort echo time magnetization transfer (UTE-MT) MRI modeling," Bone Rep. **11**, 100220 (2019).

[242] M. Y. Jerban, L. Li, H. Jang, L. Wan, T. Guo, A. Searleman, E. Y. Chang, and J. Du, "Volumetric mapping of bound and pore water as well as collagen protons in cortical bone using 3D ultrashort echo time cones MR imaging techniques," Bone **127**, 120–128 (2019).

[243] R. A. Horch, D. F. Gochberg, J. S. Nyman, and M. D. Does, "Non-invasive predictors of human cortical bone mechanical properties: T2-discriminated 1H NMR compared with high resolution x-ray," PLoS One **6**(1), 5 (2011).

[244] A. L. Hong, M. Ispiryan, M. V. Padalkar, B. C. Jones, A. S. Batzdorf, S. S. Shetye, N. Pleshko, and C. S. Rajapakse, "MRI-derived bone porosity index correlates to bone composition and mechanical stiffness," Bone Rep. **11**, 100213 (2019).

[245] C. Li, A. C. Seifert, H. S. Rad et al., "Cortical bone water concentration: Dependence of MR imaging measures on age and pore volume fraction," Radiology **272**, 796–806 (2014).

[246] M. A. Gallant, D. M. Brown, M. Hammond, J. M. Wallace, J. Du, A. C. Deymier-Black, J. D. Almer, S. R. Stock, M. R. Allen, and D. B. Burr, "Bone

cell-independent benefits of raloxifene on the skeleton: A novel mechanism for improving bone material properties," Bone **61**, 191–200 (2014).

[247] Y. Xie, S. Liu, J. Qu, P. Wu, H. Tao, and S. Chen, "Quantitative magnetic resonance imaging UTE-T2* mapping of tendon healing after arthroscopic rotator cuff repair: A longitudinal study," Am. J. Sports Med. **48**, 2677–2685 (2020).

[248] M. Han, P. E. Larson, J. Liu, and R. Krug, "Depiction of Achilles tendon microstructure *in vivo* using high-resolution three-dimensional ultrashort echo-time magnetic resonance imaging at 7 T," Invest. Radiol. **49**, 339–345 (2014).

[249] S. Jerban, Y. Ma, B. Namiranian, A. Ashir, H. Shirazian, Z. Wei, N. Le, M. Wu, Z. Cai, J. Du, and E. Y. Chang, "Age-related decrease in collagen proton fraction in tibial tendons estimated by magnetization transfer modeling of ultrashort echo time magnetic resonance imaging (UTE-MRI)," Sci. Rep. **9**, 17974 (2019).

[250] M. Benjamin and G. M. Bydder, "Magnetic resonance imaging of entheses using ultrashort TE (UTE) pulse sequences," J. Magn. Reson. Imaging **25**, 381–389 (2007).

[251] D. Geiger, W. Bae, S. Statum, J. Du, and C. B. Chung, "Quantitative 3D ultrashort time-to-echo (UTE) MRI and micro-CT evaluation of the temporomandibular joint (TMJ) condylar morphology," Skeletal Radiol. **43**, 19–25 (2014).

[252] M. Carl, H. T. Sanal, E. Diaz, J. Du, O. Girard, S. Statum, R. Znamirowski, and C. B. Chung, "Optimizing MR signal contrast of the temporomandibular joint disk," J. Magn. Reson. Imaging **34**, 1458–1464 (2011).

[253] H. T. Sanal, W. C. Bae, C. Pauli, J. Du, S. Statum, R. Znamirowski, R. L. Sah, and C. B. Chung, "Magnetic resonance imaging of the temporomandibular joint disc: Feasibility of novel quantitative magnetic resonance evaluation using histologic and biomechanical reference standards," J. Orofacial Pain **25**, 345–353 (2010).

[254] C. M. Filley and R. D. Fields, "White matter and cognition: Making the connection," J. Neurophysiol. **116**, 2093–2104 (2016).

[255] P. A. Felts, T. A. Baker, and K. J. Smith, "Conduction in segmentally demyelinated mammalian central axons," J. Neurosci. **17**, 7267–7277 (1997).

[256] D. J. Miller, T. Duka, C. D. Stimpson, S. J. Schapiro, W. B. Baze, M. J. McArthur, A. J. Fobbs, S. M. Sousa, N. Sestan, D. E. Wildman, L. Lipovich, C. W. Kuzawa, P. R. Hof, and C. C. Sherwood, "Prolonged myelination in human neocortical evolution," Proc. Natl. Acad. Sci. U. S. A. **109**, 16480–16485 (2012).

[257] U. Funfschilling, L. M. Supplie, D. Mahad *et al.*, "Glycolytic oligodendrocytes maintain myelin and long-term axonal integrity," Nature **485**, 517–521 (2012).

[258] E. M. Gibson, D. Purger, C. W. Mount *et al.*, "Neuronal activity promotes oligodendrogenesis and adaptive myelination in the mammalian brain," Science **344**, 1252304 (2014).

[259] I. A. McKenzie, D. Ohayon, H. Li *et al.*, "Motor skill learning requires active central myelination," Science **346**, 318–322 (2014).

[260] P. Long and G. Corfas, "To learn is to myelinate," Science **346**, 298–299 (2014).

[261] C. Sampaio-Baptista, A. A. Khrapitchev, S. Foxley *et al.*, "Motor skill learning induces changes in white matter microstructure and myelination," J. Neurosci. **33**, 19499–19403 (2013).

[262] G. S. Tomassy, D. R. Berger, H. H. Chen *et al.*, "Distinct profiles of myelin distribution along single axons of pyramidal neurons in the neocortex," Science **344**, 319–324 (2014).

[263] R. D. Fields, "Myelin—more than insulation," Science **344**, 264–266 (2014).

[264] K. Sinha, S. Karimi-Abdolrezaee, A. A. Velumian, and M. G. Fehlings, "Functional changes in genetically demyelinated spinal cord axons of shiverer mice role of juxtaparanodal Kv1 family K+ channels," J. Neurophysiol. **95**, 1683–1695 (2006).

[265] Y. Lee, B. M. Morrison, Y. Li *et al.*, "Oligodendroglia metabolically support axons and contribute to neurodegeneration," Nature **487**, 443–448 (2012).

[266] D. Chabas, S. E. Baranzini, D. Mitchell *et al.*, "The influence of the proinflammatory cytokine, osteopontin, on autoimmune demyelinating disease," Science **294**, 1731–1735 (2001).

[267] L. Steinman, "Multiple sclerosis: A coordinated immunological attack against myelin in the central nervous system," Cell **85**, 299–302 (1996).

[268] D. C. Dean, S. A. Hurley, S. R. Kecskemeti *et al.*, "Association of amyloid pathology with myelin alteration in preclinical Alzheimer's disease," JAMA Neurol. **74**, 41–49 (2017).

[269] D. C. Dean, J. Sojkova, S. Hurley *et al.*, "Alterations of myelin content in Parkinson's disease: A cross-sectional neuroimaging study," PLoS One **11**, 0163774 (2016).

[270] L. Concha, D. W. Gross, B. M. Wheatley, and C. Beaulieu, "Diffusion tensor imaging of time-dependent axonal and myelin degradation after corpus callosotomy in epilepsy patients," NeuroImage **32**, 1090–1099 (2006).

[271] A. J. Mierzwa, C. M. Marion, G. M. Sullivan *et al.*, "Components of myelin damage and repair in the progression of white matter pathology after mild traumatic brain injury," J. Neuropathol. Exp. Neurol. **74**, 218–232 (2015).

[272] H. Lecar, G. Ehrenstein, and I. Stillman, "Detection of molecular motion in lyophilized myelin by nuclear magnetic resonance," Biophys. J. **11**, 140–145 (1971).

[273] A. MacKay, C. Laule, I. Vavasour, T. Bjarnason, S. Kolind, and B. Madler, "Insights into brain microstructure from the T2 distribution," Magn. Reson. Imaging **24**, 515–525 (2006).

[274] J. Oh, E. T. Han, D. Pelletier, and S. J. Nelson, "Measurement of *in vivo* multi-component T2 relaxation times for brain tissue using multi-slice T2 prep at 1.5 and 3 T," Magn. Reson. Imaging **24**, 33–43 (2006).

[275] D. Hwang, D. H. Kim, and Y. P. Du, "*In vivo* multi-slice mapping of myelin water content using T2* decay," NeuroImage **52**, 198–204 (2010).

[276] K. Schmierer, F. Scaravilli, D. R. Altmann, G. J. Barker, and D. H. Miller, "Magnetization transfer ratio and myelin in postmortem multiple sclerosis brain," Ann. Neurol. **56**, 407–415 (2004).

[277] S. K. Song, J. Yoshino, T. Q. Le, S. J. Lin, S. W. Sun, A. H. Cross *et al.*, "Dymyelination increases radial diffusivity in corpus callosum of mouse brain," NeuroImage **26**, 132–140 (2005).

[278] K. Schmierer, C. A. Wheeler-Kingshott, D. J. Tozer, P. A. Boulby, H. G. Parkes, T. A. Yousry, F. Scaravilli, G. J. Barker, P. S. Tofts, and D. H. Miller, "Quantitative magnetic resonance of postmortem multiple sclerosis brain before and after fixation," Magn. Reson. Med. **59**, 268–277 (2008).

[279] V. Dousset, R. I. Grossman, K. N. Ramer, M. D. Schnall, L. H. Young, F. Gonzalez-Scarano, E. Lavi, and J. A. Cohen, "Experimental allergic encephalomyelitis and multiple sclerosis: Lesion characterization with magnetization transfer imaging," Radiology **182**, 483–491 (1992).

[280] J. Newcombe, C. P. Hawkins, C. L. Henderson *et al.*, "Histopathology of multiple sclerosis lesions detected by magnetic resonance imaging in unfixed postmortem central nervous system tissue," Brain **114**, 1013–1023 (1991).

[281] P. J. Gareau, B. K. Rutt, S. J. Karlik, and J. R. Mitchell, "Magnetization transfer and multicomponent T2 relaxation measurements with histopathologic correlation in an experimental model of MS," J. Magn. Reson. Imaging **11**, 586–595 (2000).

[282] C. Guglielmetti, T. Boucneau, P. Cao, A. Van der Linden, P. E. Z. Larson, and M. M. Chaumeli, "Longitudinal evaluation of demyelinated lesions in a multiple sclerosis model using ultrashort echo time magnetization transfer (UTE-MT) imaging," NeuroImage **208**, 116415 (2020).

[283] Y. Ma, A. Searleman, H. Jang, J. Wong, E. Y. Chang, J. Corey-Bloom, G. M. Bydder, and J. Du, "Whole-brain myelin mapping using 3D double echo sliding inversion recovery ultrashort echo time (DESIRE UTE) MRI," Radiology **294**, 362–374 (2020).

[284] O. Togao, R. Tsuji, Y. Ohno, I. Dimitrov, and M. Takahashi, "Ultrashort echo time (UTE) MRI of the lung: Assessment of tissue density in the lung parenchyma," Magn. Reson. Med. **64**, 1491–1498 (2010).

[285] Y. Ohno, H. Koyama, T. Yoshikawa, K. Matsumoto, M. Takahashi, M. Van Cauteren, and K. Sugimura, "T2* measurements of 3-T MRI with ultrashort TEs: Capabilities of pulmonary function assessment and clinical stage classification in smokers," Am. J. Roentgenol. **197**, 279–285 (2011).

[286] K. M. Johnson, S. B. Fain, M. L. Schiebler, and S. Nagle, "Optimized 3D ultrashort echo time pulmonary MRI," Magn. Reson. Med. **70**, 1241–1250 (2013).

[287] P. Larson, K. M. Johnson, M. D. Hope *et al.*, "Detection of small pulmonary nodules with ultrashort echo time sequences in oncology patients by using a PET/MR system," Radiology **278**, 239–246 (2015).

[288] W. Jiang, F. Ong, K. M. Johnson *et al.*, "Motion robust high-resolution 3D free-breathing pulmonary MRI using dynamic 3D image self-navigator," Magn. Reson. Med. **79**, 2954–2967 (2018).

[289] L. I. Feng, J. Delacoste, D. Smith *et al.*, "Simultaneous evaluation of lung anatomy and ventilation using 4D respiratory-motion-resolved ultrashort echo time sparse MRI," J. Magn. Reson. Imaging **49**, 411–422 (2019).

[290]X. Zhu, M. Chan, M. Lustig, K. M. Johnson, and P. Larson, "Iterative motion-compensation reconstruction ultra-short TE (iMoCo UTE) for high-resolution free-breathing pulmonary MRI," Magn. Reson. Med. **83**, 1208–1221 (2019).

[291]S. Yang, Y. Zhang, J. Shen et al., "Clinical potential of UTE-MRI for assessing COVID-19: Patient- and lesion-based comparative analysis," J. Magn. Reson. Imaging **52**, 397–406 (2020).

[292]Y. Kohgo, K. Ikuta, T. Ohtake, Y. Torimoto, and J. Kato, "Body iron metabolism and pathophysiology of iron overload," Int. J. Hematol. **88**, 7–15 (2008).

[293]J. K. Olynyk, T. G. St. Pierre, R. S. Britton, E. M. Brunt, and B. R. Bacon, "Duration of hepatic iron exposure increases the risk of significant fibrosis in hereditary hemochromatosis: a new role for magnetic resonance imaging," Am. J. Gastroenterol. **100**, 837–841 (2005).

[294]A. J. Krafft, R. B. Loeffler, R. Song, A. Tipirneni-Sajja, M. B. McCarville, M. D. Robson, K. S. Hankins, and C. M. Hillenbrand, "Quantitative ultrashort echo time imaging for assessment of massive iron overload at 1.5 and 3 T," Magn. Reson. Med. **78**, 1839–1851 (2017).

[295]M. Kramer, A. G. Motaal, K. H. Herrmann, B. Loffler, J. R. Reichenbach, J. Strijkers, and V. Hoerr, "Cardiac 4D phase-contrast CMR at 9.4T using self-gated ultra-short echo time (UTE) imaging," J. Cardiovasc. Magn. Reson. **19**, 39 (2017).

[296]R. R. Edelman and I. Koktzoglou, "Non-contrast MR angiography: An update," J. Magn. Reson. Imaging **49**, 355–373 (2019).

[297]C. Zhang, W. Dou, K. Yu, Y. Ji, W. Wang, M. U. Sami, Y. Shen, and K. Xu, "The feasibility of non-contrast-enhanced zero echo time magnetic resonance angiography for characterization of intracranial atherosclerotic disease," Quant. Imaging Med. Surg. **11**, 2442–2452 (2021).

[298]K. R. O'Brien, S. G. Myerson, B. R. Cowan, A. A. Young, and M. D. Robson, "Phase contrast ultrashort TE: A more reliable technique for measurement of high-velocity turbulent stenotic jets," Magn. Reson. Med. **62**, 626–636 (2009).

[299]N. Takano, M. Suzuki, R. Irie et al., "Non-contrast-enhanced silent scan MR angiography of intracranial anterior circulation aneurysms treated with a low-profile visualized intraluminal support device," Am. J. Neuroradiology **38**, 1610–1616 (2017).

[300]M. Katsuki, N. Narita, D. Ozaki, Y. Sato, S. Iwata, and T. Tominaga, "Three Tesla magnetic resonance angiography with ultrashort echo time describes the arteries near the cerebral aneurysm with clip and the peripheral cerebral arteries," Surg. Neurol. Int. **11**, 224 (2020).

[301]C. F. Chan, N. G. Keenan, S. Nielles-Vallespin, P. Gatehouse, M. N. Sheppard, J. J. Boyle, D. J. Pennell, and D. N. Firmin, "Ultra-short echo time cardiovascular magnetic resonance of atherosclerotic carotid plaque," J. Cardovasc. Magn. Reson. **12**, 17 (2010).

[302]S. Sharma, S. Boujraf, A. Bornstedt, V. Hombach, A. Ignatius, A. Oberhuber, and R. Volker, "Quantification of calcifications in endarterectomy samples by means of high-resolution ultra-short echo time imaging," Invest. Radiol. **45**, 109–113 (2010).

[303]J. Du, J. Corbeil, R. Znamirowski, N. Angle, M. Peterson, G. M. Bydder, and A. M. Kahn, "Direct imaging and quantification of carotid plaque calcification," Magn. Reson. Med. **65**, 1013–1020 (2011).

[304]J. Du, M. Peterson, N. Kansal, G. M. Bydder, and A. Kahn, "Mineralization in calcified plaque is like that of cortical bone—further evidence from ultrashort echo time (UTE) magnetic resonance imaging of carotid plaque calcification and cortical bone," Med. Phys. **40**, 102301 (2013).

[305]M. Carl, K. Koch, and J. Du, "MR imaging near metal with undersampled 3D radial UTE-MAVRIC sequences," Magn. Reson. Med. **69**, 27–36 (2013).

[306]W. E. Shaalan, H. Cheng, B. Gewertz, J. F. McKinsey, L. B. Schwartz, D. Katz, D. Cao, T. Desai, S. Glagov, and H. S. Bassiouny, "Degree of carotid plaque calcification in relation to symptomatic outcome and plaque inflammation," J. Vasc. Surg. **40**, 262–269 (2004).

[307]H. Huang, R. Virmani, H. Younis, A. P. Burke, R. D. Kamm, and R. T. Lee, "The impact of calcification on the biomechanical stability of atherosclerotic plaques," Circulation **103**, 1051–1056 (2001).

[308]M. Abedin, Y. Tintut, and L. L. Demer, "Vascular calcification: Mechanisms and clinical ramifications," Arterioscler., Thromb., Vasc. Biol. **24**, 1161–1170 (2004).

[309]M. Banobre-Lopez, A. Teijeiro, and J. Rivas, "Magnetic nanoparticle-based hyperthermia for cancer treatment," Rep. Pract. Oncol. Radiother. **18**, 398–400 (2013).

[310]C. G. Peterfy, A. Guermazi, S. Zaim et al., "Whole-Organ magnetic resonance imaging score (WORMS) of the knee in osteoarthritis," Osteoarthritis Cartilage **12**, 177–190 (2004).

[311]C. W. Pfirrmann, A. Metzdorf, M. Zanetti et al., "Magnetic resonance classification of lumbar intervertebral disc degeneration," Spine **26**, 1873–1878 (2001).

[312]J. F. Griffith, Y. X. Wang, G. E. Antonio et al., "Modified Pfirrmann grading system for lumbar intervertebral disc degeneration," Spine **32**, 708–712 (2007).

[313]A. C. Zelinski, L. M. Angelone, V. K. Goyal, G. Bonmassar, E. Adalsteinsson, and L. L. Wald, "Specific absorption rate studies of the parallel transmission of inner-volume excitations at 7 T," J. Magn. Reson. Imaging **28**, 1005–1018 (2008).

[314]A. Lu, B. L. Daniel, J. M. Pauly, and K. B. Pauly, "Improved slice selection for R2* mapping during cryoablation with eddy current compensation," J. Magn. Reson. Imaging **28**, 190–198 (2008).

[315]R. E. Breighner, Y. Endo, G. P. Konin, L. V. Gulotta, M. F. Koff, and H. G. Potter, "Technical developments: Zero echo time imaging of the shoulder: Enhanced osseous detail by using MR imaging," Radiology **286**, 960–966 (2018).

[316]R. de Mello, Y. Ma, A. Ashir, S. Jerban, H. Hoenecke, M. Carl, J. Du, and E. Y. Chang, "Three-dimensional zero echo time magnetic resonance imaging versus three-dimensional computed tomography for glenoid bone assessment," Arthroscopy **36**, 2391–2400 (2020).

[317]L. B. Lane and P. G. Bullough, "Age-related changes in the thickness of the calcified zone and the number of tidemarks in adult human articular cartilage," J. Bone Joint Surg. Br. **62**, 372–375 (1980).

[318]B. Berg-Johansen, M. Han, A. J. Fields et al., "Cartilage endplate thickness variation measured by ultrashort echo-time MRI is associated with adjacent disc degeneration," Spine **43**, 592–600 (2018).

[319]S. C. Foreman, W. Ashmeik, J. D. Baal, M. Han, E. Bahroos, C. E. von Schacky, M. Carl, R. Krug, G. B. Joseph, and T. M. Link, "Patients with type 2 diabetes exhibit a more mineralized deep cartilage layer compared with nondiabetic controls: A pilot study," Cartilage **13**, 428S (2021).

[320]M. Byra, M. Wu, X. Zhang, H. Jang, Y. Ma, E. Y. Chang, S. Shah, and J. Du, "Knee menisci segmentation using transfer learning with deep convolutional neural networks in 3D ultrashort echo time (UTE) Cones MR imaging to determine relaxometry," Magn. Reson. Med. **83**, 1109–1122 (2020).

[321]Y. Xue, H. Jang, M. Byra, Z. Cai, M. Wu, E. Y. Chang, Y. Ma, and J. Du, "Automated cartilage segmentation and quantification using 3D ultrashort echo time (UTE) Cones MR imaging with deep convolutional neural networks," Eur. Radiol. **31**, 7653–7663 (2021).

[322]R. Kijowski, F. Liu, F. Caliva, and V. Pedoia, "Deep learning for lesion detection, progression, and prediction of musculoskeletal disease," J. Magn. Reson. Imaging **52**, 1607–1619 (2020).

[323]D. Shen, G. Wu, and H. I. Suk, "Deep learning in medical image analysis," Annu. Rev. Biomed. Eng. **19**, 221–248 (2017).